The University Of Sheffield.

Towards Integrated Scalable Nanophotonic Circuits

By:

James Edward Dixon

A thesis submitted in partial fulfilment of the requirements for the degree of Doctor of Philosophy

The University of Sheffield
Faculty of Science
Department of Physics & Astronomy

Submission Date

September 2017

Abstract

This thesis presents optical measurements used to explore nanophotonic circuits composed of III-V semiconductors with embedded quantum dots. The focus of this work is to investigate issues related to the scalability and performance of these structures.

A technique to register the position of a quantum dot, relative to pre-fabricated registration markers, with the aid of a solid immersion lens, is developed. The variance in the repeatedly registered position of the quantum dot is shown to be significantly reduced as a result of the solid immersion lens, compared with positions registered without a solid immersion lens.

The total error of the deterministic fabrication, using position registered quantum dots, is small when compared to the size of optical fields. Confirmation of this has been achieved through two independent methods. Re-registration of the position relative to deterministically positioned registration markers show that the total error of deterministic fabrication is small. Additionally, the demonstration of optical spin readout, via the deterministic positioning of a quantum dot at a chiral point of a suspended nanobeam waveguide, further confirms the positional accuracy of the technique.

The demonstration of efficiently coupled single photons form an embedded quantum into a nanobeam waveguide, with enhanced coherence lengths due to resonant excitation, is achieved. A high level of resonant laser rejection is demonstrated due to the orthogonal excitation and waveguide propagation directions.

Acknowledgements

I am extremely grateful for the opportunity to have studied within the Low Dimensional Structures and Devices (LDSD) group within the Department of Physics and Astronomy at the University of Sheffield. The wealth of knowledge and experience available to support me throughout my PhD provided an excellent environment to grow and develop as a physicist.

I would like to acknowledge the work and support of all those within the LDSD group and the III-V centre who made this work not only possible, but also an enjoyable experience. I would especially like to thank my supervisor, Professor Maurice Skolnick for his continued support and guidance throughout the entire process.

This thesis is a testament to friends and family, who have continuously nurtured, pushed and supported me. I would especially like to dedicate this thesis to my wife, who has endured all the stress and late nights which have been associated with this thesis over the past five years. For her continued support and love I am forever grateful.

The first principle is that
you must not fool yourself.....
..... And you are the easiest
person to fool.

- *R. P. Feynman (1974)*

Table of Contents

Table of Contents ix
1. Introduction 1
1.1. Quantum Information Processing 1
1.2. Nanophotonic QIP 4
1.3. Quantum Dots 8
1.4. Nanobeam waveguides 11
1.5. Scope of thesis 13
1.6. References 15
2. Experimental Methods 19
2.1. Introduction 19
2.1.1. Acknowledgments 19
2.2. Sample Growth 19
2.2.1. Molecular Beam Epitaxy 19
2.2.2. Stranski-Krastanov Growth 20
2.2.3. Heterostructures 21
2.3. Device Fabrication 22
2.3.1. Spin Coating 23
2.3.2. Electron Beam Lithography 24
2.3.3. Developing 25
2.3.4. Etching 25
2.4. Cryostats 27
2.4.1. Continuous flow cryostat 27
2.4.2. Bath Cryostat 30
2.5. Optical Measurements 32
2.5.1. Spectral Analysis and Filtering 32
2.5.2. Michelson Interferometer 33
2.5.3. Lifetime 35
2.5.4. Hanbury-Brown Twiss 37
2.6. Solid Immersion Lens 39
2.7. References 44
3. Dot Registration 47
3.1. Introduction 47
3.1.1. Chapter Overview 47
3.1.2. Precision 48
3.1.3. Nanowires 50
3.1.4. Deterministic Growth 51

3.1.5. Dot Registration 52
3.2. Samples 55
3.2.1. Marker Design 55
3.2.2. Marker Fabrication 56
3.2.3. Marker Alignment 57
3.3. Registration 59
3.3.1. System stability 61
3.3.2. Surface Damage 64
3.3.3. Solid Immersion Lens Enhanced Registration 71
3.4. Conclusion 77
3.5. References 79
4. Deterministic Fabrication With Registered Quantum Dots 83
4.1. Introduction 83
4.2. EBL Precision 84
4.2.1. Sources of Error 84
4.2.2. Quantum Dot Re-Registration 91
4.3. Nanobeam Waveguides 93
4.3.1. Bulk Characterisation 94
4.3.2. Waveguide Characterisation 101
4.4. Optical Spin Readout 108
4.4.1. Simulations 110
4.4.2. Deterministic Spin Readout 112
4.5. Conclusions 118
4.6. References 119
5. Waveguide Coupled Resonance Fluorescence 121
5.1. Introduction 121
5.1.1. Coherence 121
5.1.2. Resonance Fluorescence 123
5.1.3. Laser Suppression 124
5.2. Excitation Regime 125
5.3. Nanobeam Waveguide Laser Suppression 127
5.4. Optical Measurements 130
5.5. Conclusions 139
5.6. References 140
6. Summary and outlook 145
6.1. Chapter Overview 145
6.1.1. Dot Registration 145
6.1.2. Deterministic Fabrication 145

6.1.3. Resonance Fluorescence 146
6.2. Outlook 147
6.2.1. In-Situ Lithography 147
6.2.2. Fabrication Induced Spectral Changes 149
6.2.3. Single mode diode waveguides 151
6.2.4. Spin-initialisation 152
6.3. References 153

`

1. Introduction

The phrases “quantum computing” and “quantum information processing” are ones which are becoming more readily recognised outside the scientific community. This is in part due to commercial ventures involving quantum computing which have bridged the gap between the academic and commercial world [1]. Even so, quantum information processing is still in its infancy, with significant work remaining in order to realise large scale, integrated quantum processors. Work presented in this thesis is therefore directly motivated by this fact, and focusing on nanophotonic structures, examines several of the challenges facing the realisation of scalable photonic architectures.

Prior to any discussion of experimental work, a brief overview of quantum information processing and the role of quantum dots embedded in nanophotonic devices is presented. The purpose of this introduction is therefore to provide a general context for subsequent results. For a more detailed description of any of the points discussed in this section, the reader is directed to the references, or to any number of textbooks on quantum information processing, such as that by M. Nielsen [2].

1.1. Quantum Information Processing

The components used in the classical computer throughout its development have changed significantly, ranging from mechanical gears to valves and transistors. However, the fundamental principles of how a computer operates have remained fixed. That is, in a classical computer, data is read in, stored, processed and output in the form of binary digits (bits) which can take one of two values (0 or 1). The most common form a bit takes in the modern computer is that of a voltage. Although somewhat arbitrary, a voltage difference can be used to distinguish two binary states, with the magnitude of the difference a physical parameter which depends on the specifics of the components used.

In order to perform complex calculations, multiple bits can be initialised, and passed through a series of logical gates made up of several transistors. An example of a simple ‘AND’ gate frequently used in a modern computer is shown in Figure 1-1 which uses two transistors to compare the voltage of two inputs. The truth table presented as an insert shows that an output of ‘1’, corresponding to a ‘high’ voltage, is measured only if both inputs are also equal to ‘1’. Through the combination of additional transistors in

alternative configurations, additional computations can be performed, such as the NOT and OR gates. For the classical computer, these three gates (AND, NOT and OR) are referred to as universal gates for Boolean logic operations. That is to say, any arbitrary complex mathematical function, that we may want to obtain the answer to, can be solved via various combinations of these three gates alone.

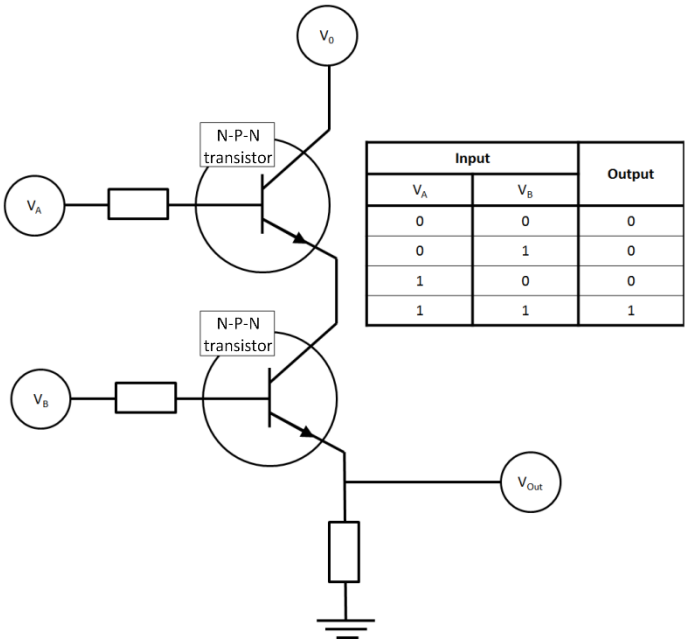

Input		Output
V_A	V_B	
0	0	0
0	1	0
1	0	0
1	1	1

Figure 1-1 – Circuit diagram showing simple 'AND' gate using N-P-N transistors in a classical computer

It can be seen therefore that in order to perform complex tasks, an increasing number of transistors will be required. Furthermore, it is often possible and quicker to break many of these tasks down into multiple simpler tasks which could be performed in parallel with the use of additional transistors. As the demand for faster, more energy efficient computation compounds with the demand for an increased density of transistors, there is significant motivation for developing smaller and smaller transistors.

As the size of transistors decrease, the need to better understand and control quantum effects becomes ever more important as transistors approach the atomic scale. At these small scales, the macroscopic variables used in classical computation are subject to quantum fluctuations through effects such as quantum tunnelling. As our understanding and the implications of these quantum affects developed, it was realised that under certain circumstances these quantum effects may be beneficial, and as a result, an alternative form of computation was first proposed by Feynman in the 1980's [3], referred to as a quantum computer. The goal of the quantum computer is to utilise the

physical laws which govern these quantum effects to carry out computational tasks which may more '*efficiently*' simulate certain physical problems. Analogous to the 'bits' of the classical computer, information is processed using two level systems as quantum bits (qubit's). Unlike classical bits, these qubits can take advantage of superposition, where the qubit may be in both the 0 and 1 state simultaneously, as described by the wavefunction $|\psi\rangle = \alpha|0\rangle + \beta|1\rangle$, where α and β may be any complex number such that $|\alpha|^2 + |\beta|^2 = 1$.

To understand the advantages a quantum computer offers over a classical computer, the computational and energy efficiency need to be considered. Of the computational advantages promised by a quantum computer, Shor's factoring algorithm [4] initially stood out as one with significant real world consequences. This is because one of the foundations of modern day cyber security is based on the enormous computational time required to calculate the prime factors of a large random number. Shor's algorithm makes use of quantum entanglement which results in an exponential decrease in the number of computational steps required to determine the factors. Additional quantum algorithms, such as Grover's search and the Quantum Fourier Transform are amongst other similar computation processes which may be carried out quadratically or exponentially quicker than on a classical computer [5][2]. As a result, complex problems which are currently considered too computationally time consuming to solve may be done so on a reasonable time scale using a quantum computer.

The computational energy efficiency refers to the maximum energy efficiency possible per bit of information. In the classical computer, it can be seen for the 'AND' gate described in Figure 1-1, for two bits of information input, a single bit of information is output. This is an inherently irreversible process which increases the entropy of the system and results in a minimum of $k_B T \ln(2)$ of energy released, referred to as the Landauer limit [6]. For a quantum system, as each gate operation is required to be a unitary transformation, it is by definition reversible and no information is lost. A quantum computer is in principle therefore more energy efficient than modern computers. It is worth noting however that through the use of additional transistors, a Toffoli gate [7] can be constructed for a classical computer which does not result in any loss of information, but in doing so, the number of transistors per gate operation is increased. This type of reversible computation is not commonly employed in conventional computers and would likely represent a significant technological barrier.

1.2. Nanophotonic QIP

Initially, one of the strongest contenders for quantum information processing was that of NMR, in part due to the well-established technology at the time. As such, it was one of the first platforms to experimentally demonstrate Shor's quantum factoring algorithm on a four qubit number [8]. Since then, alternative platforms have been presented, such as trapped ions, superconducting josephson junctions and quantum dot nanophotonic cicruits, each with distinct advantages. The interest in such a diverse set of platforms can be understood when considering the five criteria outlined by DiVincenzo that any system must possess in order to carry out meaningful calculations [9]. Quantum dots embedded within nanophotonic circuits are particularly well suited to several of these criteria, especially those which pertain to scalability due to their strong interactions with photons. This enables the creation of highly scalable photonic networks, a significant obstacle in most other quantum information platforms. In contrast, well isolated systems such as trapped ions experience long coherence times with respect to gate operation times, which quantum dots traditionally struggle to achieve, resulting in an increased gate fidelity and computational reliability. The trade-offs of each system mean there is not one system which is best suited for quantum computing, and the strengths and weaknesses of each system are continuously being explored and improved.

We focus here on the advances being made with quantum dot nanophotonic circuits, providing a brief overview of several key areas of research which are aimed directly at addressing one or more of the DiVincenzo criteria. The first DiVincenzo criterion is directly aimed at the ability to utilise multiple qubits so that increasingly complex calculations may be performed.

1. *"A scalable physical system with well characterised qubits"*

The fabrication of quantum dots which act as both a source of qubits as well as computational nodes is typically performed using molecular beam epitaxy or metal-organic chemical vapour deposition techniques. Via controlling the fabrication parameters, quantum dots may be grown at high densities yielding large numbers of potential qubits. Details of the self-assembly growth process are provided in Chapter 2, and a more detailed look at the quantum dot properties which make it suitable to act as a qubit are discussed in section 1.3. With this in mind, there is significant interest in achieving site controlled growth of quantum dots [10]–[12] to achieve both optimal

performance of nanophotonic structures as well as scalability. Techniques exploiting nucleated growth or deterministic fabrication of quantum dots embedded within nanophotonic structures have already demonstrated moderate success, with optimal light-matter coupling being demonstrated via the characteristic anti-crossing behaviour of the strong coupling regime [13]. As the work presented in Chapter 3 and 4 is directly focussed on realising deterministic fabrication, additional details can be found in the relevant sections.

With a scalable source of qubits, the second criterion states that it must be possible to initialise these qubits to an arbitrary state. What this arbitrary state is depends on the measurement basis chosen, with various proposals including the population of single photons, or in the spin state of either the excited quantum dot or emitted photons. Initialisation may therefore be performed either by allowing the system sufficient time that it naturally decays into its ground state (no photons), or by directly initialising a given spin state via the use of a polarised excitation laser [14]. Unlike the first criterion which has varying degrees of success, the initialisation criterion is pass or fail and a necessity.

2. *"The ability to initialise the state of the qubits to a simple fiducial state"*

Initialisation plays an important role in quantum computation as it enables the correct alignment of the measurement basis with that of the final qubit state. Additionally, many quantum algorithms make use of a continuous stream of ancilla qubits, such as proposals for quantum error correction [15], which are all required to be initialised to the same ground state. The continuous need for initialised qubits is therefore also linked to the third DiVincenzo criterion, requiring the state to evolve slowly with respect to time scales of computations. That is, initialised qubits should remain in the initialised state with a high fidelity until they are needed.

3. *"Long relevant decoherence times compared to the gate operation time"*

When considering long de-coherence times of a nanophotonic circuit, it is simplest to consider the physical and optical components separately. In comparison, the decoherence of emitted photons, with respect to exciton decoherence, can be neglected as the photons interact weekly with the photonic circuit. Decoherence of the excited quantum dot state is therefore dominant due to the strong coupling of the quantum dot to its solid state environment which means that it may be influenced by a number of

effects, including phonon scattering and charge fluctuations [16]. The magnitude of these effects is strongly coupled to the excitation regime used to initialise the qubit, and as such, an active area of research is that aimed at resonantly exciting the quantum dot under low powers to realise highly coherent, indistinguishable photons [17], [18]. To date, the longest coherence times observed are for the electron spin in quantum dots which have been shown to exceed 1 μs using spin echo techniques [14]. This is several orders of magnitude longer than the optical gate times needed, which have been demonstrated in the 1 – 10 ps range [19].

By realising the first three of the DiVincenzo criteria, a scalable quantum system can be realised, however it is far from capable of performing quantum information processing. The final two criteria relate to this issue, stating that it must be possible to manipulate the state of the qubit in a meaningful way, as well as measure the final state.

4. "A 'universal' set of quantum gates"

5. "A qubit-specific measurement capability"

For nanophotonic circuits, quantum gates have been proposed via the use of photonic devices such as beam splitters and optical cavities, as well as light matter coupling to the exciton states of quantum dots. Depending on the measurement basis, as discussed for the second criterion, the photonic components used may be different, such as either a simple 50:50 beam splitters or more sophisticated polarising beam splitters [20]. In order to realise these devices on chip, various photonic structures have been proposed, including evanescent coupling [21] between nanobeam waveguides and directional coupling of orthogonal polarisations via displaced quantum dots [22], [23]. In order to realise a universal set of quantum gates, the Hadamard gate, the phase gate and the controlled not gate are required [2].

Measurement of the final state in the computational basis may be performed using one or more single photon detectors in combination with nanophotonic structures such as polarising beam splitters. In an effort to realise on chip detection of single photons, attention is turning to superconducting thin films fabricated atop of the photonic circuit [24]. By maintaining the current in the superconducting wire just below the critical current, localised heating induced by the absorption of a photon introduces a short lived normal conducting hot-spot. Current research goals include increasing the quantum

efficiency of these devices, whilst developing techniques to reduce stray scattered laser light which would render any desirable signal unresolvable.

DiVincenzo realised that if a system possessed all five of these criteria, it is in principle possible to realise a scalable quantum computer. The advantages of the quantum computer over a classical computer, as discussed previously, may however be rendered moot when considering the scale of classical computation which may be achieved using a large number of networked computers. As a result, two additional desirable criteria were also specified which would enable quantum networks to be established, and therefore allow for similar distribution of parallel problems over many quantum computing devices. These criteria say that it must be possible to transfer the quantum state of the qubit from one location to another via a 'flying' qubit. Additionally, it must be possible to transfer the quantum state reliably between stationary qubits and flying qubits.

6. *"The ability to interconvert stationary and flying qubits"*

7. *"The ability faithfully to transmit flying qubits between specified locations"*

For quantum processing architectures such as superconducting Josephson junctions, the practicality of implementing large scale flying qubits between networked devices represents a significant technological challenge. In contrast, as nanophotonic circuits are designed to utilise photons as flying qubits on chip, they may also be used to transmit data over long distance in a similar fashion to that already used in fibre optic cables at telecommunication wavelengths (1300 nm and 1500 nm). Additional devices such as quantum repeaters [25] will be needed to overcome Compton scattering and dispersion in the signal over large distances as conventional amplification is prohibited due to the 'no cloning' theorem.

With significant work still remaining before a scalable nanophotonic quantum computer may be realised, the interest in long distance transmission of photons as flying qubits is primarily within the field of quantum key distribution. This area of research relies on the no cloning theorem and makes use of entanglement to transfer information between two locations in a secure manor. Recent achievements have shown through single photon correlation measurements that the quantum state of the photon can be preserved at

distances of up to 100 km [26], which is more than sufficient for simple quantum networks.

1.3. Quantum Dots

In nanophotonic circuits, an anti-bunched source of single photons is required in order to faithfully carry out quantum information processing. Quantum dots therefore represent an excellent source of single photons as they can be embedded directly within the nanophotonic circuits, improving overall efficiency. Additionally, the various excitonic configurations can be manipulated via the fabrication of diode structures, enabling the emission energy of the emitted photons to be precisely controlled [27] as well as the number of electrons trapped on the quantum dot, effectively providing a coulomb blockade controlling photon absorption. In this section, we give a brief overview of the opto-electronic properties of InGaAs quantum dots used in this thesis. Following this, a brief description of how QuBit states can be constructed is presented.

The InGaAs quantum dots used in this thesis are small islands of semiconductor material, typically 10's nm in size laterally, and 4 – 5 nm in height, composed of $\sim 10^5$ atoms [28]. The strong spatial confinement on the scale of the deBroglie wavelength for electrons results in the confinement of carriers to the quantum dot [16]. As a result, the electrons no longer experience the continuous band structure of the bulk semiconductor, but rather discreet energy levels form, with a splitting determined by the strength of the confinement potential in each of the spatial dimensions. As the quantum dots exhibit stronger confinement in the growth direction compared to the lateral dimensions, the solution to these energy levels may be approximated by considering a strong confinement potential in the growth axis, and a weaker, parabolic potential in the lateral plane [29]. The resulting transition between the continuous band structure of the bulk semiconductor material to that of the atomic like states for quantum dots is shown in Figure 1-2.

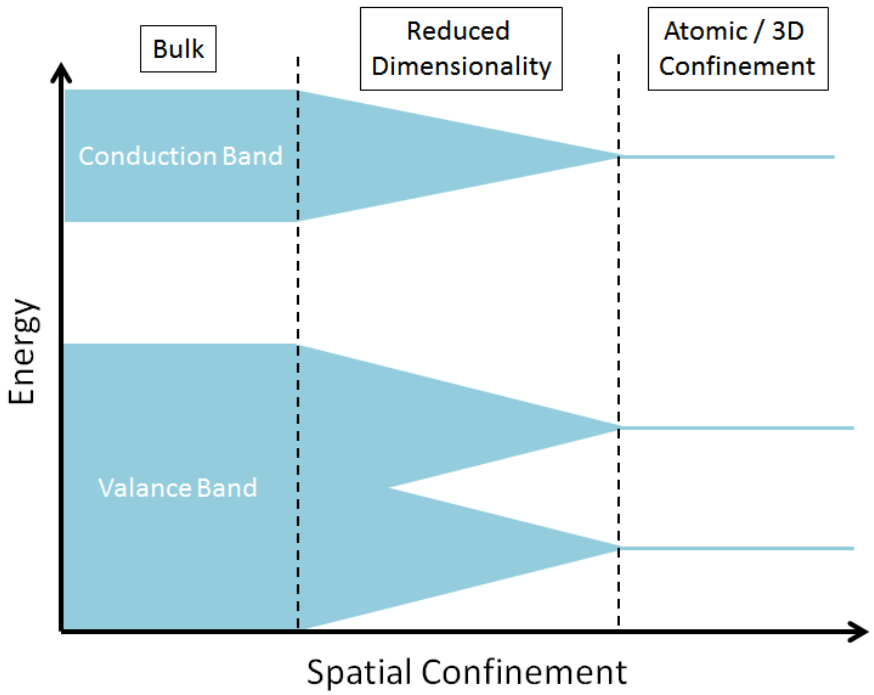

Figure 1-2 – Sketch depicting the transition from a continuum of states for a bulk semiconductor material towards atomic like discreet energy levels as the dimensions of the system are confined.

In order to consider the InGaAs quantum dots as two level systems which can be used as to construct QuBits, the transition between two discreet energy levels must be chosen. For the lowest level of the conduction band which an excited electron may occupy, a doublet state exists with s-type symmetry (S=1/2, S_z=±1/2). For InGaAs, the electron with the highest quantum angular moment in the valence band, and therefore the highest occupied energy level, has p-type symmetry with six fold spin degeneracy. These states can be separated into the spin doublet (S=1/2, S_z=±1/2) and quadruplet (S=3/2, S_z=±1/2 and S_z=±3/2). As a result of spin orbit coupling, the doublet state is split from the quadruplet state by several hundred meV and is referred to as the split off band. In a more complete picture, the interaction of additional bands, the effect of quantum confinement as well as strain within the quantum dot lift the energy degeneracy of the quadruplet state [28][30], resulting in a splitting of 10's meV between the S_z=3/2 and S_z=1/2 heavy hole and light hole bands respectively. A sketch of the resulting relative energy levels is shown in Figure 1-3.

The minimum energy transition for an electron in an InGaAs quantum dot is therefore from the heavy hole band to the ground state of the conduction band. The resulting transition leads to the formation of an exciton between the excited electron and newly created hole which form a quadruplet spin set which are:

Electron	Hole	Exciton Spin
$+1/2$	$+3/2$	$J = +2$
$+1/2$	$-3/2$	$J = -1$
$-1/2$	$+3/2$	$J = +1$
$-1/2$	$-3/2$	$J = -2$

Based on the total angular moment of the formed exciton, the quadruplet states can be split into two classifications, the bright and dark excitons. The states are named according to the optical selection rules which require conservation of angular moment when the electron and hole re-combine. Photons being bosons carry a total angular moment of 1, and therefore, the $J = \pm 2$ transitions are forbidden from emitting a photon.

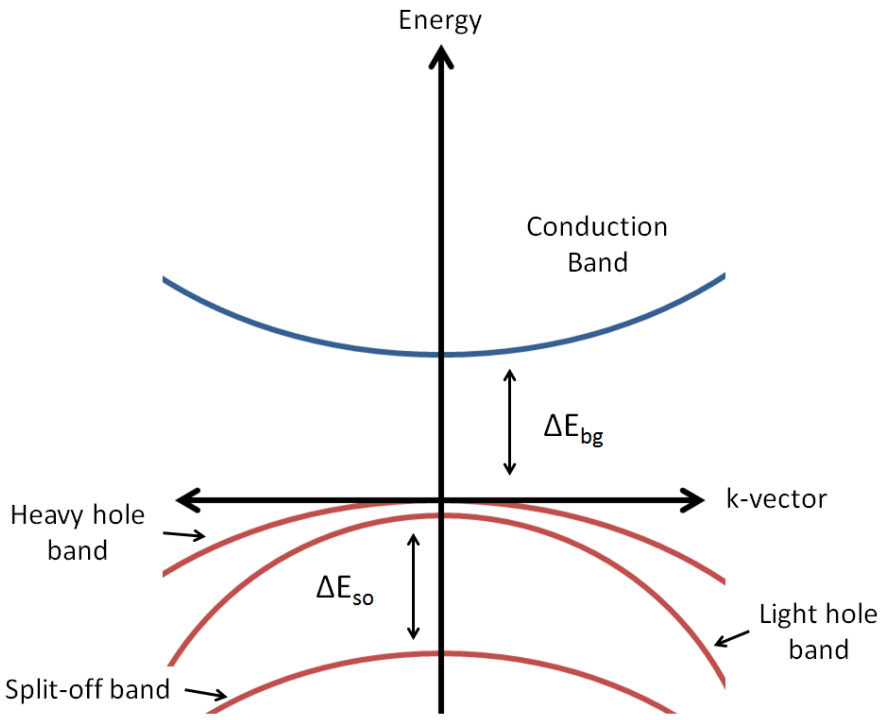

Figure 1-3 – Simplified band structure of InGaAs showing relative energy splitting of various valance band.

In an ideal quantum dot, the $J = \pm 1$ doublet is degenerate, however, due to anisotropic strain and asymmetry in the growth plane, the symmetry of the two wave functions is almost always lifted, resulting in a fine structure splitting typically no more than a few 10's of μeV's. As a result, the exchange interaction between the two pure states results in the formation of two new Eigenstates which are given by the superposition of the pure states, ${}^{1}/_{\sqrt{2}}|+1\rangle \pm |-1\rangle$. As the anisotropy in the quantum dot is between the [110] and [1$\underline{1}$0] crystal axis, photons emitted as a result of the recombination of these mixed states is linearly polarised along either of these crystal axes. Recently, the linearly polarised

emission as a result of fine structure splitting has been shown to be controllable through the use of novel piezo electric heterostructures which manipulate the strain profile of the quantum dot [31].

For the nanophotonic circuits discussed in this thesis, QuBits may be constructed in a variety of ways. One such method initially considered was in the spin state of electrons trapped on quantum dots [32]. Through techniques such as spin echo, it was considered that the coherence times of the spin state could be as long as µs for GaAs, many orders of magnitude longer than optical gate times. Unfortunately the interaction range of these QuBits is relatively short, and therefore attention turned to excitonic QuBits as stationary QuBits. The formation of a neutral exciton, and subsequent formations of charged and bi-excitons via the addition of subsequent electrons and holes to the quantum dot represent the building blocks which exciton QuBits may be formed.

Through control of the electron-hole spin, the spin state of the exciton can be controlled allowing the production of an exciton spin QuBit. Alternatively, the population of excitons can be used to construct QuBit states. Simply, it can be devised that the excited state of the QuBit is when an exciton is present, and the ground state is when the electron and hole have recombined. Alternatively, more complex systems can be constructed using the Bi-Exciton to Exciton transition. As only a single exciton can exist within the QD at any one time, the initialised ground state and the excited state can be considered two levels.

As the recombination of a bright exciton transition results in the emission of a photon, the QuBit state is persevered in the form of a flying QuBit. For spin QuBits, this information is encoded in the handedness of the emitted photon. Similarly, when the presence of an exciton is used as the basis for the QuBit state, the QuBit state is preserved via the presence or absence of an emitted photon.

1.4. Nanobeam waveguides

For nanophotonic circuits, there exist numerous novel photonic components which have been used to realise desirable manipulation of the photonic state, such as whispering gallery mode resonators [33], elongated nanowires [34], H1 photonic crystal cavities [35][36] and distributed Bragg reflector micro-cavities [37] to name a few. It is therefore not feasible to discuss each photonic component in any detail. However, the nanobeam waveguide is used extensively in the work presented in this thesis, and so a brief overview of its physical and optical properties is presented here.

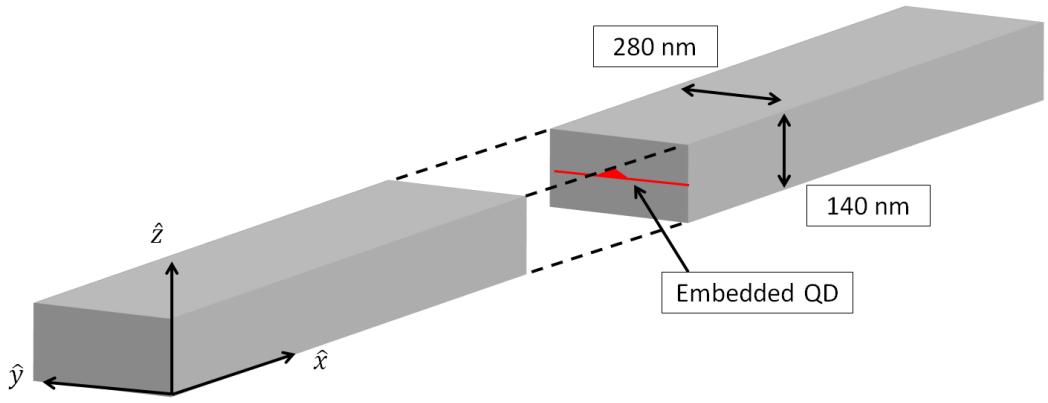

Figure 1-4 – Schematic showing 280 nm wide by 140 nm high GaAs waveguide with a quantum dot located at the centre. A vacuum cladding surrounding the GaAs provides an index contrast of $\sim \mathbf{3.4:1}$ *resulting in a critical angle of* $\sim \mathbf{17^o}$

The nanobeam waveguide is analogous to the metal wires which transport electrons in classical computers, as its primary purpose is to transport photons between photonic components with minimal losses or influence on the photonic state. Efficient confinement of the photonic state is achieved by using a high refractive index material to form the waveguide, where we use GaAs with a refractive index of ~ 3.4, and then remove the surrounding material so that it is vacuum clad, as shown in Figure 1-4. This results in a low critical angle of $\sim 17^o$. Dimensions for the single mode nanobeam waveguides used in this thesis are determined by finite difference time domain (FDTD) simulations by R. Coles [38]. The simulations were used to identify width and height of the waveguide which provided optimal coupling into the fundamental transverse electric field modes, which are calculated to be 280 nm by 140 nm respectively. Further details regarding the fabrication of the nanobeam waveguides is presented in Chapter 2.

Based on this design, simulations have shown that for the wavelength range of 900 nm to 950 nm, which is typical for the InGaAs quantum dots used, two fundamental transverse electric field modes are supported, referred to as TE_x and TE_y, with their electric fields aligned along the $\hat{x}$ and $\hat{y}$ axis (see Figure 1-4) of the waveguide respectively. The spatial profiles of the two optical field modes are shown in Figure 1-5, which show the presence of a node at the centre of the waveguide for the TE_x mode. A quantum dot 'ideally' located at the centre of the waveguide will therefore only efficiently coupled to the TE_y mode.

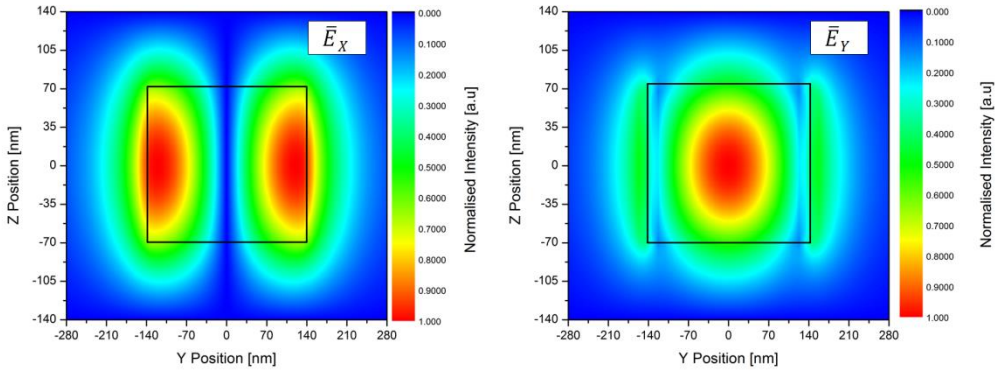

Figure 1-5 – Spatial profiles of the two fundamental transverse electric fields modes of a 280 nm wide and 140 nm high GaAs nanobeam waveguide.

Despite this fact, as the neutral exciton state typically experiences fine structure splitting which splits the two circularly polarised pure states into two mixed linearly polarised states, by aligning the waveguide to either the [110] or [1$\underline{1}$0] crystal axis, the overlap of one of these states with the TE_y mode can be maximised. For a quantum dot located at the centre of a waveguide, referred to as an 'L' point, it has been calculated that the coupling efficiency of a linearly polarised exciton state can be as high as 95% [38]. In order to couple circularly polarised light, the quantum dot must be laterally displaced in the waveguide such that the amplitude of the electric field of TE_x mode is non zero. Optimal coupling of circularly polarised light is achieved when the electric field amplitude of the TE_x mode is equal to that of the TE_y mode, referred to as a 'C' point. The overall coupling efficiency of circularly polarised light is determined to be $\sim 70\%$ [38]. Polarisation dependent coupling and propagation in nanobeam waveguides is the focus of experimental investigation in Chapter 4, where further details are provided.

1.5. Scope of thesis

With the above in mind, the work presented in this thesis looks to build on the existing work on scalable photonic circuits with embedded quantum dots, focusing in particular on two research areas; that of deterministic fabrication, and of exciton coherence lengths.

In Chapter 2, an overview of the wafer growth, device fabrication and the experimental setups used in subsequent chapters is presented. Specific details are given as to the setups of individual measurements which make use of novel equipment or experimental configurations.

In Chapter 3, the precision in which a quantum dot can have its position measured relative to a set of pre-fabricated markers when using a solid immersion lens is determined. Consideration is given to detrimental effects which the presence of a solid immersion lens may have on the both the sample and registration technique. The accuracy of the registration technique is used to determine how precisely a photonic structure can be deterministically fabricated around a quantum dot to achieve optimal performance.

Chapter 4 builds on the work of Chapter 3 and experimentally confirms the positional accuracy of the technique via several independent methods. Optical measurements are performed to characterise any changes in the spectral properties of the quantum dots as a result of the registration process or subsequent device fabrication. Further analysis of the spectral properties is used to confirm the quantum dot behaves as expected within the nanophotonic structure.

Chapter 5 explores the use of resonant excitation, as appose to above bandgap or quasi-resonant p-shell excitation, in order to increase the coherence length of photons. It is demonstrated that through a novel excitation regime, the laser signal can be strongly suppressed, whilst the resonantly excited quantum dot results in an efficient source of single photons emitted into the waveguide mode.

A brief summary of the key findings, as well as considerations for future work and foreseen challenges is presented in Chapter 6.

1.6. References

[1] G. Amaierako, L. Trabajo, and F. De Grado, “D-Wave quantum computer,” 2016.

[2] M. A. Nielsen and I. L. Chuang, “Quantum computation and quantum information,” *Am. J. Phys.*, 2002.

[3] R. P. Feynman, “Simulating physics with computers,” *Int. J. Theor. Phys.*, vol. 21, no. 6–7, pp. 467–488, 1982.

[4] P. Shor, “Polynomial-Time Algorithms for Prime Factorization and Discrete Logarithms on a Quantum Computer,” *SIAM J. Comput.*, vol. 26, no. 5, pp. 1484–1509, 1997.

[5] L. K. Grover, “Quantum Mechanics Helps in Searching for a Needle in a Haystack,” *Phys. Rev. Lett.*, vol. 79, p. 325, 1997.

[6] C. H. Bennett, “Notes on Landauer’s principle, reversible computation, and Maxwell’s Demon,” *Stud. Hist. Philos. Sci. Part B - Stud. Hist. Philos. Mod. Phys.*, vol. 34, no. 3, pp. 501–510, 2003.

[7] T. Toffoli, “Reversible computing,” *Computational Complexity: Theory, Techniques, and Applications*. pp. 2685–2701, 1980.

[8] L. M. Vandersypen, M. Steffen, G. Breyta, C. S. Yannoni, M. H. Sherwood, and I. L. Chuang, “Experimental realization of Shor’s quantum factoring algorithm using nuclear magnetic resonance.,” *Nature*, vol. 414, no. 6866, pp. 883–887, 2001.

[9] D. P. Divincenzo, “The Physical Implementation of Quantum Computation,” no. x, 2008.

[10] M. Felici, P. Gallo, A. Mohan, B. Dwir, A. Rudra, and E. Kapon, “Site-controlled InGaAs quantum dots with tunable emission energy,” *Small*, vol. 5, no. 8, pp. 938–943, 2009.

[11] P. Atkinson, S. Kiravittaya, M. Benyoucef, A. Rastelli, and O. G. Schmidt, “Site-controlled growth and luminescence of InAs quantum dots using in situ Ga-assisted deoxidation of patterned substrates,” *Appl. Phys. Lett.*, vol. 93, no. 10, pp. 91–94, 2008.

[12] J. Tatebayashi, Y. Ota, S. Ishida, M. Nishioka, S. Iwamoto, and Y. Arakawa, “Site-controlled formation of InAs/GaAs quantum-dot-in-nanowires for single photon emitters,” *Appl. Phys. Lett.*, vol. 100, no. 26, 2012.

[13] S. M. Thon, M. T. Rakher, H. Kim, J. Gudat, W. T. M. Irvine, P. M. Petroff, and D. Bouwmeester, “Strong coupling through optical positioning of a quantum dot in a photonic crystal cavity,” *Appl. Phys. Lett.*, vol. 94, no. 11, p. 111115, 2009.

[14] W. B. Gao, A. Imamoglu, H. Bernien, and R. Hanson, “Coherent manipulation, measurement and entanglement of individual solid-state spins using optical fields,” *Nat. Photonics*, vol. 9, no. 6, pp. 363–373, 2015.

[15] L. M. Duan and G. C. Guo, “Scheme for reducing decoherence in quantum computer memory by transformation to the coherence-preserving states,” *Chinese Physics Letters*, vol. 14, no. 7. pp. 488–491, 1997.

[16] I. I. Flagg Edward B., “Coherent control and decoherence of single semiconductor quantum dots in a microcavity,” 2008.

[17] C. Matthiesen, A. Vamivakas, and M. Atatüre, “Subnatural Linewidth Single Photons from a Quantum Dot,” *Phys. Rev. Lett.*, vol. 108, no. 9, pp. 1–4, Feb. 2012.

[18] M. N. Makhonin, J. E. Dixon, R. J. Coles, B. Royall, I. J. Luxmoore, E. Clarke, M. Hugues, M. S. Skolnick, and A. M. Fox, “Waveguide Coupled Resonance Fluorescence from On-Chip Quantum Emitter,” 2014.

[19] H. Takagi, T. Nakaoka, K. Watanabe, N. Kumagai, and Y. Arakawa, “Coherently driven semiconductor quantum dot at a telecommunication wavelength.,” *Opt. Express*, vol. 16, no. 18, pp. 13949–13954, 2008.

[20] H.-R. Wei and F.-G. Deng, “Scalable quantum computing based on stationary spin qubits in coupled quantum dots inside double-sided optical microcavities.,” *Sci. Rep.*, vol. 4, p. 7551, 2014.

[21] N. Prtljaga, C. Bentham, J. O’Hara, B. Royall, E. Clarke, L. R. Wilson, M. S. Skolnick, and A. M. Fox, “On-chip interference of single photons from an embedded quantum dot and an external laser,” *Appl. Phys. Lett.*, vol. 108, no. 25, 2016.

[22] I. J. Luxmoore, N. A. Wasley, A. J. Ramsay, A. C. T. Thijssen, R. Oulton, M. Hugues, S. Kasture, V. G. Achanta, A. M. Fox, and M. S. Skolnick, "Interfacing Spins in an InGaAs Quantum Dot to a Semiconductor Waveguide Circuit Using Emitted Photons," *Phys. Rev. Lett.*, vol. 110, no. 3, p. 37402, Jan. 2013.

[23] R. J. Coles, D. M. Price, J. E. Dixon, B. Royall, E. Clarke, P. Kok, M. S. Skolnick, A. M. Fox, and M. N. Makhonin, "Chirality of nanophotonic waveguide with embedded quantum emitter for unidirectional spin transfer.," *Nat. Commun.*, vol. 7, no. 2015, p. 11183, 2016.

[24] G. Reithmaier, S. Lichtmannecker, T. Reichert, P. Hasch, K. Müller, M. Bichler, R. Gross, and J. J. Finley, "On-chip time resolved detection of quantum dot emission using integrated superconducting single photon detectors.," *Sci. Rep.*, vol. 3, p. 1901, 2013.

[25] N. Sangouard, C. Simon, H. De Riedmatten, and N. Gisin, "Quantum repeaters based on atomic ensembles and linear optics," *Rev. Mod. Phys.*, vol. 83, no. 1, pp. 33–80, 2011.

[26] H. Takesue, S. D. Dyer, M. J. Stevens, V. Verma, R. P. Mirin, and S. W. Nam, "Quantum teleportation over 100 km of fiber using highly efficient superconducting nanowire single-photon detectors," *Optica*, vol. 2, no. 10, p. 832, 2015.

[27] O. Couto, J. Puebla, E. Chekhovich, I. Luxmoore, C. Elliott, N. Babazadeh, M. Skolnick, A. Tartakovskii, and A. Krysa, "Charge control in InP/(Ga,In)P single quantum dots embedded in Schottky diodes," *Phys. Rev. B*, vol. 84, no. 12, pp. 1–7, Sep. 2011.

[28] A. N. Vamivakas and M. Atatüre, "Photons and (artificial) atoms: an overview of optical spectroscopy techniques on quantum dots," *Contemp. Phys.*, vol. 51, no. 1, pp. 17–36, Jan. 2010.

[29] G. Bester, S. Nair, and A. Zunger, "Pseudopotential calculation of the excitonic fine structure of million-atom self-assembled 1-xGa xAs/GaAs quantum dots ," *Phys. Rev. B*, vol. 67, no. 16, p. 161306, 2003.

[30] Y. H. Huo, B. J. Witek, S. Kumar, R. Singh, E. Zallo, R. Grifone, D. Kriegner, R.

Trotta, N. Akopian, J. Stangl, V. Zwiller, G. Bester, A. Rastelli, and O. G. Schmidt, "Semiconductor quantum dots with light-hole exciton ground state: fabrication and fine structure," *arXiv Prepr. arXiv*, p. 16, 2012.

[31] J. Zhang, E. Zallo, B. Höfer, Y. Chen, R. Keil, M. Zopf, S. Böttner, F. Ding, and O. G. Schmidt, "Electric-field-induced energy tuning of on-demand entangled-photon emission from self-assembled quantum dots," p. 12, 2016.

[32] T. D. Ladd, F. Jelezko, R. Laflamme, Y. Nakamura, C. Monroe, and J. L. O'Brien, "Quantum Computing," 2010.

[33] K. Srinivasan and O. Painter, "Linear and nonlinear optical spectroscopy of a strongly coupled microdisk–quantum dot system," *Nature*, vol. 450, no. 7171, pp. 862–865, 2007.

[34] A. P. Foster, J. P. Bradley, K. Gardner, A. B. Krysa, B. Royall, M. S. Skolnick, and L. R. Wilson, "Linearly polarized emission from an embedded quantum dot using nanowire morphology control," *Nano Lett.*, vol. 15, no. 3, pp. 1559–1563, 2015.

[35] I. J. Luxmoore, E. D. Ahmadi, A. M. Fox, M. Hugues, and M. S. Skolnick, "Unpolarized H1 photonic crystal nanocavities fabricated by stretched lattice design," *Appl. Phys. Lett.*, vol. 98, no. 4, p. 41101, 2011.

[36] C. Bentham, I. E. Itskevich, R. J. Coles, B. Royall, E. Clarke, J. O'Hara, N. Prtljaga, A. M. Fox, M. S. Skolnick, and L. R. Wilson, "On-chip electrically controlled routing of photons from a single quantum dot," *Appl. Phys. Lett.*, vol. 106, no. 22, p. 221101, 2015.

[37] A. Muller, E. B. Flagg, P. Bianucci, X. Y. Wang, D. G. Deppe, W. Ma, J. Zhang, G. J. Salamo, M. Xiao, and C. K. Shih, "Resonance Fluorescence from a Coherently Driven Semiconductor Quantum Dot in a Cavity," *Phys. Rev. Lett.*, vol. 99, no. 18, pp. 2–5, Nov. 2007.

[38] R. J. Coles, "Quantum Optical Circuits using III-V Nanophotonic Structures," no. April, 2015.

2. Experimental Methods

2.1. Introduction

An overview of fabrication and experimental techniques is presented in this chapter. Three fundamental experimental areas are discussed; quantum dot growth, wafer processing and photoluminescence measurements.

2.1.1. Acknowledgments

It is acknowledged here that the growth of quantum dots used in this thesis was performed by E. Clarke. Subsequent wafer processing and fabrication were jointly carried out with the support of B. Royall.

2.2. Sample Growth

The InGaAs self-assembled Quantum Dots (QDs), embedded within a GaAs matrix, used in this thesis are ideally suited as a platform for quantum information processing due to the inherent scalability and utilisation of well-established semiconductor technologies. These InGaAs QDs are grown in bespoke heterostructures by 'Molecular Beam Epitaxy' (MBE).

2.2.1. Molecular Beam Epitaxy

In order to produce quantum dots with a well-defined size and number density, rotation stop molecular beam epitaxy is used. For a more comprehensive study of MBE technology and theory, the reader is referred to the following sources [1], [2]. As an introduction to the work presented, a brief overview of MBE is discussed.

MBE was developed by A. Y. Cho and J. R. Arthur around the start of the 1970's at Bell Laboratories [3], and has since been widely adopted in the production of semiconductor devices. The success of the technology is in part due to the range of materials which can be deposited, and the level of control that can be achieved. By independently varying the flux of separate elements, the composition of the layers grown can be precisely controlled. Further, the rate of growth can be tailored so that it is possible to achieve control down to individual monolayers of growth [4].

To start the growth process, first an initial wafer with a so called 'epi ready' surface is required for material to be grown on. The surface quality of this wafer can dramatically affect the growth of subsequent layers of materials, and so great lengths are taken to ensure it is free of oxides, contaminants or morphological imperfections [5]. Epi ready GaAs wafers are used to fabricate the quantum dots for this work, with major and minor flats used to mark the $[110]$ and $[1\bar{1}0]$ crystal axes. This host wafer is loaded into the MBE ultra-high vacuum chamber, with typical pressures of less 10^{-8} Pa, to prevent contamination which may otherwise adversely affect the growth [6]. Material deposition is achieved through the evaporation of highly pure elements located in effusion cells surrounding the wafer chamber. The flow rate of the molecular beam is then controlled through a combination of temperature and mechanical shutter plates [6][7].

In order to ensure a uniform growth across the sample, it is common for the host wafer to be rotated during growth. As we however require varying densities of quantum dots from the same hetero-structure devices, rotation of the host wafer is stopped during the quantum dot growth layers. As a result, more material is deposited on the side of the wafer closer to the evaporation cell, and therefore gives a higher density of quantum dots.

2.2.2. Stranski-Krastanov Growth

In molecular beam epitaxy, there are three primary growth methods which can occur; Volmer-Webber (VW) growth which results in discreet island formation, Frank-van der Merwe (FM) growth which results in uniform layers, and Stranski-Krastanov (SK) growth which results in both layer and island formation [8][9]. The quantum dots used in this thesis are the result of island formation from the SK growth of indium arsenide on gallium arsenide.

The growth regime which occurs during MBE is highly dependent on the inherent properties of the materials being grown. For the case of SK growth of InAs on GaAs, the surface adhesion energy is initially dominant, and so adatoms preferentially adhere to the GaAs surface. This initially results in monolayer growth. As the lattice constant of InAs and GaAs are significantly different, with a mismatch of approximately 7% , the strain energy in the monolayers quickly increases [10]. After a critical film thickness, nominally a few monolayers for InGaAs, the strain energy term becomes dominant, and therefore

favourable for island formation growth to occur as it allows the strained bonds to relax and more closely approximate their intrinsic bond length.

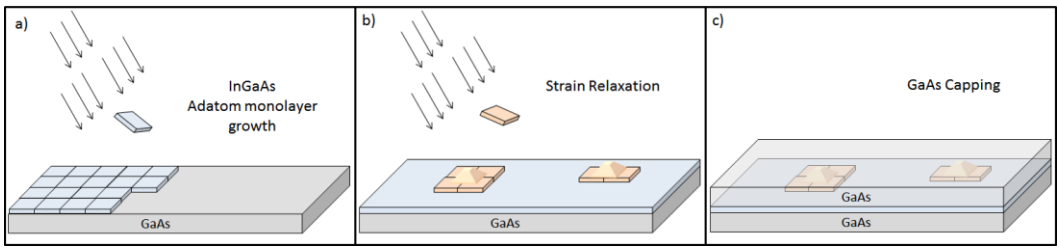

Figure 2-1 – (a) Initial monolayer growth process during MBE for Stranski-Krastanov growth conditions. Adatoms preferential bond to vacancy's forming uniform crystal layers. (b) The strain energy becomes greater than surface adhesion potential resulting in nucleated growth of islands. (c) SK growth is stopped after a predefined thickness is reached and GaAs is grown on top of the QDs to protect the surface.

For InGaAs, these islands are typically tens of nanometres in size laterally, and a few nanometres in height, which is comparable to the de Broglie wavelength of free carriers in the surrounding bulk semiconductor [11]. The three dimensional confinement of carriers to these islands therefore provides an easily accessible platform to investigate quantum affects.

2.2.3. Heterostructures

As described in §2.2.1, MBE allows for precise control over the size and composition of a fabricated structure. For devices studied in this thesis, a standard 140 nm thick membrane recipe is used, with a cross section presented in Figure 2-2.

In order to relax strain and prevent defects from propagating to the quantum dot layers, a 500 nm thick buffer layer of GaAs is first grown. A second layer, 1 µm thick, of $Al_{0.6}Ga_{0.4}As$ is then deposited as a sacrificial layer. The purpose of this layer is to be selectively removed at a later point during fabrication. The final layers, which will be referred to as the 140 nm thick membrane, consist of QDs and the wetting layer clad either side by 70 nm of GaAs.

This heterostructure is used to fabricate nanobeam waveguide photonic circuits as it provides the basis for one dimension confinement of the optical mode in the growth axis. By removing the sacrificial layer below the membrane layer, the dielectric contrast between the membrane layer and its surroundings is significantly increased. For InGaAs quantum dots, with typical emission energy of 1.347eV (900 – 950 nm), the 140nm thick

membrane represents a half wavelength, and therefore optimal confinement of photonic modes for devices such as nanobeam waveguides [12]. It is therefore possible to achieve three dimensional confinement (growth axis plus two in plane axis) of photons by using standard two dimensional lithographic processes (see section 2.3).

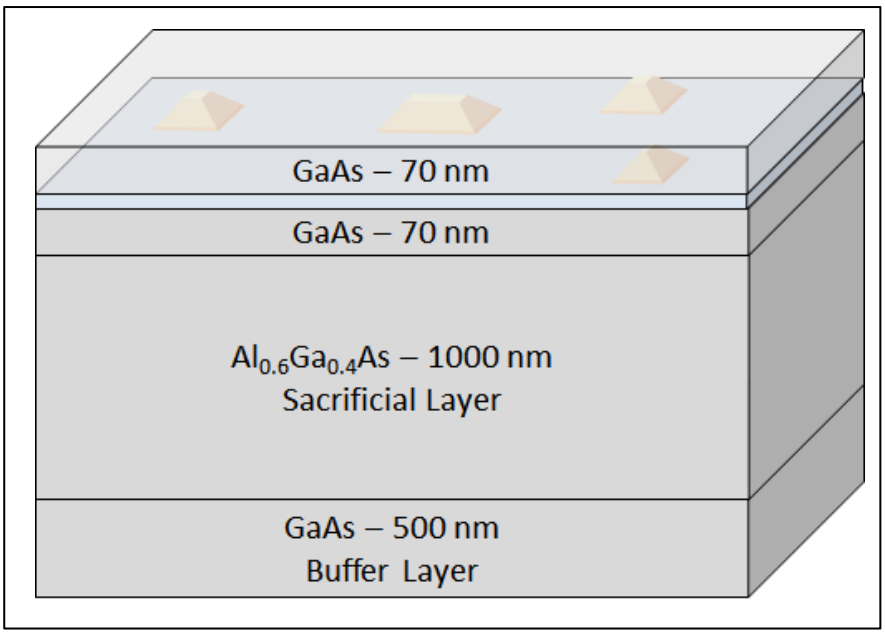

Figure 2-2 – A sketch of quantum dots (red), exaggerated in size, are shown on top of the wetting layer (blue) located at the centre of the 140 nm thick membrane, composed of two 70 nm thick GaAs cladding layers. The $Al_{0.6}Ga_{0.4}As$ sacrificial layer is shown between the 140 nm thick membrane layer and the 500 nm GaAs buffer layer.

2.3. Device Fabrication

To produce the different structures used in thesis, a wide range of fabrication techniques are required. An overview of the wafer processing steps is given here and covers the general principles required to fabricate most of the photonic structures examined. Where the fabrication methods have been modified, details will be given in the relevant chapter. An example of a nanobeam waveguide, which requires several etching processes, and gold registration markers, which require metal evaporation, is shown in *Figure 2-3*.

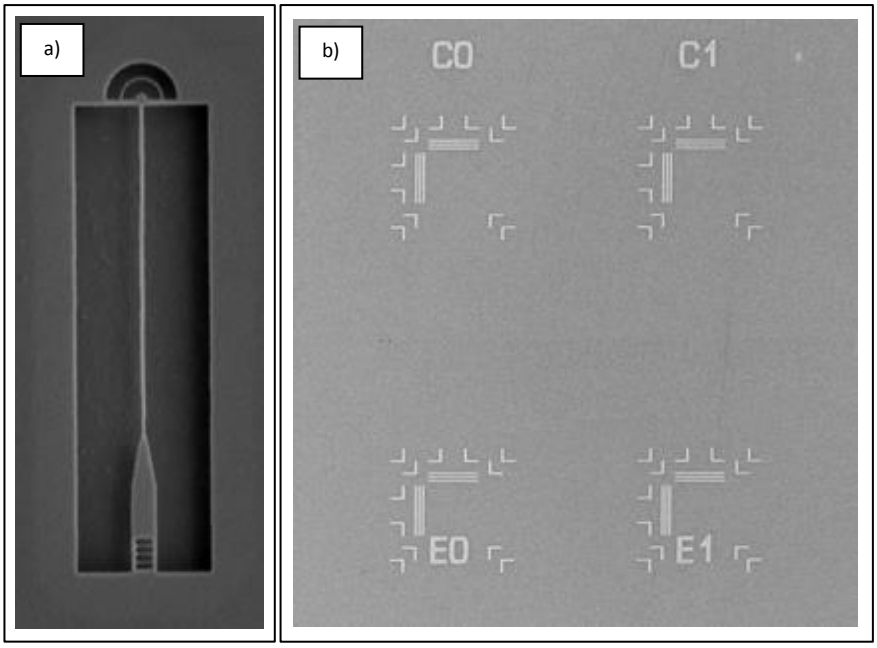

Figure 2-3 – (a) SEM image showing an under etched nanobeam waveguide with two types of distributed brag reflectors at the top and bottom. (b) SEM image showing horizontal and vertical gold markers evaporated onto the wafer surface to be used for dot registration.

2.3.1. Spin Coating

Spin coating is a well-established technology predominantly used in the fabrication of thin films, with achieved minimum film thicknesses of less than 10 nm. Due to the simple relation between the film thickness to viscosity and angular velocity, the technique is considered more reproducible than alternatives, such as dip coating [13].

Spin coating is used here to reproducibly, and uniformly, cover the surface of a wafer in the electron beam resist, ZEP520a. To ensure the electron beam resist adheres to the wafer surface, hexamethyldisilazane is first applied as a bonding agent. It was found that without the use of a bonding agent, the ZEP520a would lift off during subsequent etching processes. The hexamethyldisilazane is applied with a spin speed of 5000 rpm, and due to the volatility of the solvent, no baking is required.

ZEP520a is then pipetted onto the samples surface which is spun again, also at 5000 rpm. The wafer is this time baked at 180^{o}C for 5 minutes to cure the resist. To ensure consistent fabrications, periodic measurements of the film thickness were performed using a Dektak. The standard film thickness was found to be 320nm which is sufficient to withstand the required etching processes.

Due to the sensitivity of ZEP520a to oxidation and ultraviolet light, samples were prepared in a yellow room directly before being used. When samples needed to be transported, they were done so in sealed, dark containers.

2.3.2. Electron Beam Lithography

Electron Beam Lithography (EBL) is used to transfer the 2D pattern of bespoke photonic structures into the surface of the ZEP520a. During exposure of the ZEP520a, the polymer undergoes chain-scission [14], increasing its solubility with respect to a given solvent. As ZEP520a is a positive resist, any areas which are exposed and subsequently developed, are removed leaving the bare wafer surface exposed.

The performance of a photonic structure, such as an out-coupler at the end of a nanobeam waveguide, can be highly dependent on several critical dimensions. There is unfortunately an inherent 'blurring' which occurs during the patterning of photonic structures due to the backscattering of electrons within the GaAs leading to the proximity effect of the electron beam. Proximity error correction is therefore required to ensure the pattern transferred to the wafer accurately represents that of the desired pattern. This is achieved by discretising the desired pattern and scaling the exposed dose to suitably account for neighbouring exposures.

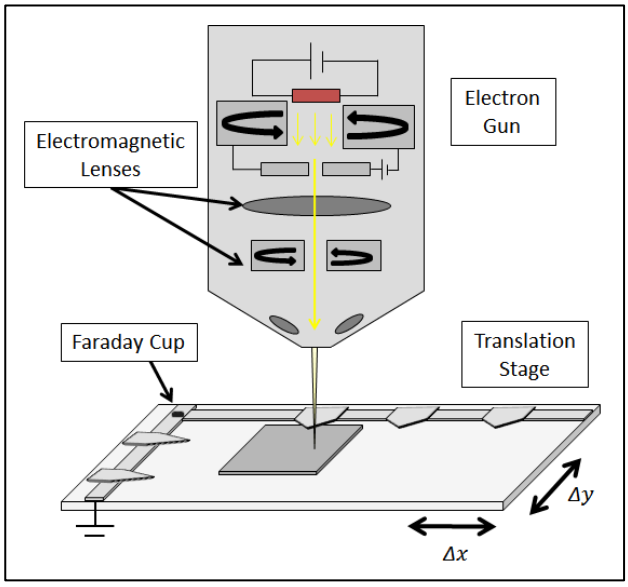

Figure 2-4 – Schematic of Raith150 EBL system with a sample mounted on a feedback controlled translation stage. After initial sample positioning using the interferometer controlled translation stage, the electron beam can be deflected to expose various areas of the sample using a series of electromagnetic lenses.

A Raith150 EBL system, as shown in Figure 2-4, is used to write the 2D patterns using a computer aided design (CAD) software. When the sample is loaded into the EBL system, it is grounded using a metal contact to prevent excessive charging. It is observed that near the metal contact, deflection of the EBL beam occurs, likely due to a nonlinear charge distribution in the sample. As this area is typically quite small, this area of the wafer is avoided during exposures.

The electron gun is operated at 30keV in order to minimise the backscattered electron dose contribution during sample exposures. A faraday cup is used prior to each exposure to calibrate the electron fluence, which slowly degrades over the electron guns service life. For a given writing field of 50 µm by 50µm, a combination of magnetic and electric deflection coils and lenses are used to position the electron beam. A typical write speed of > 5 mms^{-1} is achieved, with a minimum step size of 4 nm, which enables a 15µm long waveguide to be exposed in less than 1 minute.

2.3.3. Developing

After exposing the resist using electron beam lithography, the sample is developed to remove the areas of the resist which were exposed. The wafer is placed in a Xylene bath at 23^{o}C for 60 seconds, and then thoroughly rinsed in isopropyl alcohol.

Although the physical pattern has been transferred to the resist, thermal fluctuations can cause the remaining resist to warp. Any subsequent processing steps are therefore carried out immediately.

2.3.4. Etching

To fabricate 3D photonic structures, such as those shown in *Figure 2-3*, two separate etching techniques are required; a dry etch and a wet etch. An inductively coupled plasma (ICP) dry etch is first performed to etch down through the 140nm thick membrane layer to a midpoint in the sacrificial layer. A wet, hydrofluoric acid etch is then used to selectively remove the sacrificial layer

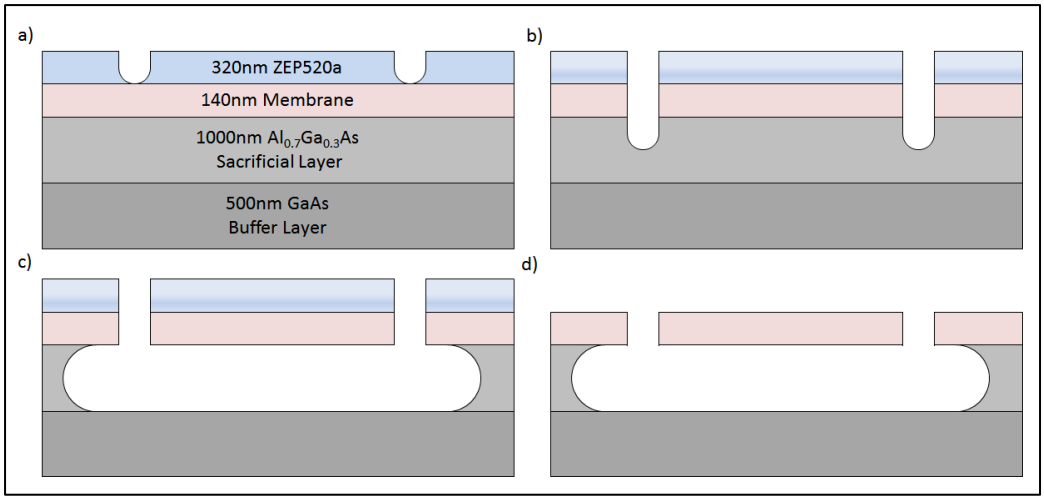

Figure 2-5 - Process diagram showing the four etching steps required to fabricate free standing photonic structures. a) Initial sample with developed resist leaving exposed areas of the wafer surface in the desired pattern. b) ICP $SiCl_4$ dry etch is used to chemically etch through the 140nm membrane and partially into the sacrificial layer. c) Wet HF acid etch selectively removes the sacrificial layer through exposed channels in the membrane layer. d) The resist layer is removed leaving the fabricated free standing photonic structure.

ICP etching uses a radio frequency (RF) electrical current to inductively ionise an etchant within the sample chamber. These freed electrons are rapidly accelerated by the induction coils, at which point, depending on the phase of the RF signal, are either removed from the chamber or attach to the sample causing it to charge. The remaining ionised species, due to the relatively heavy mass, are not so readily accelerated by the RF field. They are however accelerated towards the sample by the quasi static field caused by the charged sample. As the ionised etchants hit the sample nearly normal to the surface, it is possible to fabricate high aspect ratio structures with nearly vertical side walls.

An etch recipe using silicon tetrachloride ($SiCl_4$) with a flow rate of 5 sccm at a pressure of 2mTorr and a temperature of 20°C was employed. The RF power is measured to be 180W with an interferometer measured etch rate of 450nm/min through GaAs. Silicon tetrachloride is advantageous for etching GaAs, as opposed to alternatives such as argon [15][16], as it etches via a chemical reaction rather than sputtering material. The key benefit of chemical etching being that it produces smother surfaces, and so high quality photonic structures can be fabricated [17].

Once the sacrificial layer has been exposed through etching, the electron beam resist is no longer needed as the 2D pattern has been transferred into the GaAs membrane. The

remaining ZEP520a is removed using 1-2-Methyl-Pyrrolidone, followed by a series of solvent baths, leaving a clean, uncontaminated, surface ready for the second wet etch.

A 40% solution of hydrofluoric acid, by volume, is used to selectively etch the $Al_{0.6}Ga_{0.4}As$ sacrificial layer. Although hydrofluoric acid etches the sacrificial layer significantly quicker than the GaAs membrane layer, there is a non-negligible measured effect on the width of photonic structures if they are left in the hydrofluoric acid for extended periods of time. It was found that 15 seconds was sufficient time to remove the 1µm thick sacrificial layer, which typically resulted in only a few nanometres of etching in the GaAs membrane.

To prevent further etching, and crucially to prevent the collapse of the any free standing photonic structures, the sample is immediately placed in deionised water and then acetone. Critical point drying is then used to remove the acetone, by displacing it with carbon dioxide, such that no change in surface tension occurs that would otherwise destroy the free standing structure [18].

2.4. Cryostats

Optical measurements of samples are conducted in either a continuous flow cryostat or a bespoke bath cryostat at temperatures of 4 K. Whilst some of the optics, such as spectrometers and avalanche photo diodes (APDs), are shared between the two setups, there remain several significant differences which warrant separate discussion.

2.4.1. Continuous flow cryostat

Due to the active cooling required in a flow cryostat system, it is inherently less mechanically stable than a bath cryostat. It does however allow samples to be changed quickly, which is ideal for characterisation, or dot registration purposes. As such, it is possible to make small adjustments to the sample at room temperature between measurements. To achieve sufficient mechanical stability, an oxford instruments 'MicrostatHiRes2' continuous flow liquid helium cryostat is used, as shown in Figure 2-6.

The key to the MicrostatHiRes2's mechanical stability is the use of capillaries to transport helium through the heat exchange where the sample is mounted. By physically separating the transfer tube and the capillaries, high frequency vibrations are prevented from reaching the sample. Conventionally, liquid helium coolant is pulled through the cryostat into the return line using a motorised pump, however this also introduces additional

sources of vibrations which are detrimental to stability. Therefore, when stability is paramount, an alternative push method is used. This method requires, an overpressure in the liquid helium Dewar which forces the coolant through the cryostat to the return line. Care is taken with this method to ensure the temperature is stable as it is subject to pressure fluctuations.

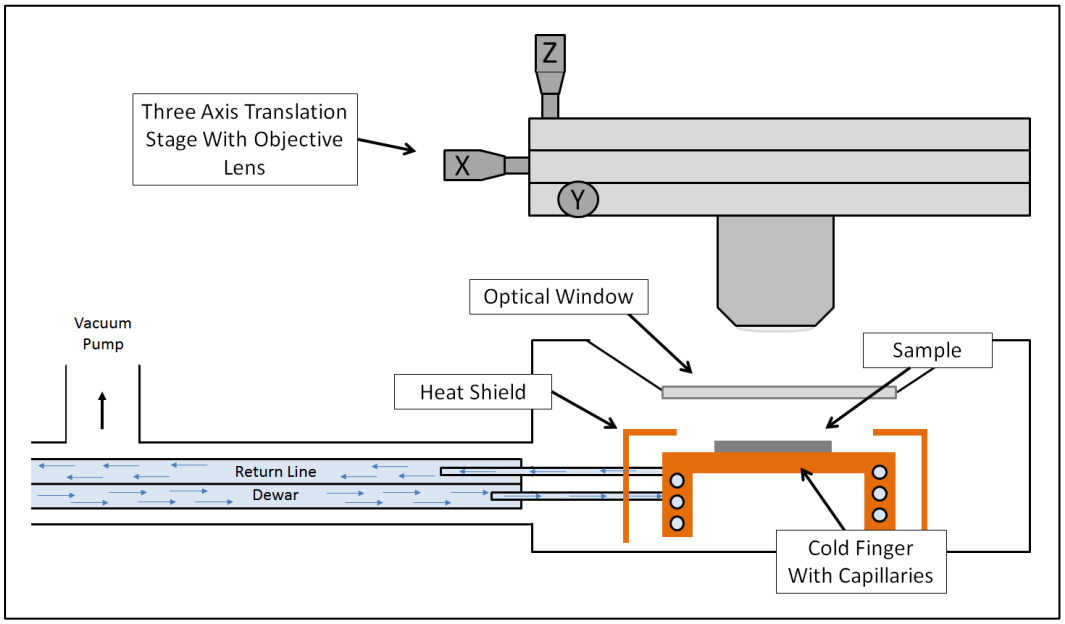

Figure 2-6 – Diagram showing the internal mechanics of the 'Microstat HighRes2' flow cryostat. A sample is shown mounted on a copper cold finger with capillaries running through it to transport liquid helium coolant. Capillaries are mechanically isolated from the helium transfer tube to minimise vibrations in the sample. An objective lens is shown mounted above the cryostat on a 3 axis translation stage with micrometre screws for positioning the excitation and collection spot.

For increased versatility, two excitation and two collection paths are mounted above the cryostat using breadboards as shown in Figure 2-7. A range of 92:8 and 50:50 transmission to reflection pellicle and cubic beam splitters are used, interchangeably, to divert the optical paths and maintain high, balanced signal levels. A significant advantage to multiple excitation and collection paths is that multiple locations on the sample can be probed simultaneously. By using remote controlled stepper motors attached to kinematic mirrors, the excitation and collection spots can be precisely controlled with a minimum estimated deflection of 0.5 nm to the optical beam.

To enable the use of the stepper motors, the objective lens must first be placed above the desired location on the sample. This is achieved with the use of a course, $1 \mu m$ resolution, three axis translation stage with a total travel distance of 12mm. A built in,

closed loop, piezoelectric translation mechanism, with a resolution of 1nm, and a maximum travel distance of 100 μm increases the functionality of the stage so that it is possible to reproducibly navigate around the sample.

Excitation lasers are coupled into single mode fibre optic cables, with a core diameter of approximately 5µm, and are collimated by a 10x magnification objective lens before passing through any other optical elements. This provides a small Gaussian beam which can be effectively focused onto the sample, using a 50x objective lens, resulting in an excitation spot roughly 500 nm in diameter. Scattered laser light and quantum dot photoluminescence is collected into single mode fibre optic cables with the use of additional 10x magnification objective lenses. By matching the magnification to the core diameter, as well as choosing an appropriate numerical aperture (0.14 for near infrared single mode fibres), signal collection efficiency into the fibre in excess of 80% is possible[1].

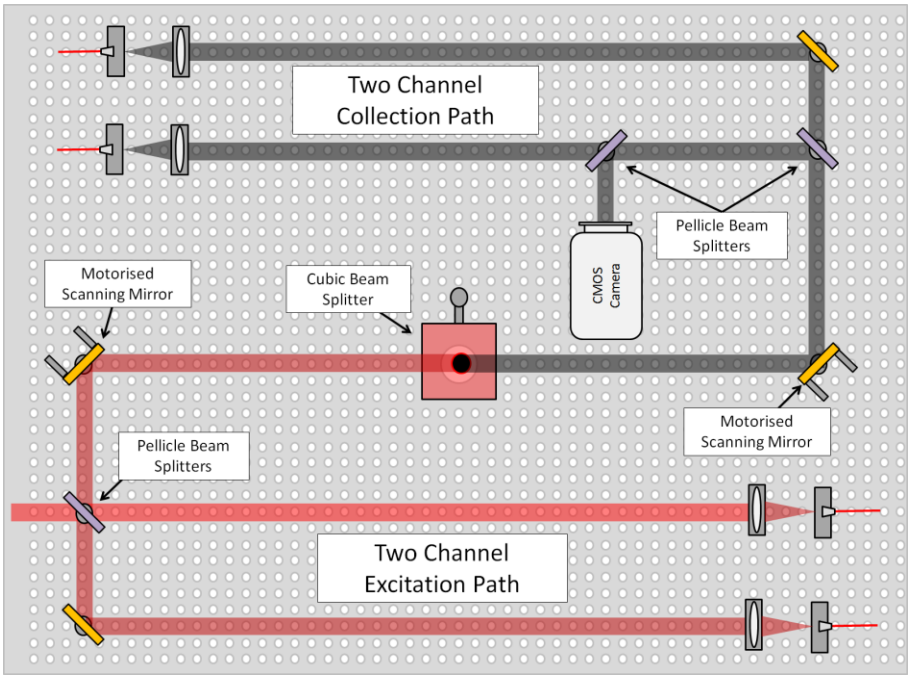

Figure 2-7 – Sketch showing optical setup mounted on a breadboard typically used for excitation and collection of photoluminescence of the flow cryostat system. Two fibre coupled excitation lasers are shown to be partially reflected by a cubic beam splitter onto the samples surface. Transmitted light is detected by a power meter to determine the excitation power. The photoluminescence channel is shown to be split by a pellicle beam splitter and coupled into two separate single mode fibre optic cables.

[1] Collection efficiency is determined by measuring the power before and after coupling into the fibre has occurred using a reference single mode infra-red laser.

Due to the properties of total internal reflection, any light coupled to the cladding will not couple to the core due to its lower refractive index, but rather will just pass through it. This results in a top hat convolution of the point spread function for the coupling efficiency of the incident photons to the fibre optic cable, analogous to that used in confocal microscopes. As a result we claim a spatial resolution of 500 nm on the sample surface, which for typical samples observed is more than sufficient to isolate individual quantum dot lines and distinguish geometric features of photonic structures. We do however acknowledge that due to scatter surfaces, both in the fabricated structures and optical equipment, some level of noise is coupled to the collection fibre.

2.4.2. Bath Cryostat

The use of fibre optic cables provides a versatile platform from which to probe the properties of photoluminescence and study photonic structures. As previously stated, up to 80 % of the collected signal can be coupled into a single mode fibre, however, when the initial signal intensity is low or highly sensitive to environmental factors, it can be difficult to distinguish weak signals with respect to background without the use of a bath cryostat. This is because the use of a bath cryostat significantly reduces the vibrations, as a result of no longer actively pumping liquid helium through a cold finger, which would typically result in the continuous drifting of the sample with respect to the excitation and collection points. It is therefore possible to maintain cryogenic temperatures for extended periods, enabling long signal integration times to be used.

A bath cryostat, as shown in Figure 2-8, is fundamentally a liquid helium Dewar that has been extensively modified to support an optical insert, and typically with a breadboard supporting excitation and collection optics atop of it. Whilst the design used here is similar to most commercial systems available, it is important to distinguish it from the flow cryostat described in the previous chapter.

A three inch diameter hollow insert is used to contain optic elements, such as lenses, as well as piezo electric translation stages and multiple samples. The insert is sealed with a 'Spectrosil B' optical window and pumped down to pressures of 10^{-6} Bar to remove contaminants. Although it will ultimately be immersed in a bath of liquid helium, the high thermal conductivity, and its contact with Dewar housing, would prevent a sample from reaching cryogenic temperatures. For this reason, a small amount of exchange gas is introduced, in the form of Helium gas. Helium is chosen over alternative exchange gases

as they would likely condense or freeze on the surface of the insert, optics or sample once immersed. Additionally, because of its low mass, it also has a high thermal conductivity which helps achieve lower temperatures, despite the metal insert being directly exposed to room temperatures.

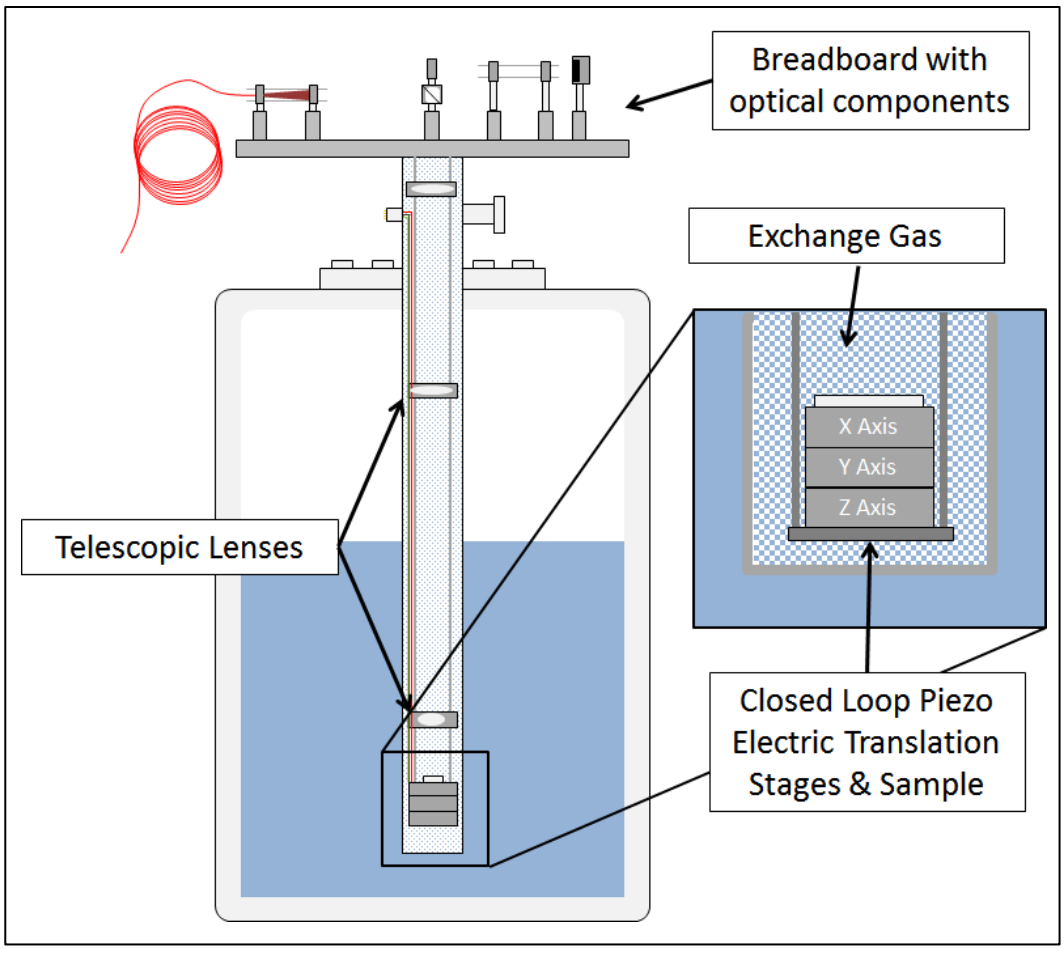

Figure 2-8 – Sketch showing interior of bath cryostat with optical insert. A sample is shown mounted on three orthogonal piezoelectric translation stages at the bottom, suspended via a rail system attached at the top of the insert to reduce the thermal contact area. Two telescopic lenses are shown in the optical insert which are used to maintain collimation of the beam through a broad chromatic range.

In order to position the sample once it is inside the cryostat, three piezo electric linear translation stages are mounted orthogonally on top of each other. Each translation stage is operated in an open loop circuit with a maximum travel distance of 5mm. By mounting the sample on the top of the piezo stack, it is possible to navigate around the sample to probe various features, as well as compensate for focal length changes.

A sketch of the bath cryostat system is shown in Figure 2-8 showing a Dewar with the optical insert inside it and a bread board mounted on top. No details regarding the two

channel excitation and collection optics for the bath cryostat are given here as they are much the same as those used for the flow cryostat, as shown in Figure 2-7.

2.5. Optical Measurements

As described above, samples may be studied in either a continuous flow or bath cryostat. Each of these setup makes use of fibre optic cables, allowing for a 'plug and play' approach to optical measurements. The following experimental setups are therefore shared between the two cryostats by changing which fibre optic cable is connected.

2.5.1. Spectral Analysis and Filtering

Observing the spectral properties of quantum dots is a fundamental measurement required to characterise both the quantum dot and the performance of photonic structures they may be embedded in.

The spectrometer used is a Princeton Instruments SP2750 with a focal length of 75 cm. A range of gratings are supported, although typically a high resolution 1200 line per mm grating is used with a blazing optimised for 750 nm. A Pylon CCD with a 1340 x 100 array of 20 x 20 μm^2 sized pixels is used to detect the filtered signal with a peak resolution greater than 0.02 nm at 920nm. This provides a spectral window of slightly more than 20 nm.

In addition to measuring the spectral properties directly, a side exit slit on the spectrometer allows for the filtered signal to be studied using additional experimental equipment, such as APD's and single photon counting modules for experiments such as lifetime measurements. By varying the width of the exit slit, it is possible to control the output spectral bandwidth. As quantum dot lines tend to be well isolated in energy from other spectral signals, such as the GaAs band gap or the so called wetting layer, a spectral bandwidth up to 1 nm is often used. These larger bandwidths are chosen in order to preserve signal intensity which may have otherwise been lost due to geometric or chromatic aberrations as a result of optics in the spectrometer.

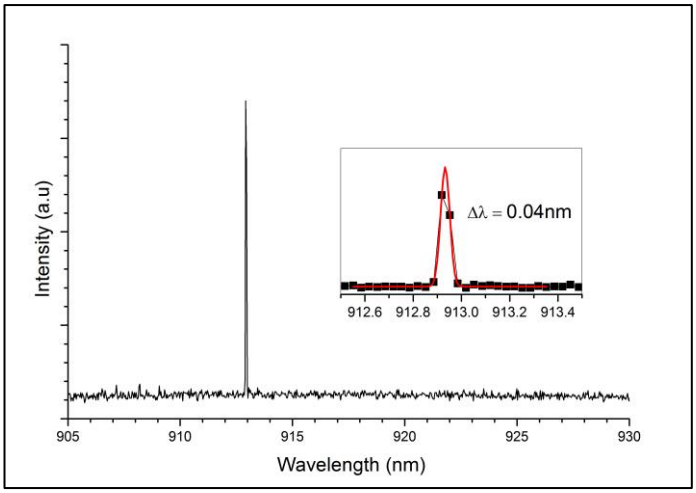

Figure 2-9 – Example spectrum showing isolated quantum dot signal with near resolution limited linewidth

Maintaining a high signal level is a key challenge when studying quantum dots, especially when studying sensitive properties such as photon correlation statistics, with a measurement time which varies with the square of the signal intensity. As described above, the spectrometer may be used to filter quantum dot signals. This method is however inherently lossy, with typically 50% loss arising from the spectral filtering process and a further 80% loss when the signal is coupled into the collection fibre. Alternatively, if the quantum dot selected is sufficiently well isolated, a range of fixed band-pass filters may be used. This reduces the total signal loss by comparison from 60% due to the spectrometer to as little as 35%.

2.5.2. Michelson Interferometer

An area of keen interest in quantum dots is that of the coherence time of the photons emitted from the relaxation of excitonic states. Whilst it is possible to infer the coherence length of the photon from an accurate measurement of the spectral linewidth, this can be experimentally challenging due to the high spectral resolution required, and may not provide the true coherence length.

In order to determine the coherence time of the emitted photons, the first order correlation function is directly measured using a Michelson Interferometer. The Michelson Interferometer is a special configuration of optical elements designed to remove any spatial dependence from the first order correlation function. This is done by splitting the optical signal into two paths, and varying the path length of one arm with respect to the other before recombining the two signals. To ensure all spatial dependence

is removed, the two optical paths must be recombined parallel to each other with no spatial offset, as is shown in Figure 2-10.

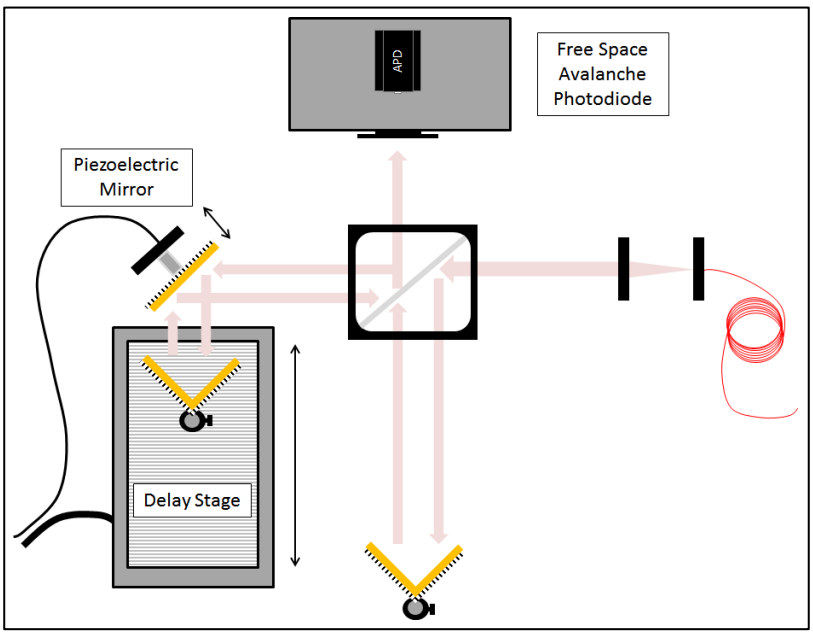

Figure 2-10 – Schematic of fibre optic coupled Michelson interferometer setup used. A 50:50 cubic beam splitter separates the beam into two balanced signals. One path has a fixed length and is reflected using gold retroreflectors back through the beam splitter, where 25% of the original signal is incident on the free space APD. The second path has a varied length using a delay stage to move an additional gold plated retroreflector. The phase of this second signal is perturbed using a piezo electric mirror with a total travel distance of 10 µm.

To determine the coherence time of a quantum dot, the visibility of the interference pattern is measured at a range of delay lengths to determine the decay constant, τ_2. In the experimental setup shown, a Newport UTS150CC delay stage is used to vary the time delay in one arm with respect to the other. The stage has a maximum travel distance of 15 cm corresponding to a total delay length of 1 ns, larger than typical quantum dot coherence times. A piezoelectric driven mirror, with a scan range of 10 µm, is positioned in the optical path of this delay arm which enables the interference visibility to be measured by recording the signal intensity on the APD as a function of the mirror displacement. As the interference visability is sensitive to the spatial alignment of the two optical beams, retro-reflectors are used to displace the beams, and return them along their original path. The use of retro-reflectors increases the stability of the interferometer compared to the use of conventional mirrors alone.

In order to quantify the quality of the optical alignment, a single mode laser with a coherence time significantly greater than that of quantum dots is used to test the setup. By measuring the coherence length of the laser, it is possible to determine systematic errors due to misalignment of the optical components. A plot of the measured interference visibility is shown in Figure 2-11, as well as that expected from a quantum dot with a coherence time of 200ps. A coherence time of more than 4 ns for the laser was calculated, which, for a quantum dot with a coherence length of 200 ps, would result in an error of 6 ps in the measured coherence time. This is error considered to be small with regards to other sources of error during likely measurements, such as fluctuating signal intensities.

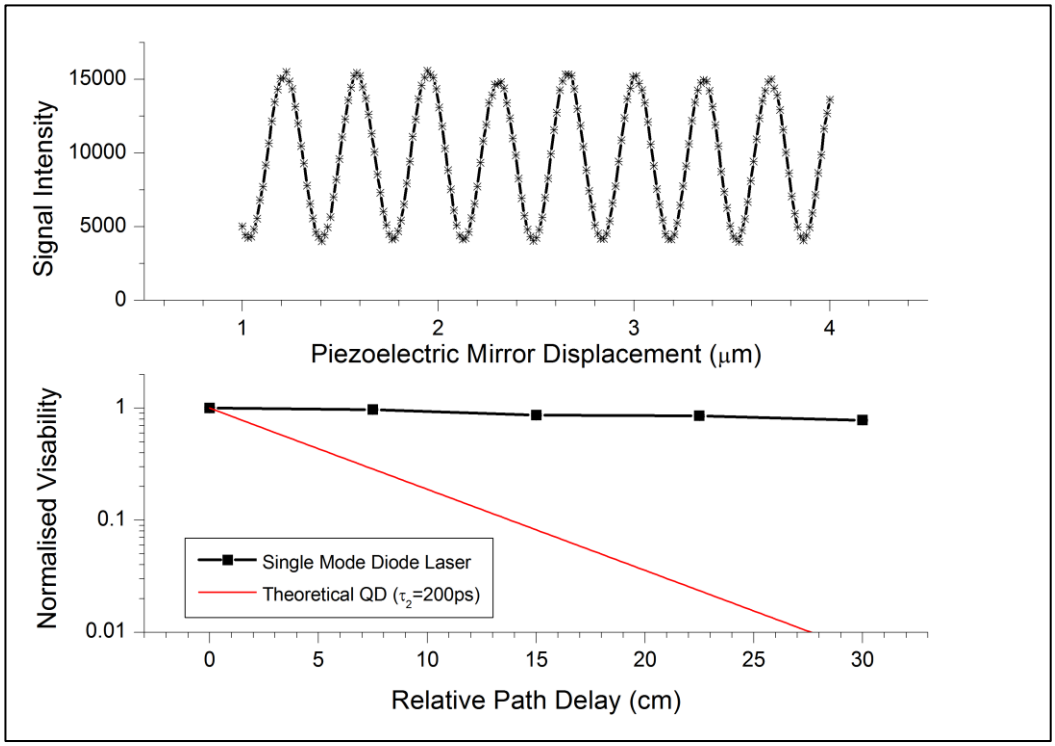

Figure 2-11 – (top) Interference pattern observed for a single mode laser at a given delay length using a Michelson Interferometer. The Visibility of the fringes is calculated to be > 10k counts s^{-1} with an offset of ~ 4.2k counts s^{-1}. This offset is the sum contribution from scattered photons, dark counts and imbalance between the two optical paths.

2.5.3. Lifetime

The interaction of quantum dots with their solid state environment can be both beneficial and detrimental. Fabrication of spatial and mode matched photonic structures leading to Purcell enhancements have been used to study interesting areas of physics such as the strong coupling regime [22]. Similarly though, the interaction of the quantum dot with its

environment may result in unwanted behaviour, such as blinking or spectral flickering due to affects such as charge trapping [23].

In order to determine the performance of a quantum dot embedded within a photonic structure, lifetime measurements can provide a quantitative method for doing so. In the absence of additional fields, the emission of a photon from a quantum dot is the result of spontaneous emission governed, and as such, the emission rate can be characterised by the lifetime, T_1. If however the quantum dot is located within a photonic structure which modifies the local density of states that the quantum dot can emit a photon into, the lifetime is modified according to Fermi's Golden Rule [24], see Equation 2-1

$$\frac{1}{T_1} = \Gamma_1 = \frac{2\pi}{\hbar^2}|\langle f|\bar{\mu}\bar{\varepsilon}|i\rangle|^2 \rho_{if}{}^2 \tag{2.1}$$

Equation 2-1 : Fermis Golden Rule for the rate of spontaneous emission (Γ) from the initial state, $|i\rangle$, to the final state, $\langle f|$. $\bar{\mu}$ represents the dipole moment of the quantum dot, $\bar{\varepsilon}$ is the vacuum field at the location of the quantum dot and ρ_{if} is the density of states.

To directly measure the lifetime of a quantum dot, a pulsed excitation source, fast photon detection and a timing circuit are needed. The pulsed excitation source used is a tuneable Ti:Si laser with a pulse duration of 100 fs. This results in a fourier limited linewidth of ~ 3 nm when tuned into resonance with the wetting layer, typically 870nm. As with most optical instruments used, the pulsed laser is coupled into a single mode fibre so that it can be readily used in the existing fibre launchers in either the bath or flow cryostat. Prior to coupling into the single mode fibre, a small portion of the excitation laser is siphoned off to trigger a photo diode. The purpose of this is to provide a reference signal which can be used to determine the relative time between excitation and the emission of photoluminescence.

An avalanche photodiode (APD) is used to record when a photon is emitted from the quantum dot. The choice over which APD to use depends strongly on the lifetime of the quantum dot to be measured. For APD's, a trade-off is required between the quantum efficiency and the readout time, and as such, it is possible to optimally detect photons or the timing of when a photon arrives, but not both. Two types of APD were available having instrument limited readout times of 90 ps and 400 ps with a quantum efficiency of approximately 3% and 25% respectively.

2.5.4. Hanbury-Brown Twiss

The Hanbury-Brown Twiss experiment is named after the two astronomers who pioneered the technique. At the time, Michelson interferometry was being extensively used at radio frequencies to determine the angular size of astronomical objects. Unfortunately, depending on the angular size of the object being measured, the size requirements of the detector caused problems as a result of the available technology. It was realised however by Hanbury-Brown and Twiss that if the radiation observed at two detectors was coherent, then the changes in the intensity of the two signals must be correlated [25]. The intensity correlation function, given by Equation 2-2, often referred to as the second order correlation function (*g^2)*, provides information on temporal distribution of photons.

$$g^{(2)}(\tau) = \frac{\langle I_1(t) I_2(t+\tau)\rangle}{\langle I_1(t)\rangle \langle I_2(t+\tau)\rangle} \tag{2.2}$$

Equation 2-2 – Second order (intensity) correlation function where τ is the relative time delay between the detection of the two signals, detected at time t.

In order to see why the second order correlation function is such a powerful technique in quantum optics, it is simplest to first consider its relationship with classical light sources. If we first consider the case where emission of light is entirely random for all values of τ, we see that $\langle I_1(t)\rangle = \langle I_2(t+\tau)\rangle$, and therefore $\langle I(t)^2\rangle = \langle I(t)\rangle^2$. The result is a measured $g^{(2)}(\tau)$ which equals one for all values of τ. Light of this type can be produced by systems such as lasers, where the probability of a photon being emitted is entirely uncorrelated with the probability of another photon being emitted.

In the event noise is introduced into the system, such as thermal fluctuations of a black body radiation, the intensity can be considered the sum of the unperturbed intensity plus a time dependent term. It must therefore follow that $\langle I'_1(t)^2\rangle \geq \langle I'_1(t)\rangle^2$, resulting in a $g^{(2)}(0) > 1$. Systems which exhibit second order correlation functions greater than one are considered to be classical light sources, with bunched photon distributions.

For a system such as a quantum dot, where it is only possible to emit a single photon at a time, the emission characteristics are exactly opposite of that for classical light sources. In the limit that τ = 0, we can see that $\langle I_2(t)^2\rangle = 0$ as the excited state has relaxed into the ground state, and therefore requires exciting again before it can emit a second photon. Therefore the second order correlation function must also be equal to zero. This test not

only provides insight into the anti-bunching of photon statistics, but is a result not allowed for classical light sources. As a result, measuring the second order correlation of photoluminescence provides a method to verify the quantum nature of the emission. A comparison of bunched, random and anti-bunched photon emission is presented schematically in Figure 2-12.

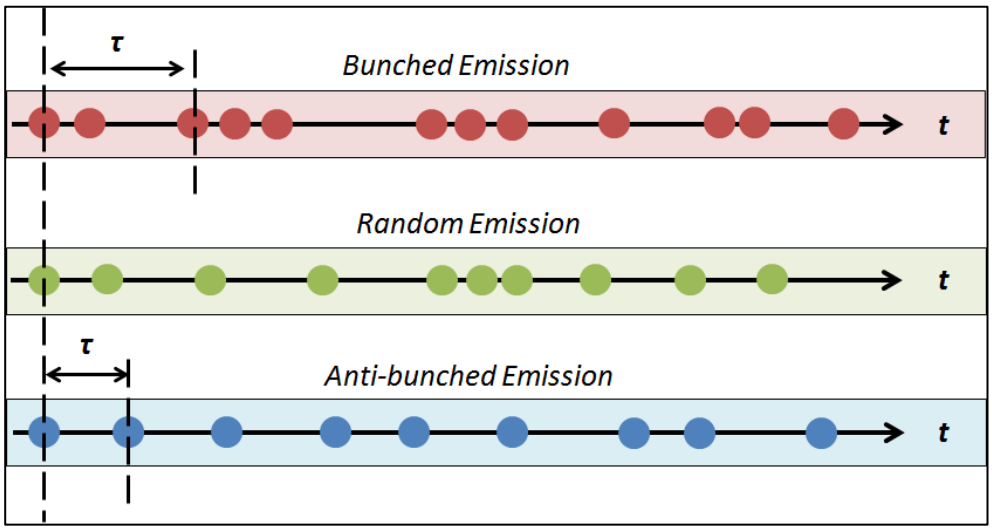

Figure 2-12 – Photon distributions as a function of time for bunched, random and antibunched emission.

In order to directly measure the photon statistics, a 50:50 cubic beam splitter is used to separate the collected photoluminescence into two optical paths. Free space APDs are then used to efficiently convert the detection of a photon into an electrical pulse. By fixing one of the APDs as the signal channel, and the second as the trigger, a single photon counting module can precisely measures time delays between the two detections. A schematic of the experimental setup used is shown in Figure 2-13.

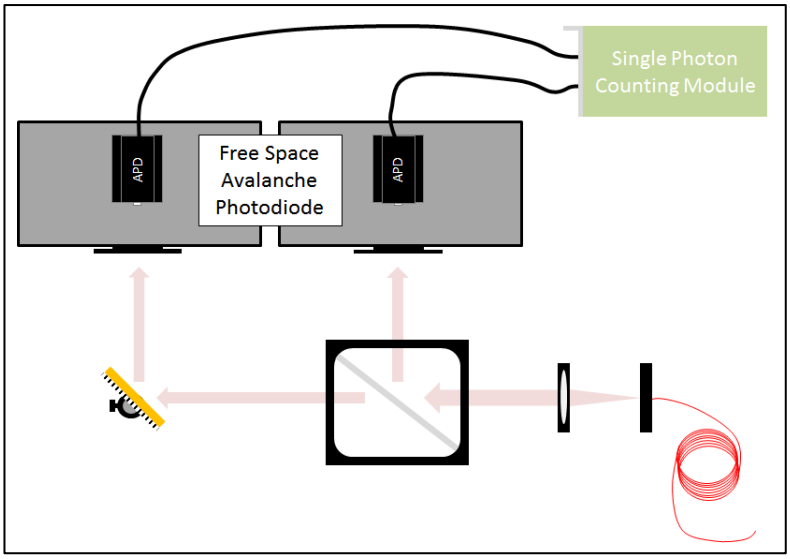

Figure 2-13 – Setup of fibre coupled Hanbury -Brown Twiss experiment using 50:50 cubic beam splitter with two free space APD's. Detection pulses from the APD's are relayed into a timing circuit in the single photon counting module.

2.6. Solid Immersion Lens

The nature of nanotechnology often means that the resolution required to adequately study a device is close to, or even beyond the diffraction limit for optical microscopes. This is apparent when studying photoluminescence in single mode photonic structures, where key features may be difficult to distinguish. By examining Rayleigh's resolution criteria, Equation 2-3, it can be seen that the resolution of a system can be increased in three ways [19].

$$\boldsymbol{\delta = \frac{1.22\lambda_0}{2n_{obj}\sin(\alpha)}} \tag{2.3}$$

Equation 2-3 : Rayleigh resolution criteria, where the measured wavelength is given by $\boldsymbol{\lambda_0}$, the refractive index of the collection path is $\boldsymbol{n_{obj}}$, and the half angle for the cone of light which is collected by the objective lens is given by $\boldsymbol{\alpha}$.

Unfortunately, the simplest approach of reducing the observation wavelength, λ_0, is impractical and/or impossible for photoluminescence as the emission energy of quantum dots is confined to a small wavelength range. We must therefore consider the two alternative options available; increase the refractive index, $\mathbf{n_{obj}}$, or increase the accepted angle of light collected by the objective lens, $\boldsymbol{\alpha}$.

At room temperatures, techniques such as oil immersion microscopy are extensively used to increase the resolving power of an optical setup by increasing the refractive index of the area surrounding the object. In order to prevent reflections defined by Snell's Law, the refractive index of the oil must match that of the objective lens, limiting the materials available. Further, more practical limitations apply when attempting to implement such a system at cryogenic temperatures.

An alternative to oil immersion microscopy is a solid immersion lens microscope, first proposed to be used with a conventional microscope in 1990 as a method for improving the spatial resolution without the use of liquids [20]. It was proposed to place a hemispherical lens in contact with the surface of the sample, as shown in Figure 2-14, which would enable the surface to be imaged at the centre of the hemisphere. It can be seen from a simple geometric argument, that when the focal point of the objective lens is set to the centre of the hemisphere, each ray is normally incident to the surface of the solid immersion lens. As a result, no refraction occurs and the Abbe Sine condition, which requires the ratio of the sine of the incident angle and refracted angle to be a constant in order to produce clear images, is met [19].

Interestingly, and somewhat less intuitively, a second focal point exits at a depth of R/n below the centre of the hemisphere, where R is the radius of the lens, and n is the refractive index. Due to the spherical curvature of the lens, the ratio of the sine of the incident and refracted light rays make with the normal to the lens's surface is always constant. This also represents a solution to the Abbe Sine condition, and so produces a distortion free image [19].

As a result of these two focal points, there are two common types of solid immersion lens. The hemispherical solid immersion lens (h-SIL) utilises the focal point at the centre of the sphere as shown in Figure 2-14 – a. The second type takes the shape of a flat bottomed sphere, sometimes referred to as a Weierstrass solid immersion lens, or more commonly a super spherical solid immersion lens (s-SIL), which is designed to focus at the second aplanatic point, shown in Figure 2-14 – b.

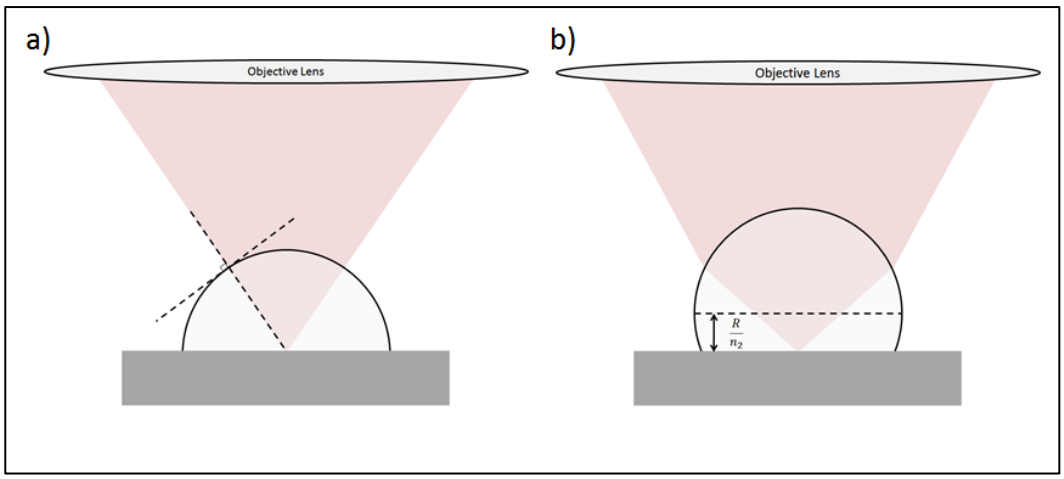

Figure 2-14 – (a) Ray diagram showing the focal position for a hemispherical solid immersion lens at the centre of a sphere. As such, each focused ray is normally incident to the surface of the sphere. (b) Ray diagram showing the second focal position of spherical sphere a depth of R/n_2 below the equator.

Work presented here makes use of a cubic zirconia s-SIL as it can be used to achieve higher resolutions than that of the h-SIL. The reason that an s-SIL improves the resolution more so than a h-SIL is that the effective numerical aperture, and therefore the resolution, is increased by a factor of $\mathbf{n}^2$ for the s-SIL, whereas the h-SIL only provides an improvement proportional to **n** [21].

For both SIL types, a fundamental limit exists on the maximum collection efficiency increase which can be gained. This limit occurs when the light cone collected by the objective lens is a full hemisphere resulting in a numerical aperture equal to the refractive index of the SIL. When it is not possible to use a numerical aperture matched objective lens to couple with the SIL, the s-SIL is advantageous for collection efficiency due to the refraction which occurs at the SILs surface, resulting in tighter confinement of the light cone when it exits the SIL.

It must be stated that despite the strong advantages of SIL's, there are several practical limitations on their use. Firstly, while the existence of two aplanatic points can be shown for a spherical lens, the size of the distortion free imaging plane which exists is typically very small. This concern is discussed in more detail in §3 where imaging distortions are of significant concern.

Additionally, chromatic aberrations, whilst not of a major concern for h-SIL's, may be more evident for s-SIL's depending on the material used. The reason for this is that both the size of the SIL, as well as the vertical position of the imaging plane, is related to the

refractive index, a wavelength dependent term. For the zirconium dioxide s-SILs used in this thesis, the strength of these chromatic aberrations are not thought to be significant over the small wavelength ranges considered based on the small relative changes in the refractive index of zirconium dioxide[2].

The final major challenge when using SIL's at cryogenic temperatures is maintaining alignment of the SIL in the correct location relative the samples surface. Both the effects of vacuum pumping and thermal contraction must be countered if control is to be had over where the sample can be imaged. Two methods have therefore been found acceptable for securing the position of the SIL to the surface; high viscous bonding or mechanical connection.

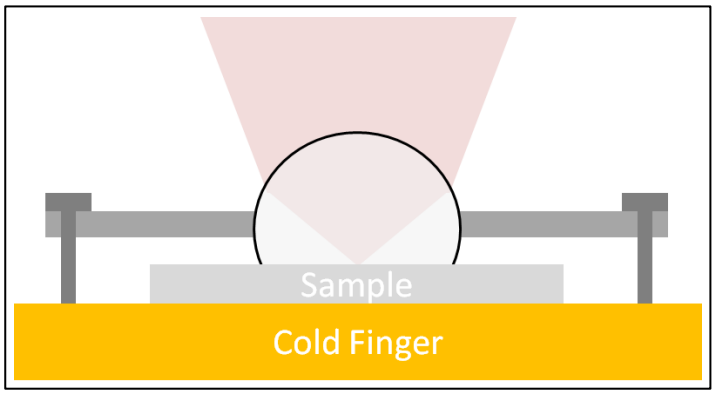

Figure 2-15 – Schematic showing method used to mechanically attach the solid immersion lens to the surface of the sample securely. A thin, flexible, membrane with a 1 mm hole is placed over the solid immersion lens to hold it in place. The membrane is then fixed to the cryostat, tightening until good contact occurs between the SIL and the sample wafer.

In high viscous bonding, carbon based grease is used to mechanically connect the sample and the outer surface of the SIL. It is found to provide adequate stability during vacuum pumping and freezes in place at cryogenic temperatures. Furthermore the carbon based grease is readily soluble in n-Butyle-acetate, Acetone and Xylene, and may be removed without permanent contamination of the sample.

Where additional photonic structures exist on the samples surface, viscous bonding may however result in the collapse or partial destruction of free standing membranes. A method of mechanically bonding the SIL to the surface of the sample is therefore used,

[2] A relative change of less than 1% exists between the refractive index of ZrO^2 between the wavelength range of 920nm and 633nm [26].

as depicted in Figure 2-15, using a thin 1 mm Ø pinhole membrane. This method is used over high viscous bonding only when photonic structures are present as the mechanical holder introduces constraints on the sample size as well as obscuring parts of the sample.

2.7. References

[1] E. C. Larkins and J. S. Harris, *Molecular Beam Epitaxy of High- Quality GaAs and AIGaAs*. Elsevier, 1995.

[2] A. Baskaran and P. Smereka, "Mechanisms of Stranski-Krastanov growth," *J. Appl. Phys.*, vol. 111, no. 4, pp. 1–6, 2012.

[3] A Y. Cho and J. R. Arthur, "Molecular beam epitaxy," *Prog. Solid State Chem.*, vol. 10, pp. 157–191, 1975.

[4] J. J. Harris and B. A. Joyce, "Oscillations In The Surface Structure Of Sn Doped GaAs During Growth By MBE," *Surf. Sci. Lett.*, vol. 103, no. 1, pp. 90–96, 1981.

[5] M. Gabas, S. Palanco, S. Bijani, E. Barrigon, C. Algora, I. Rey-Stolle, I. Garcia, J. R. R. Ramos-Barrado, M. Gabás, E. Barrigón, and I. García, "Analysis of the surface state of epi-ready Ge wafers," *Appl. Surf. Sci.*, vol. 258, no. 20, pp. 8166–8170, 2012.

[6] R. A. Kubiak and S. M. Newstead, "The Technology and Design of Molecular Beam Epitaxy Systems."

[7] D. G. Schlom and J. S. Harris, "MBE Growth of High TC Superconductors," 1986.

[8] N. Kaiser, "Review of the fundamentals of thin-film growth.," *Appl. Opt.*, vol. 41, no. 16, pp. 3053–3060, 2002.

[9] K. Oura, M. Katayama, A. V. Zotov, V. G. Lifshits, and A. A. Saranin, *Surface Science - Growth of Thin Films*. Berlin, Heidelberg: Springer Berlin Heidelberg, 2003.

[10] J. H. Blokland, M. Bozkurt, J. M. Ulloa, D. Reuter, A. D. Wieck, P. M. Koenraad, P. C. M. Christianen, and J. C. Maan, "Ellipsoidal InAs quantum dots observed by cross-sectional scanning tunneling microscopy," *Appl. Phys. Lett.*, vol. 94, no. 2, p. 23107, 2009.

[11] D. Sreenivasan, T. U. Eindhoven, and R. Magnificus, “Capture, relaxation and recombination in quantum dots,” 2008.

[12] R. J. Coles, “Quantum Optical Circuits using III-V Nanophotonic Structures,” no. April, 2015.

[13] N. Sahu, B. Parija, and S. Panigrahi, “Fundamental understanding and modeling of spin coating process: A review,” *Indian J. Phys.*, vol. 83, no. 4, pp. 493–502, 2009.

[14] N. Olds and E. Engineering, “Characterization and Optimization of ZEP520A Electron Beam Lithography Resist Abstract : Introduction : Procedure,” pp. 96–97, 2004.

[15] S. Combrié, S. Bansropun, M. Lecomte, O. Parillaud, S. Cassette, H. Benisty, and J. Nagle, “Optimization of an inductively coupled plasma etching process of GaInP⁄GaAs based material for photonic band gap applications,” *J. Vac. Sci. Technol. B Microelectron. Nanom. Struct.*, vol. 23, no. 4, p. 1521, 2005.

[16] K. Kinoshita, H. Utsumi, K. Suemitsu, H. Hada, and T. Sugibayashi, “Etching magnetic tunnel junction with metal etchers,” *Jpn. J. Appl. Phys.*, vol. 49, no. 8 PART 2, 2010.

[17] M. B. Stern and P. F. Liao, “Reactive ion etching of GaAs and InP using SiCl4,” vol. 1053, no. 1983, pp. 18–21, 2016.

[18] H. P. Burstyn, “Critical point drying: Application of the physics of the PVT surface to electron microscopy,” *Am. J. Phys.*, vol. 43, no. 5, p. 414, 1975.

[19] L. P. Ghislain and V. B. Elings, “Imaging with solid immersion lenses, spatial resolution, and applications,” *Proc. IEEE*, vol. 88, no. 9, pp. 1491–1498, Sep. 2000.

[20] S. M. Mansfield and G. S. Kino, “Solid immersion microscope,” vol. 2615, no. 1990, pp. 166–168, 2016.

[21] D. Xiangmei, G. Tao, and Z. Songlin, “Focus shaping of Weierstrass solid immersion lens by an axisymmetric Bessel-modulated Gaussian beam,” *Opt.*

Appl., vol. XLIII, no. 2, 2013.

[22] J. P. Reithmaier, G. Sek, A. Löffler, C. Hofmann, S. Kuhn, S. Reitzenstein, L. V Keldysh, V. D. Kulakovskii, T. L. Reinecke, and A. Forchel, "Strong coupling in a single quantum dot-semiconductor microcavity system.," *Nature*, vol. 432, no. 7014, pp. 197–200, Nov. 2004.

[23] C. Santori, D. Fattal, J. Vučković, G. S. Solomon, E. Waks, and Y. Yamamoto, "Submicrosecond correlations in photoluminescence from InAs quantum dots," *Phys. Rev. B*, vol. 69, no. 20, pp. 1–8, May 2004.

[24] A. C. T. Thijssen, M. J. Cryan, J. G. Rarity, and R. Oulton, "Transfer of arbitrary quantum emitter states to near-field photon superpositions in nanocavities.," *Opt. Express*, vol. 20, no. 20, pp. 22412–28, Sep. 2012.

[25] G. Baym, "The physics of hanbury brown-twiss intensity interferometry: From stars to nuclear collisions," *Acta Phys. Pol. B*, vol. 29, no. 7, pp. 1839–1884, 1998.

[26] I. H. Malitson, "Interspecimen Comparison of the Refractive Index of Fused Silica*,†," *J. Opt. Soc. Am.*, vol. 55, no. 10, p. 1205, Oct. 1965.

3. Dot Registration

3.1. Introduction

A key benefit of Quantum Dots (QD's) over alternative platforms for quantum information processing *(QIP)*, such as trapped ions, is that they are intrinsically scalable and may interact strongly with the solid state environment [1]. However, if optimal light-matter coupling is to be achieved, both the spectral and spatial properties of the QD must be matched to the photonic structure, and vice versa. Due to the random nature of self-assembled growth (see Chapter 2), the ability to precisely know the position of a QD, and to deterministically embed it within photonic structure has therefore been an active area of research for more than a decade [2].

Over time, several fundamentally different approaches to embedding QD's with spatial control in photonic structures have been developed, but to date, no path on how to achieve optimal results has proven to be dominant [3]. Whilst each method attempts to address at least one technological barrier, it is this author's opinion that the most promising technique is that of nucleated or site controlled growth. As this technique still has many disadvantages, an interim technique is proposed in this chapter of registering the relative positions of quantum dots with respect to pre-fabricated markers. This then allows for the deterministic fabrication of photonic structures around the quantum dot using conventional lithographic processes.

3.1.1. Chapter Overview

As an introduction to the work presented in this chapter, we first discuss what levels of accuracy will be required in general of any technique which aims to locate a quantum dot and fabricate a photonic structure around it in section 3.1.2. A brief discussion of alternative techniques to dot registration is then presented in order to provide a basis for understanding the current motivation for using dot registration in sections 3.1.3 and 3.1.4. A discussion of the bespoke samples required for the registration process is given in section 3.2, along with details regarding experimental setup. In section 3.3, experimental results of the dot registration process are presented, including a detailed discussion regarding the effects a solid immersion lens has on the registration process. A summary of the key results is presented in section 3.4.

3.1.2. Precision

For any technique which aims to embed a quantum dot within a photonic nanostructure, the level of precision required will ultimately depend on the photonic structure being fabricated and the proposed applications. It is therefore not possible to definitively state one precision required for all purposes. Based on many nanophotonic structures discussed in the literature, there is a clear divide between devices which are strongly spatially sensitive and those which are insensitive to the relative position of an embedded quantum dot.

The nanobeam waveguide used extensively in this thesis can be particularly sensitive to the position of an embed quantum dot. This is discussed in more detail in chapter 4, where it is shown that in order to realise meaningful control on the emitted photons, a quantum dot must be precisely located with an accuracy of approximately 30 nm. As a similar example of a photonic structure with strong spatial dependence, the L3 photonic crystal cavity [4], is discussed here. In order to facilitate this discussion, the fundamental mode of the L3 photonic crystal cavity, optimised for 950 nm, is provided by R. Coles and presented in Figure 3-1 with the author's permission.

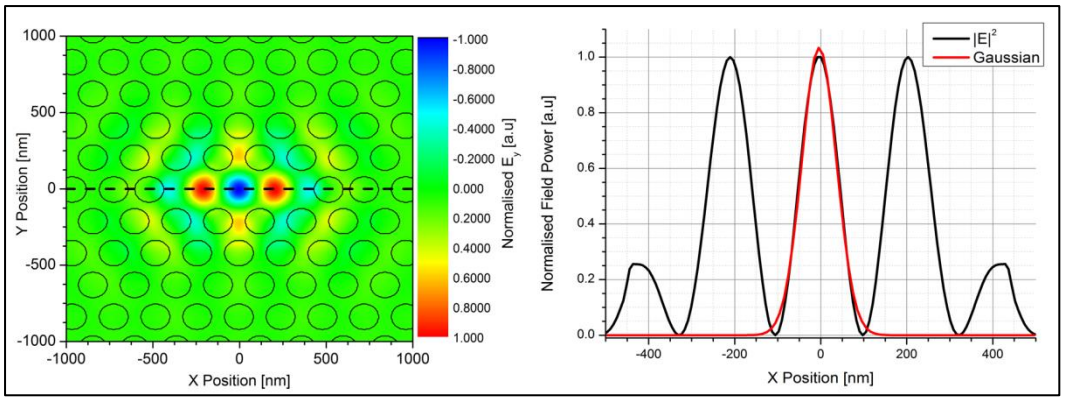

Figure 3-1: (left) Field profile for the fundamental transverse electric field profile, TE_y, for a photonic crystal L3 defect cavity (Simulation performed by R.Coles, image is included with permission). (right) Slice through fundamental electric field modes showing spatial dependence.

A cross section of the electric field profile is taken along the dotted line shown above, and is used to calculate the power of the electric field as a function of position from the centre of the photonic cavity. For most applications, it is preferable for the quantum dot to couple to the central anti-node as it reduces the proximity of the quantum dot to surfaces and reduces the overlap of the quantum dot with higher order modes. For the fundamental anti-node at the centre of the photonic crystal cavity, the field is shown to exhibit a Gaussian profile, with a full width at the half maximum (*FWHM*) of 95 nm. Due

to the exponential decay of a Gaussian profile, the power in the electric field decays quickly away from the antinodes, resulting in a small region where a quantum dot may efficiently couple to the cavity mode.

A benchmark of photonic cavities is the demonstration of strong coupling and large Purcell factors due to their importance in QIP. In the dipole approximation, the total Purcell factor for a quantum dot within a cavity is given by Equation 3-1 [5]. As we are only concerned with the spatial dependence of an embedded quantum dot, the second half of the equation can be neglected as this refers to the overlap between the emission wavelength and the resonant cavity wavelength. The first term however relates the overlap of the power in the electric field mode to that of the dipole moment of the emitter. As observed for the photonic crystal cavity above, the electric field of the central anti-node is seen to decay exponentially, and as a result, if a quantum dot was displaced as little as 45 nm in the x-axis, the increase in the spontaneous emission rate would be halved.

$$\frac{\boldsymbol{\Gamma}}{\boldsymbol{\Gamma_0}} = \boldsymbol{F_{cav}}\left(\frac{\vec{\boldsymbol{E}}(\vec{\boldsymbol{r}})\cdot\vec{\boldsymbol{\mu}}}{|\vec{\boldsymbol{E}}_{\boldsymbol{max}}||\vec{\boldsymbol{\mu}}|}\right)^{\mathbf{2}} \times \frac{\mathbf{1}}{\mathbf{1}+\mathbf{4}\boldsymbol{Q}^{\mathbf{2}}\left(\frac{\boldsymbol{\lambda_{emiter}}}{\boldsymbol{\lambda_{cav}}}-\mathbf{1}\right)^{\mathbf{2}}} + \boldsymbol{F_{pc}} \tag{3.1}$$

Equation 3-1 – Ratio of the spontaneous emission rate ($\boldsymbol{\Gamma}$) of an emitter, embedded within a cavity, with respect to the intrinsic emission rate ($\boldsymbol{\Gamma_0}$) in the bulk semiconductor. $\boldsymbol{F_{cav}}$ and $\boldsymbol{F_{pc}}$ correspond to the Purcell factors due to the cavity mode and photonic crystal respectively.

It is clear therefore that in order to achieve optimal light matter coupling, it is desirable to control the relative position between the quantum dot and photonic nanostructure a scale comparable to, but ideally much smaller than, the size of the optical field of the device. Control over the position of the photonic structure is readily achieved using standard lithographic processes, however as the size of the quantum dots is far below the diffraction limit of optical light, determining where to fabricate the photonic structurer has proved to be a significant technological challenge. Before discussing the technique of dot registration, two of the most common techniques used to control the location of quantum dots are presented.

3.1.3. Nanowires

The fabrication of quantum dot nanowire structures is an active area of research, where growth occurs typically via MBE or MOCVD (Metal-Organic Chemical Vapour Deposition)[6]. Nanowires, as their name suggests, are pillars of semiconductor material with typical diameters in the order of a few hundred nanometres, growing to be several micrometres in length [7]. Unfortunately, to achieve significantly longer nanowire lengths, the width of the nanowire also increases. Within the field of nanowires, there exist an extensive range of growth techniques and conditions, a testament to the versatility of nanowires, as well as the sensitivity and levels of control required. We limit the discussion here to the bottom up growth method, where nanowires are grown at nucleation sites, as the surface quality of the nanowire is typically superior.

Traditionally, nanowires are grown at a metal defect site on the surface of the epi-ready wafer [8]. This metal defect provides a nucleation site for growth to occur, acting as a catalyst for the vapour-liquid-solid phase transition. Site controlled growth of the nanowire structures can therefore be achieved through conventional lithographic techniques to control the location of the metal defects [9]. More recently, catalyst free techniques are emerging as it is believed that the metal defects interfere with the opto-electric properties of the nanowires [10][11]. One such method explored for catalyst free growth is achieved by introducing hole defects into a hard mask which is removed post growth [12]. However, due to the extreme lengths which are taken in order to produce epitaxial ready surfaces of the initial wafers, subsequent wafer processing techniques required to fabricate the hard mask undoubtedly introduce contaminants.

In order to utilise nanowire quantum dots for QIP, they must exhibit scalability. An interesting method of achieving scalability in nanowires, is that of overgrowth once the nanowire has formed. It is through such techniques that so called nanowire trees can be fabricated, where branches of nanowires can be grown radially from the primary nanowire [13]. Alternatively, through nano-positioning of cleaved nanowires it is possible to manipulate individual nanowires into fabricated photonic circuits [14].

Whilst it would seem that nanowires exhibit all the desirable properties required to achieve a scalable photonic circuit, there remain several important challenges. Significant among these is the quality of the photoluminescence from nanowire quantum dots. Until recently, coherence times significantly less than those measured for self-assembled quantum dots were accepted as normal. Improvements in fabrication quality have led to

coherence times of several hundred picoseconds at liquid helium temperatures being reported [15], although coherence times in the order of ~10's picoseconds are still typical [16]. In comparison, under resonant excitation, Heitler regime coherence times have been observed in excess of 20 ns for self-assembled quantum dots [17]. Furthermore, due to the large lateral size of the nanowire quantum dot, strong interactions are present with the nanowire surface. This can result in an array of unwanted characteristics in the photoluminescence, such as blinking, flickering and spectral wondering. Significant work has therefore been conducted investigating radial overgrowth and surface passivation to reduce the proximity of unsatisfied bonds [18][10].

3.1.4. Deterministic Growth

As self-assembled growth has thus far yielded quantum dots with superior optical properties, nucleated growth attempts to control the locations where self-assembly occurs. In many regards, nucleated growth is similar to the catalyst free bottom up growth approach used to fabricate nanowires. Whilst it is the epi-ready wafer which is perturbed, opposed to a hard mask used for nanowires, lithographic processes remain very similar.

A standard approach for nucleated growth is to introduce small (typically 10 – 100 nm's in diameter) etched holes in the [001] or [111] GaAs substrate [19]. However moderate levels of success has also been achieved by varying the depth of the etched hole slowly with respect to the lateral size, using pyramidal shaped etched holes at micron scales [20]. With a nucleation site introduced, MBE or MOCVD is resumed where GaAs and InAs are deposited sequentially at varying thicknesses. Whilst the levels of precision achieved by this technique are exceptional, it possesses many of the same problems present for nanowire quantum dots.

To date, the smallest achieved linewidth reported via nucleated growth of InGaAs quantum dots is 25 μeV (13.2 ps) [21], however these linewidths represent a small minority, with typical values in excess of 100 μeV [19][20][21][22]. While concerns such as spectral wandering are less prominent than they are in nanowires, additional problems are encountered due to strain and growth rate anisotropy. As a result, care must be taken to ensure only a single quantum dot forms at each nucleation site.

3.1.5. Dot Registration

It is clear when considering alternatives to the random growth undergone by self-assembled quantum dots, that the intervening wafer processes steps dramatically affects the optical properties of the dots produced. Even with extensive measures taken during MBE to remove contaminants from the growth chamber, the introduction of hard masks or etched surfaces results in a roughened surface and therefore interface fluctuations. Many groups for this reason use high densities of self-assembled quantum dots, fabricating numerous photonic structures, and search for a quantum dot randomly positioned in a suitable location. An interim solution, which aids progress on integrated photonic circuits using multiple quantum dots, whilst technical challenges are overcome with deterministic growth, is therefore desirable.

The proposed solution adopted here, similar to that used by Thon et al [2] and Senellart et al [23], is that of dot registration, where a suitable self-assembled quantum dot is identified, its position registered, and a photonic structure is precisely fabricated around it. Besides providing a platform to achieve optimally spatial located quantum dots in photonic structures, two additional benefits may be realised by characterising the photoluminescence prior to fabrication in this manner.

Firstly, by characterising the optical properties of a quantum dot before fabrication, fine control over critical dimensions of the photonic structures can be tailored. This is of significant importance when considering structures such as cavities or interferometers with a high finesse. Current efforts to tune quantum dots into resonance with photonic modes have relied on pre-fabrication of diode structures [24], or more permanent changes involving a systematic post etching to fine tune critical dimensions [25]. Furthermore, if two or more suitably coherent quantum dots can be identified, then a scalable photonic structure may be used to provide interconnectivity.

Secondly, dot registration is by its very nature a technique which identifies how the fabrication of a photonic structure affects the properties of the quantum dot. As is commonly reported in nanowires, where the quantum dot is susceptible to charge fluctuations at the surface, it will be directly evident if similar phenomenon occurs after fabrication through a comparison of the optical properties. Additionally, direct measurements of normally convoluted performance indicators, such as Purcell factors, are readily calculated and do not require assumptions regarding ensemble averages. It would therefore seem that not only can dot registration provide optimal spatial and

mode matched photonic structures, but can readily quantify the performance, aiding future developments.

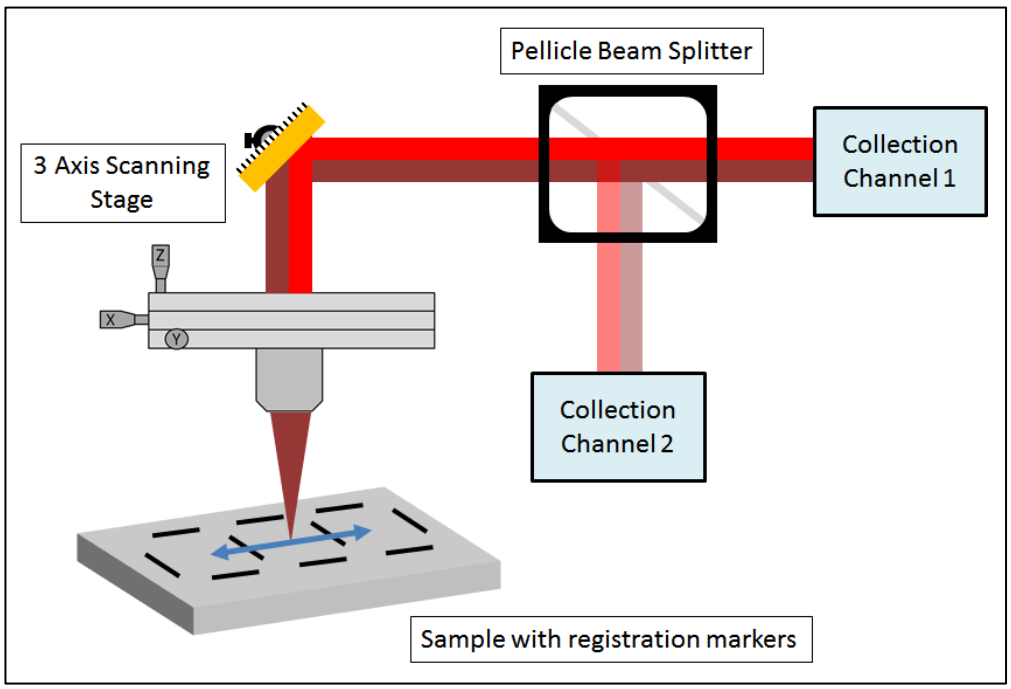

Figure 3-2 – Schematic showing two channel collection scheme used for dot registration. Photoluminescence and reflected laser signal is collected through the same objective lens before being split into two unequal arms using a 92:8 (Transmission : Reflection) pellicle beam splitter.

In this work, dot registration is developed using the continuous flow cryostat described in detail in Chapter 2. A single excitation channel, using either a HeNe (633 nm) or Diode (808 nm) laser, is used to excite quantum dots. Photoluminescence and the reflected laser signal are collected through the same objective lens before being split into two channels via a 92:8 (Transmission : Reflection) pellicle beam splitter, as shown in Figure 3-2. The transmitted channel is filtered using either a band pass filter or a monochromator to isolate a single quantum dot transition before being measured using an avalanche photo diode (APD). Additional attenuation is required for the channel used to collect the reflected signal, done using neutral density filters, due to the relatively high intensity of the reflected laser signal. No spectral filtering is employed for this channel as any spectral contributions are several orders of magnitude weaker than the laser signal.

In order to register the position of a suitable quantum dot, a closed loop piezo electric stage is used to scan the objective lens across the sample. The orthogonal sets of registration markers shown by black lines on the samples surface in Figure 3-2 are aligned perpendicular to the scanning stage axis to independently determine the horizontal and

vertical relative displacement of the quantum dot. The collected data from the two optical collection paths, with an example shown in Figure 3-3, is analysed using a least squared fit method to locate the central peaks of the markers and the quantum dot. By repeating the scan numerous times, a statistical average of the quantum dots relative location can be determined. With this information, standard lithographic processes can be used to fabricate the desired photonic structure around the quantum dot.

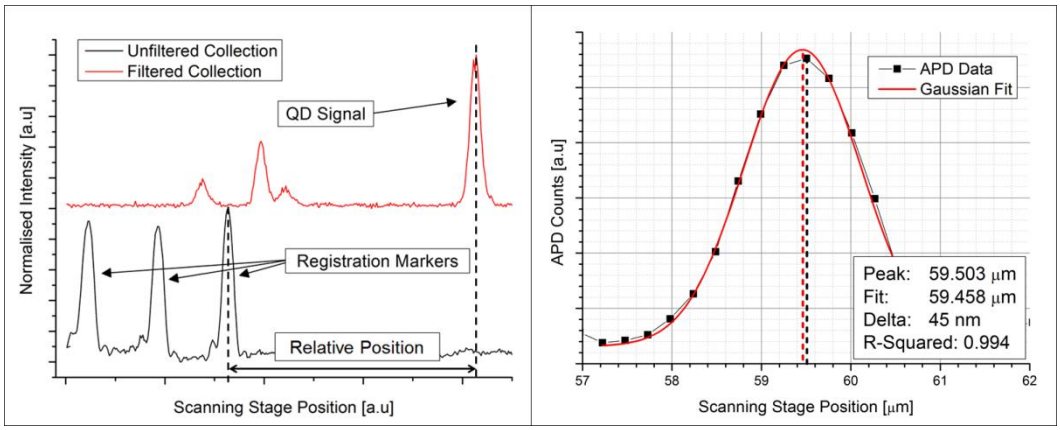

Figure 3-3 – Example of collected signal through the filtered and un-filtered collection channels of the photoluminescence setup as a function of the scanning stage position. (Left) Three distinct peaks are observed (black) where the laser is scanned over three registration markers. Similarly, a single well isolated bright peak (red) is visible at some distance away from the markers in the spectrally filtered channel. (Right) Least squared fit of a Gaussian (red) is fitted to the raw APD data for a QD signal (black) to determine its absolute positions.

So far, the technique of dot registration has already enjoyed moderate success in other groups, notably being used to realise strong coupling of a quantum dot in a L3 photonic crystal cavity [2]. However, advances in the technique appear to have stagnated with multiple groups reporting similar distribution widths (FWHM) of 50 nm in the relative position of the quantum dot with respect to the pre-fabricated registration markers [2][26]. Based on the work presented in this chapter, it is believed that this limit is the result of the limited optical resolution of a conventional micro photoluminescence setup. We therefore show using a solid immersion lens that aberration free dot registration is possible and results in a reduced distribution width for the relative position of the quantum dot.

3.2. Samples

The samples used for dot registration are of the standard 140 nm thick GaAs membrane heterostructure described in detail in chapter 2. As dot registration requires the identification of individual quantum dot lines which are both spatially and spectrally resolvable with respect to neighbouring quantum dots, samples are taken from portions of the wafer with low quantum dot density.

3.2.1. Marker Design

In order to support a solid immersion lens, as well as enable scalable fabrication, a compact design for the registration markers is required that still enables photonic structures to be interconnected. Two distinct designs were considered, each with their own specific advantages, which are shown in Figure 3-4.

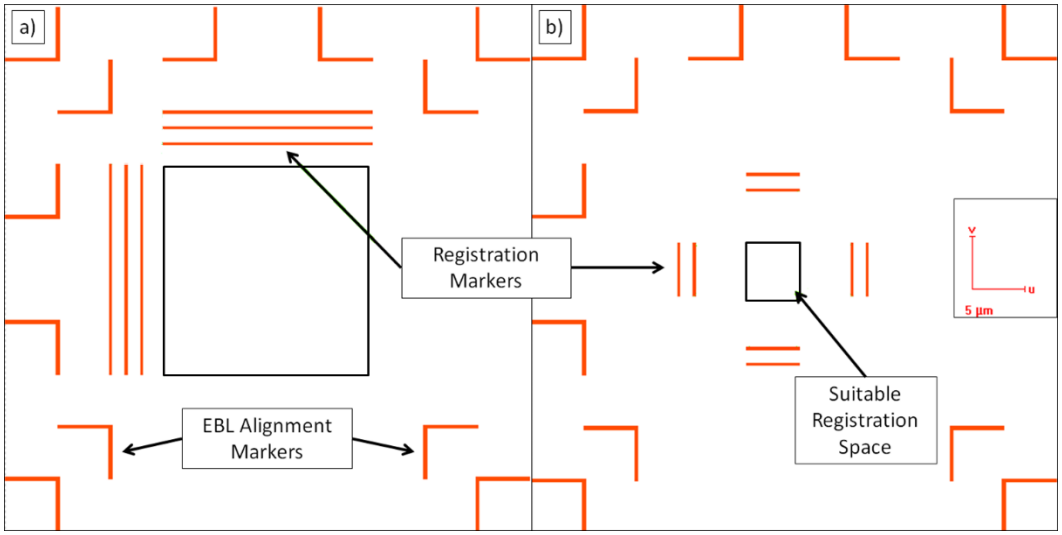

Figure 3-4 – Registration marker designs to enable the fabrication of scalable photonic circuits as well as calibration of the magnification due to a solid immersion lens. Pattern of the proposed markers is shown in red, with the supported registration area shown in green. (left) An open marker design which enables fabrication of larger photonic devices. (right) Compressed registration grid with open marker design to accommodate interconnectivity between devices.

The open marker design shown in Figure 3-4a was originally designed to allow for large scale photonic structures to be fabricated, as multiple quantum dots can be registered with a single marker set. The use of a solid immersion lens however requires at least two markers be scanned to calibrate the effective magnification due to the SIL as it is highly sensitive to the focal position of the objective lens. This therefore represents a problem for this design as in order to provide a large area to find suitable quantum dots, the markers are closely spaced, positioned only 1.5 µm apart. As a result of the small spacing,

the fractional error in their positions relative to the separation is large, making the magnification value determined less reliable.

When it was considered that photonic waveguides could be used over relatively large distances with the use of critical point drying [27], the marker set in Figure 3-4b was developed in order to decrease the percentage error in the calculated magnification. Photonic waveguides can then be used to navigate between the registration markers into areas of the wafer intentionally left free for the fabrication of photonic components.

3.2.2. Marker Fabrication

In order to support dot registration, it is necessary to fabricate registration markers on the surface of the sample first. Standard EBL techniques were used to transfer a selection of the 200nm wide registration patterns shown in Figure 3-4 into the electron beam resist. Metal evaporation is used to transfer a 5 nm thick layer of titanium, followed by a 20 nm thick layer of gold, which binds to the surface of the sample where the developed electron beam resist has been removed. Metal evaporation rates between 0.2 nm min^{-1} and 0.8 nm min^{-1} are used to allow the evaporated metal time to cool and prevent smearing. After the desired film thickness is reached, measured using a piezoelectric transducer, the remaining electron beam resist is removed, along with any excess metal, using n-methyl-2-pyrolidinone. It was found however that whilst the gold provided a good medium to reflect the laser signal, it was not robust enough to withstand sequential wafer processing techniques. Scanning electron microscope (SEM) images are shown in Figure 3-5 of a set of gold registration markers. Figure 3-5 a shows the gold markers after evaporation, before the sample has been used for dot registration purposes. Figure 3-5b shows the same wafer after the sample has been used for dot registration and subsequent gold markers have been evaporated onto the surface.

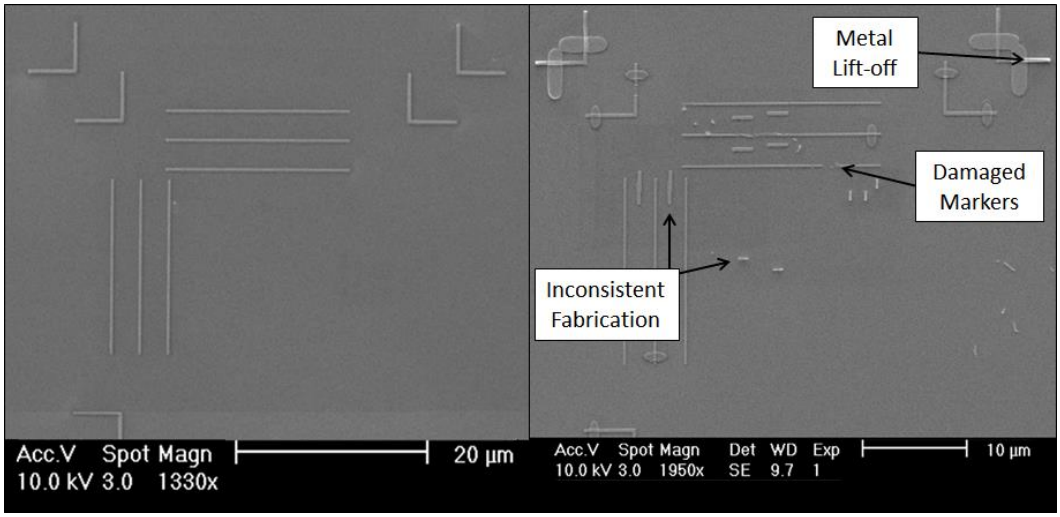

Figure 3-5 – (left) SEM image of gold registration markers immediately after fabrication. (right) SEM of registration markers which have been used for dot registration with supplementary gold markers fabricated afterwards. Signatures of metal lift-off are prevalent in both the original and supplementary markers after subsequent wafer processing steps (right)

Several issues are identified with the use of gold markers as a result of the damage revealed between SEM images. Firstly, the existing gold markers are readily damaged when standard wafer processing techniques are used. Further damage can be seen in the '*L*' shaped automatic write field alignment markers in the corners of the image. This is evident from the distinctive shadow which appears, characteristic of when the metal begins to lift away from the samples surface. As a result, the alignment of subsequent EBL exposures will be subject to additional sources of error. Additionally, as highlighted on the SEM image, the fabrication of the additional markers shows mixed results as some of the markers have been removed during the process to remove the excess titanium and gold which covers the entire surface after evaporation. As a result, an alternative etched marker is preferentially used in later registration runs, which rather than increasing the reflected laser signal, acts to scatter it away, reducing the total signal intensity.

3.2.3. Marker Alignment

A non-trivial complication which arises from the use of a solid immersion lens is that of orthogonality between the sample, registration markers and the scanning stage. If a sample is examined without a solid immersion lens, then the position of the objective lens directly corresponds to a position on the sample surface. If two markers are then scanned over, with a known separation, it is relatively simple to determine the relative angle between the sample axis and the stage's via trigonometry.

If however a solid immersion lens is used, then as a result of the magnification from the SIL, movements of the objective lens are scaled accordingly. As has previously been mentioned, in order to determine the practical magnification of the system, the separation of two markers is used. If there is any angular offset then between the two sets of axis, a systematic error is introduced.

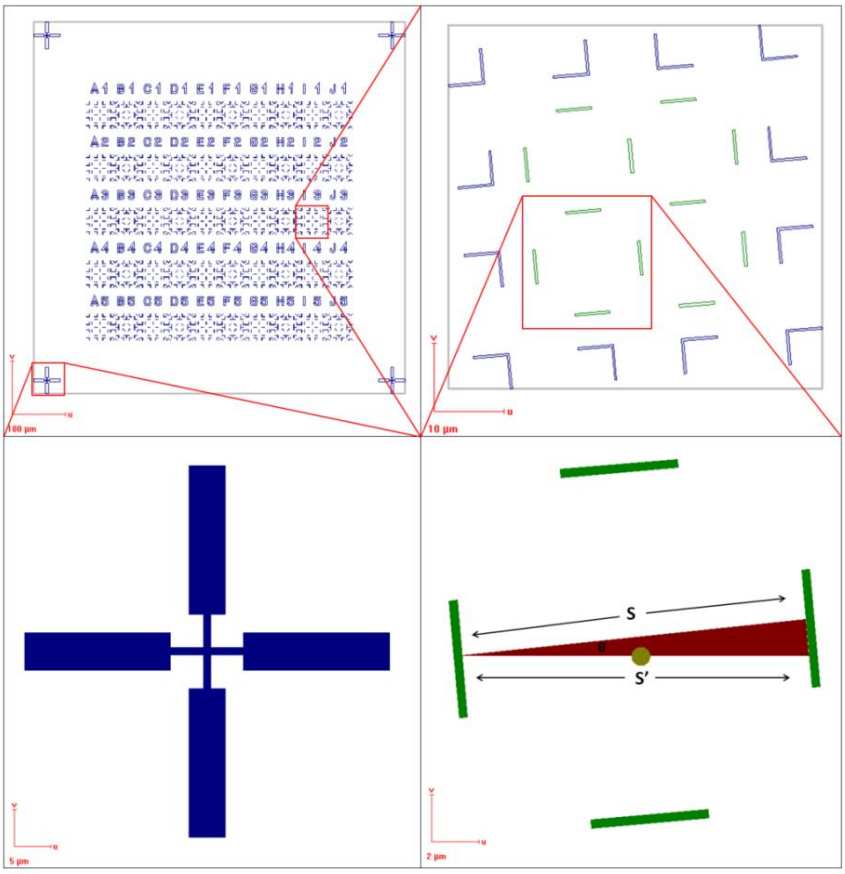

Figure 3-6 – Schematic depicting how an angular offset between the axis of the scanning stage and registration markers can introduce systematic errors in the registered position of the quantum dot. (Top left) Overview of a registration marker cell showing the four course alignment markers used to manually alight the EBL prior to sequential fabrications with a close up of an individual maker shown (bottom left). (Top right) Image of a single registration grid rotated as would be observed if the sample is misaligned with respect to the scanning stage axis. (bottom right) Depiction of how rotation of the sample results in an increased measured length for both the quantum dot position and marker separation.

In order to mitigate problems as a result of this, significant care is taken when initially aligning the sample to ensure orthogonality between the pre-fabricated registration markers and the scanning stage of the objective lens. As such, checks are performed using the EBL coarse write field alignment markers as depicted in Figure 3-6. As these markers are parallel or perpendicular to the axis of the registration markers, if the scanning stage is aligned to these, then it will also be aligned to the registration markers. Alignment is achieved by manually rotating the cryostat until it is possible to scan between adjacent

markers using a single axis of the scanning stage. As the separation of the EBL coarse field alignment markers is relatively large, typically more than 400 µm, it is possible to reduce the angle offset between the sample and the scanning stage to less than half a degree. If the upper limit of half a degree is considered, then the actual position of the quantum dot as presented in Figure 3-6, would be systematically shifted by 3.8×10^{-3} %. For a median displacement of 7.5 µm, this corresponds to an error less than 0.3 nm, and it is therefore not considered to be significant when compared to the physical size of the quantum dot.

3.3. Registration

Initial experiments to determine the viability of dot registration were done without the use of a solid immersion lens. The primary focus of these probing experiments was to determine optimal parameters and identify additional limiting factors, as well as identify systematic sources of error. By identifying impediments to the registration technique without the involvement of the solid immersion lens, objectivity can be maintained. It is reported in the literature that for a conventional micro-photoluminescence setup, the precision in the positional accuracy saturates at approximately 50 nm. In attempting to replicate this success, any limiting factors should be readily identified as a broadening in the distribution of the relative position.

The relationship between the step-size of the objective lens and the error in the quantum dots position is unknown. Therefore, several data sets are simulated containing two displaced Gaussian peaks, one representing the quantum dot and the other representing a marker. The properties of the two peaks are chosen to be identical, both with a FWHM of 1 µm. Random noise is introduced into the simulated data sets with an amplitude 6% of the peak intensity in order to approximate experimental observations. The same least squared fitting procedure which is used to process measured quantum dot data is used to determine the distance between the simulated peaks. The resolution of the simulated data sets is chosen from 1 µm to 50 nm to represent various resolutions which could be used during registration measurements. For a selection of the simulated data sets, empirical measurements are performed on a suitable quantum dot to determine the validity of the modelled data. Results are presented in Figure 3-7 which show good agreement between the observed and expected distribution width.

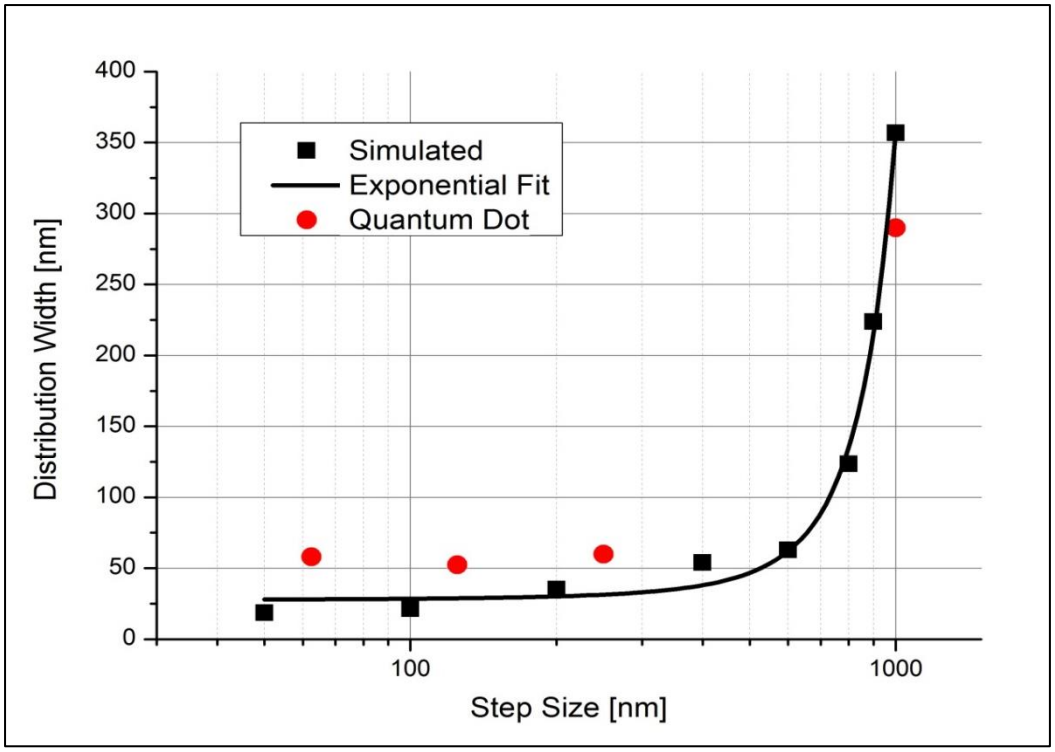

Figure 3-7 – FWHM of the relative quantum dot position for both simulated (black) and measured (red) data for a conventional photoluminescence registration setup with a resolution of approximately 1µm

From the simulated data presented in Figure 3-7, it could be assumed that by decreasing the step size between scan points during registration, incrementally smaller improvements in the accuracy could be achieved. However, as the error in the mean value of a normal distribution is equal to $\frac{\sigma}{\sqrt[2]{N}}$, where σ is the standard deviation and N is the number of data points, the observed exponential decay means that it can be beneficial to use larger step sizes and simply perform additional scans. If the total time taken to achieve an arbitrary error for the mean of the normal distribution is proportional to $\frac{\mathrm{N}}{\Delta \mathrm{x}}$, where $\Delta \mathrm{x}$ is the step size of the objective lens, then by using the exponential fit to the simulated data from Figure 3-7, the relationship between step size and experimental time required to achieve a given error can be determined, as shown in Figure 3-8.

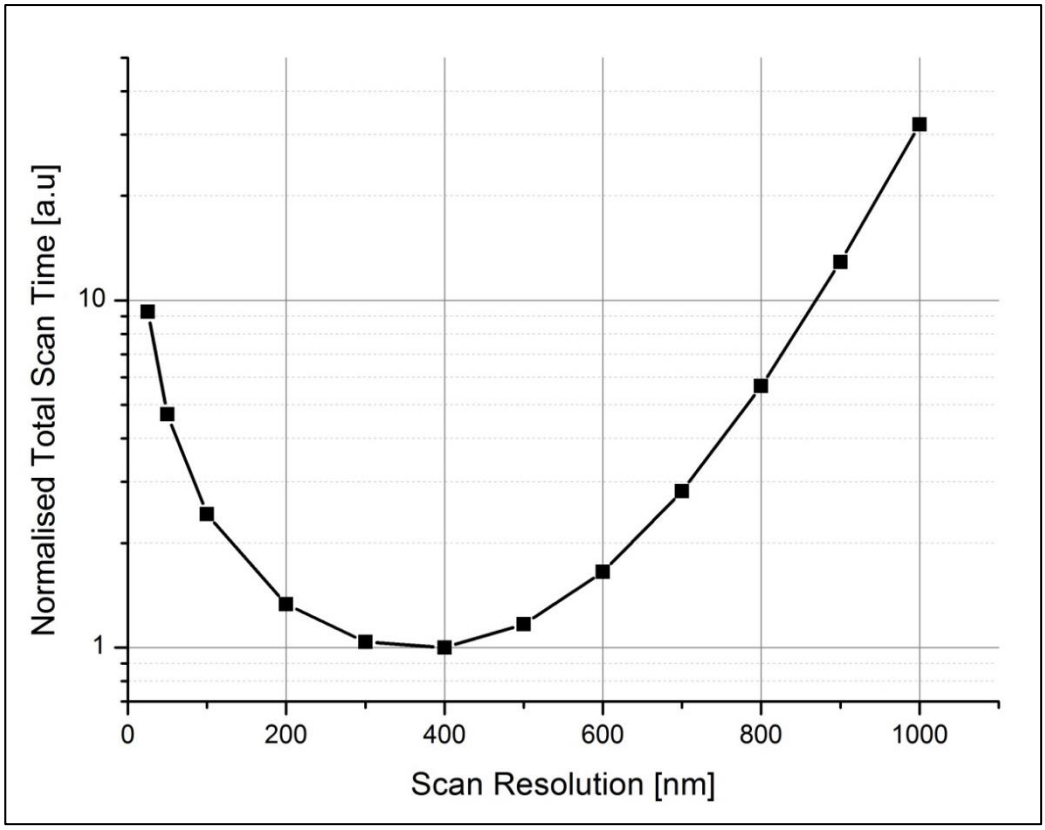

Figure 3-8 – Total time taken to achieve an arbitrary error for the position of a quantum dot as a function of the scan resolution. Total time is calculated assuming the error increases exponentially with the step size, that the number of scans required to achieve a given error is proportional to the square of the error in a single scan and that the time taken is proportional to the number of scans and inversely to the step size

For the purpose of this work, it is not the aim to find the most efficient scheme of registering quantum dots for deterministic fabrication. Rather it is to determine the best possible accuracy that can reproducibly be achieved when using a solid immersion lens. It would prematurely seem then that a finer step size will always result in a reduced distribution width for the relative position of a quantum dot. This however does not take into account systematic sources of error which may be time dependant.

3.3.1. System stability

In the process of identifying the optimal scan parameters, it was observed that the positions of the quantum dot and markers changed with time. This affect is anticipated due to instabilities as a result of vibrations, as well as a torque from the liquid helium transfer tube. Provided that the quantum dot and marker both drift at the same rate, and that the rate of drift is small on the time scale of a single scan, then this is not expected to result in significant systematic errors.

For a set of 100 scans with a scan resolution of 250 nm, the central position of the quantum dot and a marker are determined as a function of time. The results of the scans are presented in Figure 3-9 which show a drift rate of approximately 16 nm min^{-1} for both the marker and quantum dot position. Whilst this drift rate is not negligible, on the time scale of a single scan (approximately 10 to 20 seconds), it only represents a systematic error in the relative position of the quantum dot of approximately 4.0 nm in each scan. We comment that whilst the linear fit to the data does in general agree with the observed trend, it is not expected that the sample drift should always behave in a linear manor.

Furthermore, whilst it is expected that the marker and quantum dot positions should drift parallel to one another, the linear fits to the data show only a small relative drift of 1.4 ± 1.2 nm min^{-1} between the marker and the quantum dot. By plotting the relative distance between the quantum dot and one of the registration markers as a function of time, as shown in Figure 3-10, it becomes apparent that the relative drift between the two peaks is likely a result of statistical noise.

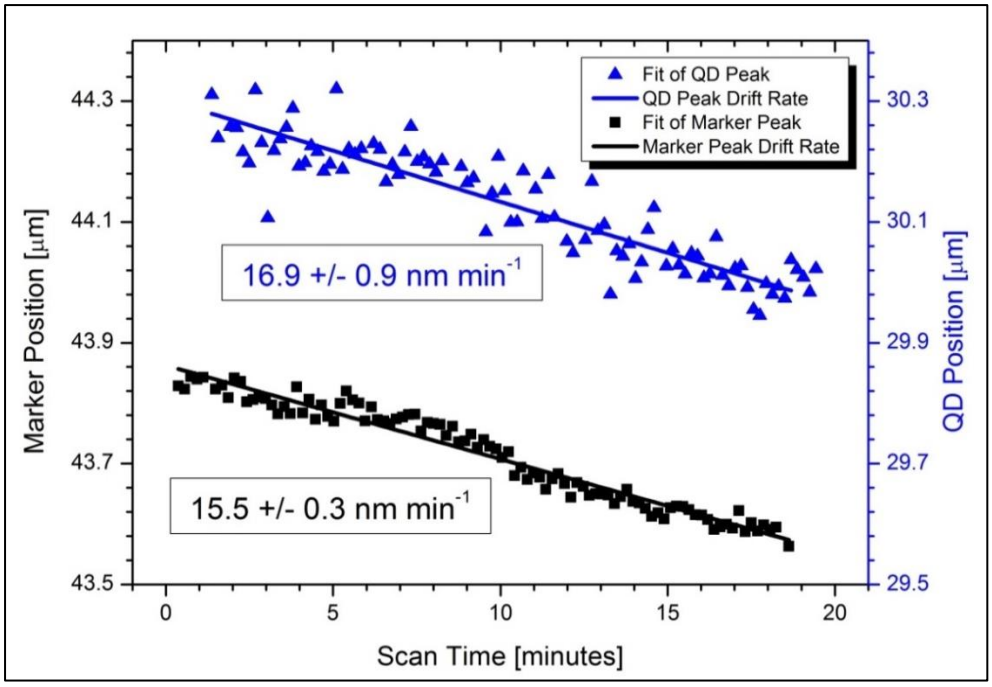

Figure 3-9 – Observed drift in the position of a quantum dot and registration marker due to mechanical instabilities of the system. Positions shown are the centre of a Gaussian fit to the collected signal and represent the absolute position of the objective lens on the scanning stage.

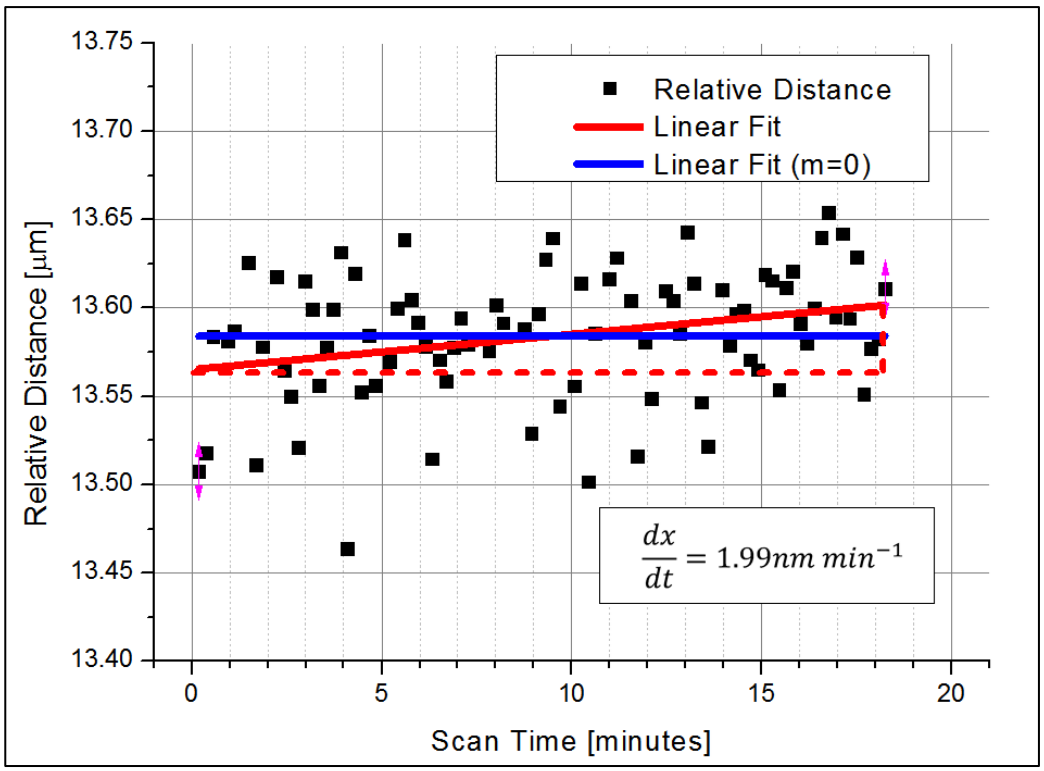

Figure 3-10 – Centre of a Gaussian fit for the relative position of the quantum dot to a registration marker as a function of the scan time (black). A least squared constant (blue) and linear fit (red) fit is performed to the data to determine the relative drift rate between the quantum dot and the markers. An upper bound of 1.99 nm min^{-1} is calculated, however this is considered to be due to the relatively large fluctuations in the calculated relative distance.

As a precaution due to the observed sample drift, the step size of the objective lens during registration scans of 250 nm has been determined appropriate to achieve optimal accuracy during dot registration whilst minimising the overall scan time, and therefore systematic errors associated with sample drift. The expected lower limit for the distribution width, full width at half maximum, at this step size is 31.4 nm from Figure 3-7. If the step size was increased to 100 nm, then the distribution width would be expected to reduce to 28.5 nm. This reduction of 2.9 nm would increase the time of each scan by a factor of 2.5, and therefore increasing the systematic error due to sample drift from 4 nm to 10 nm. Whilst it is possible to correct for this systematic error to some degree, there will always be an inherent error carried forwards. It is therefore preferable to simply reduce the run time to mitigate its impact.

In practice, it was found that even with smaller and smaller step sizes, the FWHM that could be achieved during measurements for the relative position of a quantum dot plateaued at a step size 250 nm. The smallest FWHM in the relative position of a quantum dot that was obtained without a solid immersion lens is shown in *Figure 3-11* where a

FWHM of 52.8 nm was obtained. This value is very close to the ~ 50 nm value reported by others [2][23] and therefore provides confidence in the registration setup.

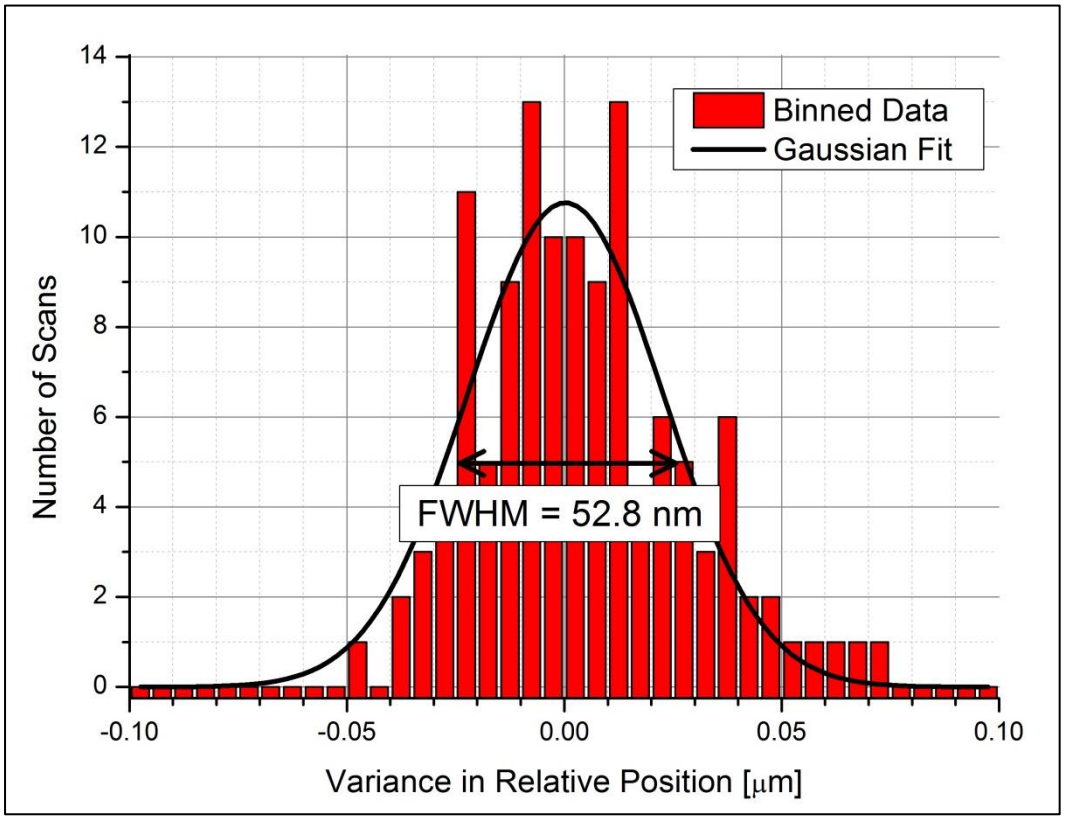

Figure 3-11 – Histogram of the Variance in the relative position (in a single axis) calculated for a quantum dot relative to a registration marker. A Gaussian peak (black) is fitted to the measured data (red) which shows a FWHM of 52.8 nm. This value is in good agreement with the best values reported in the literature for similar setups.

3.3.2. Surface Damage

In order for the micro photoluminescence setup to achieve optimal resolution with a solid immersion lens, and therefore realise the highest benefits for registration purposes, the solid immersion lens must be in mechanical contact with the samples surface. The surfaces of the solid immersion lens, specifically the bottom one in contact with the sample, are finely polished to achieve a high quality optical finish. It is contrary to expectations, that it is observed that due to fine positioning of the lens on the samples surface, extensive damage can be done to the wafers surface in the form of scratches. A scanning electron microscope image which shows a significantly damaged registration grid with a waveguide is presented in Figure 3-12. Whilst surface damage of this extent was not observed for all samples studied, at least some level of surface damage was found. It was also found that the extent of the damage was increased when using a

mechanical positioner, rather than high viscous bonding, as a result of the increased normal force.

From the SEM image in Figure 3-12, line sections are taken through several scratches and show a maximum width of approximately 200 nm. From the SEM image alone, the depth of the scratches cannot be determined, however, as the quantum dots are only 70 nm away from the surface, it is expected they will by highly sensitive to any defects. Furthermore, any such scratches on the surface of a wafer where a photonic structure is fabricated will manifest as scatter points, reducing the overall performance of the device.

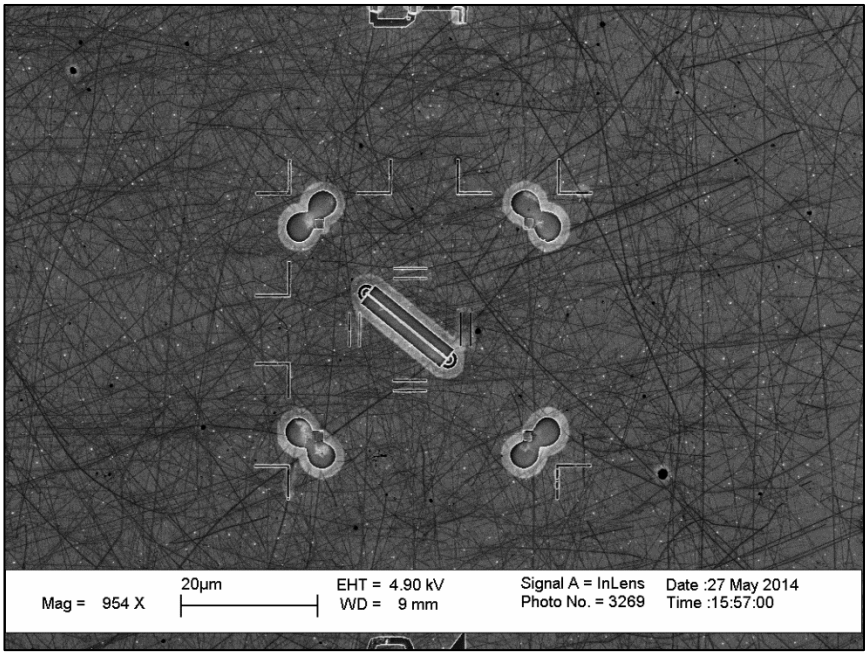

Figure 3-12 – SEM Image of a sample which has had a solid immersion lens repeatedly positioned on the surface of the sample. Due to the small aberration free image region of solid immersion lenses, it is necessary to precisely align the centre of the lens with the centre of the registration markers.

The cause of such scratches is believed to be due to the relatively soft gallium arsenide with respect to the cubic zirconium solid immersion lens. In order to characterise a materials resistance to scratching, the Mohs scale is used which ranks materials on their relative abilities to, and to be, scratched. Gallium Arsenide has a Mohs rating of 4.5 [28], whereas the ZrO_2 solid immersion lens has a rating of 8 [29], making if far more likely to scratch GaAs and less likely to be damaged. Numerous white specs are present in Figure 3-12 with saturated contrast which represents small fragments of surface contamination. It is thought that small pieces of contaminants will be present on the surface of the sample due to the normal handling of samples which often results in slight damage to the

edges of the wafer. Additionally, where etched features exist, the sharp corners of these features will be prone to chipping, resulting in additional contaminants.

We report measurements for the roughness of the contact surface of the solid immersion lens, after it has been used for dot registration and finely positioned over a registration grid. Measurements are performed using atomic force microscopy with topological plots shown from various locations of the SIL in Figure 3-13. AFM measurements are performed using a pinhole mount to hold the inverted solid immersion lens stable during scanning, where representative points were taken at several locations near the middle and edge of the lens. It is expected that large areas of optically flat regions will exist, with several contaminated regions where GaAs fragments have been transferred.

The identification of contaminants on the solid immersion lens, with typical widths corresponding to the sizes of observed scratches provides confidence as to the origin of the scratches. As a preventative measure to protect the samples surface from damage of this type during dot registration, a temporary layer of 100 nm thick SiO_2 is deposited on top of the fabricated registration markers. As SiO_2 has a Mohs rating 7 [30], much higher than that of GaAs, damage to the samples surface will be significantly reduced. Furthermore any damage to this surface is not expected to penetrate through the SiO_2 layer to the GaAs.

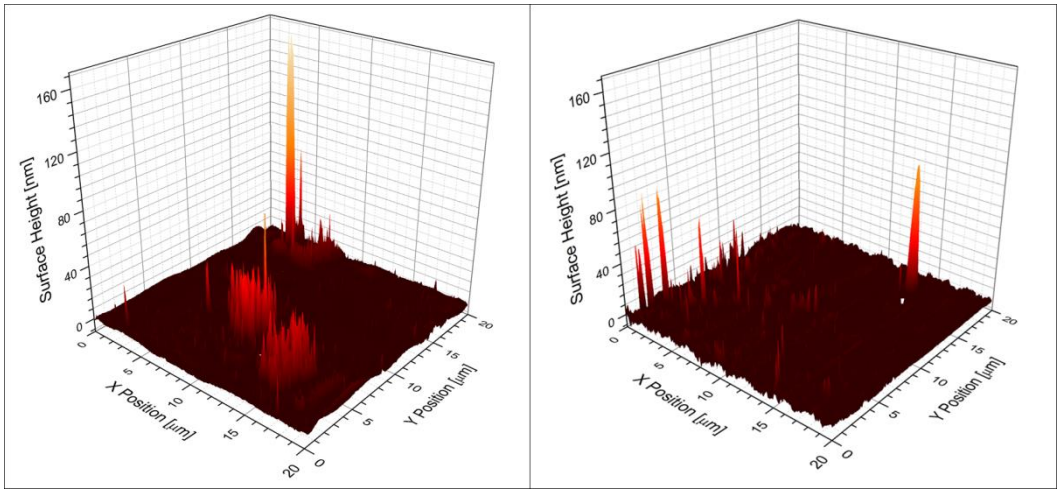

Figure 3-13 – Atomic Force Microscopy images of a 1 mm diameter solid immersion lens after it has been used for dot registration. Images show two representative points near the middle (left) and edge (right) of the solid immersion lens. The majority of the surface is seen to be optically smooth, with contamination spots 10 nm to 200 nm in size.

Plasma enhanced chemical vapour deposition (PECVD) is used to deposit the SiO_2 onto the sample surface at a rate of 40 nm per minute. Once the sample has been studied, and

a suitable number of quantum dots registered, the SiO_2 can be removed in a weak, 10% by volume, hydrofluoric acid solution for 60 seconds. After removing the SiO_2, the sample can be processed as normal should the fabrication of photonic structures be desired.

We present two SEM images in Figure 3-14 which show the surface of a wafer with registration markers; initially after the deposition of SiO_2, and after the SiO_2 has been removed after being used to protect the sample from positioning a solid immersion lens. It is noted that excessive force is used in a deliberate attempt to scratch the sample shown in Figure 3-14 to ensure that sufficient protection is provided by the SiO_2. By comparison of the two images, no evidence of surface damage as a result of scratching is observed, validating the use of a hard mask to protect the samples surface.

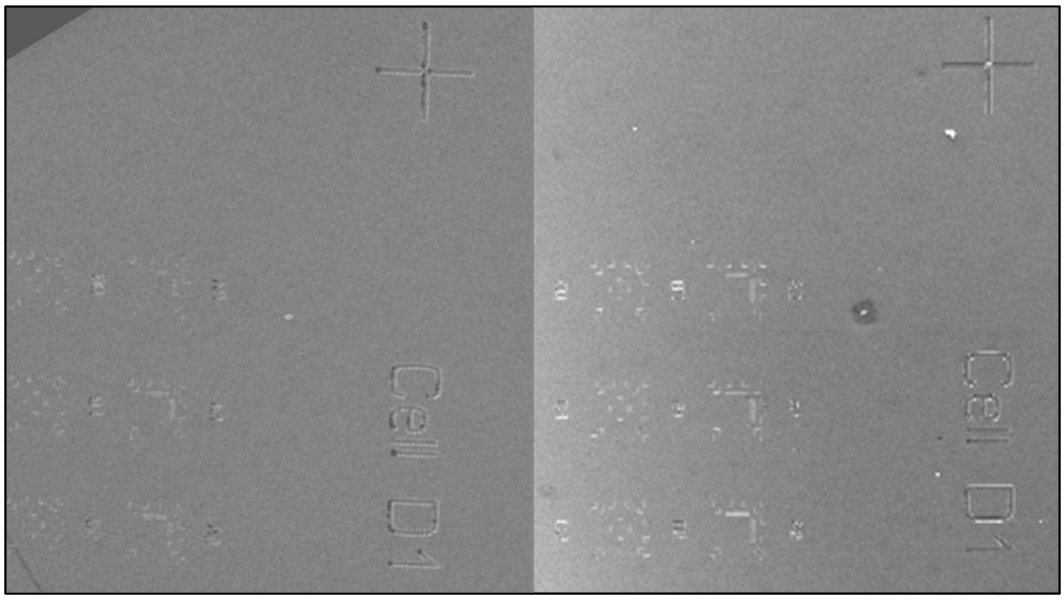

Figure 3-14 – (Left) SEM image of a wafer after registration markers are fabricated but prior to SiO_2 deposition. Due to the number of processing steps required to fabricate registration markers (Cleaving, Spin-coating, EBL, Development and Etching) repeated manual handling of the device has already introduced some level of contaminates as highlighted (red circle). (Right) SEM image after the protective SiO_2 layer has been removed showing no signs of surface damage. A small area of decreases contrast is apparent around a wafer fragment which is thought to have been trapped under the SiO_2 which may have acted as a nucleation site for deposition.

Where a fragment of semiconductor is present in both SEM images, it is likely that it has become trapped under the SiO_2 layer. These particulates on the wafer surface will act as a nucleation site during PECVD, increasing the local thickness of SiO_2 at that point. As a result, these areas may not be fully removed by the hydrofluoric acid in a single 60 second etch, and hence explains the presence of the dirt in both SEM images, as well as the darker region surrounding it. It is not thought that this will have any significant effect on

either dot registration, or the performance of fabricated structures, provided that contamination spots are suitably far away.

The protective qualities of SiO_2 are evident. However it is necessary to confirm that the properties of quantum dots are not detrimentally affected by its presence. That is, a quantum dot must exhibit the same spectral properties, both with and without the SiO_2 layer. If any significant spectral changes occur as a result of the protective layer, then the ability to selectively register quantum dots based on its properties is lost.

To determine the effects of the protective layer on the photoluminescence of quantum dots, two sets of three dimensional colour contour plots for a single registration grid are produced, both before and after the deposition of SiO_2. The collected photoluminescence is detected via the CCD of the spectrometer, rather than an APD, to preserve the full spectral information for all quantum dots within the registration grid. In order to prevent scratches affecting the properties of the quantum dots before the protective SiO_2 is deposited, the scans are performed without the aid of a SIL.

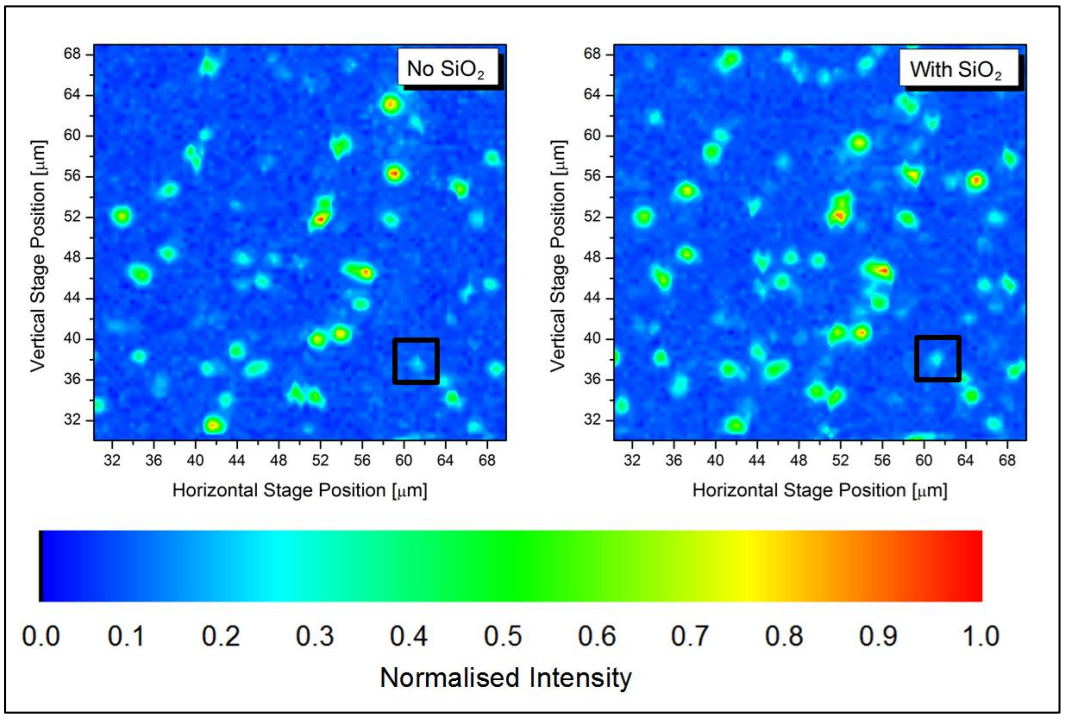

Figure 3-15 – Colour contour plots showing integrated photoluminescence signal recorded over the spectral range of 900 – 950 nm for the same registration grid before and after SiO_2 has been deposited on the samples surface.

Scan parameters were fixed between the two scans to enable a direct comparison. As multiple excitonic states are typically observed in our samples for individual quantum

dots, a high excitation power is used to produce the contour graphs. A near saturation power of approximately 2.0 μW for the HeNe (λ_0 = 633 nm) excitation laser is chosen, with a scanning stage resolution of 500 nm. The integration time on the CCD is set to 500 ms to provide sufficient signal contrast, whilst maintaining an overall short scan time to reduce the effects of drift.

Integrating the recorded intensity spectrums over a large spectral range (900 nm to 950 nm), and normalising to the maximum value, a colour contour plot is produced which shows the locations of nearly all quantum dot within the registration grid, and removes fluctuations due to the wetting layer and GaAs band gap. Figure 3-15 presents the colour contour plots for the same registration grid before and after SiO_2 has been deposited. Prior to the second scan, the scanning stage is manually re-aligned to the same registration grid, however some level of offset between the two scans is expected.

Good agreement is found between the two contour maps, with a calculated RMS difference of $< 2\%$. By calculating the residual between the two plots, as shown in Figure 3-16, it is possible to highlight where any significant differences occur. We identify apparent artefacts in the residual plot, with an example highlighted inside the red box, where at the site of a quantum dot, the sign of the residual changes from positive to negative over a short period. The origin of this affect is believed to be a result of an artificial hysteresis of the stage positions introduced when producing the contour plots. Whilst the scanning stage is operated in a closed loop providing accurate recordings of its position, in order to produce the colour contour plots, it is necessary to bin the positions recorded during the scans. This sign change is therefore attributed to a small spatial offset of the scanning stage.

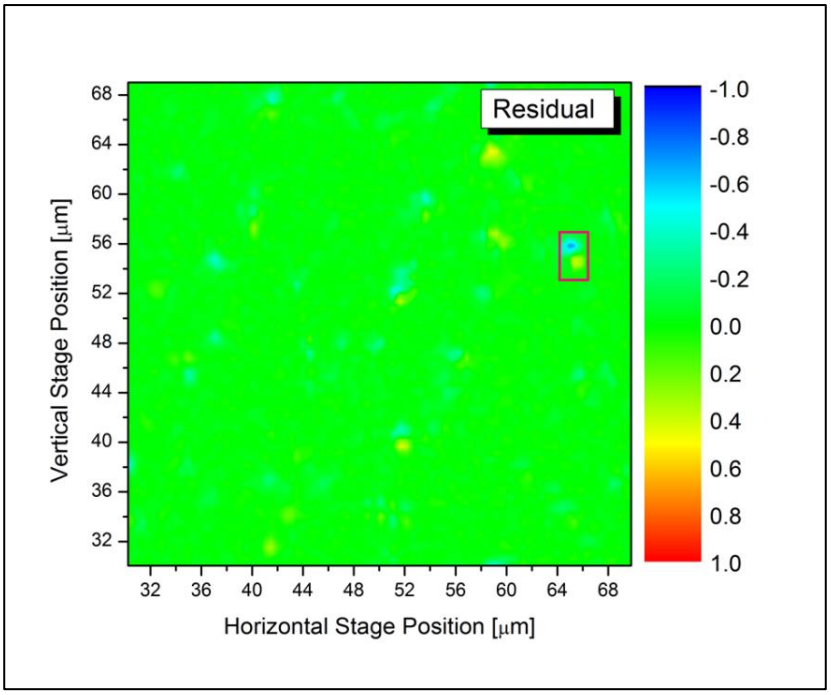

Figure 3-16 – Residual between the colour contour plots generated by integrating the observed photoluminescence spectrums over the wavelength range 900 – 950 nm for the same registration grid with and without SiO_2 deposited.

Further investigations of areas which appear to show moderate changes in signal intensity are found to be the result of a combination of factors. It is noted that quantum dots at these locations typically exhibit poor spectral properties, with numerous charged states present. Due to the increased number of relaxation pathways this provides, saturation of these dots typically require higher excitation power than those used to perform the scans. The recorded photoluminescence is therefore more sensitive to the position of the excitation laser. Subtle differences between the two scans are therefore explained as a result of the finite step size used to produce the scans.

Whilst the integrated intensity provides confidence that quantum dot emission is not quenched due to the protective layer, it provides little information regarding spectral consistency. We therefore show in Figure 3-17 a representative comparison of a typical quantum dot spectrum before and after the deposition of SiO_2. It is shown that the spectral features are nearly identical, with the dominant spectral line centred around 897 nm clearly visible before and after the deposition of SiO_2. Additionally, the presence of less dominant spectral features agree well with each other between scans, such as the cluster of states present around 902 nm. Apparent changes in the relative intensity of certain peaks are again attributed to the finite positional accuracy of the scan, and therefore a reduced excitation power felt by the quantum dot. It is therefore concluded

that the deposition of a SiO_2 hard mask, to act as a protective layer prior to dot registration, is acceptable.

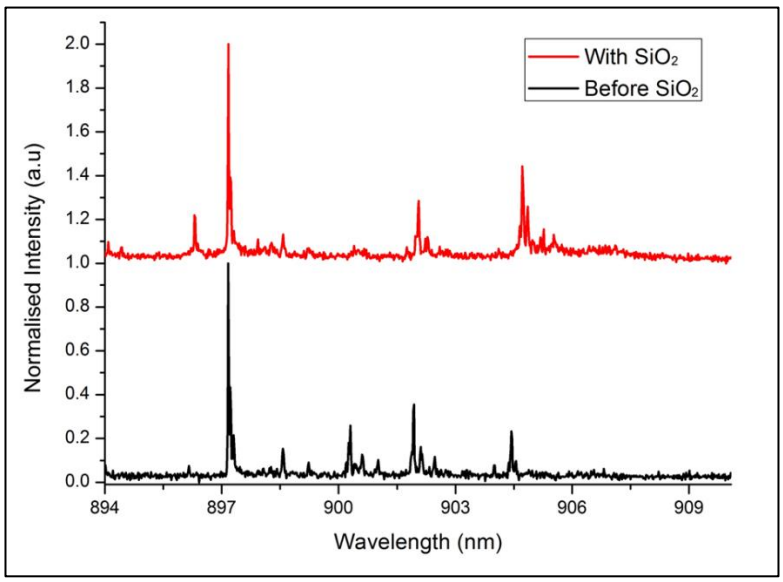

Figure 3-17 – Spectral comparison for a single quantum dot, identified by the relative position of its integrated photoluminescence signal, before (black) and after (red) the deposition of SiO_2 on the surface of the sample. The relative intensities of peaks are seen to change which is attributed to the finite resolution of the scans performed. The ability to identify corresponding peaks in both spectrum provide confidence that the spectrum remains predominantly unchanged.

3.3.3. Solid Immersion Lens Enhanced Registration

With confirmation that a solid immersion lens can be used without having a detrimental effect on the sample, the viability of solid immersion enhanced dot registration is now explored. To ensure the absence of geometric aberrations as a result of the solid immersion lens, a 3D contour plot is first generated by measuring the reflected laser signal from the sample surface through the solid immersion lens using APD's as a function of the stage position. Should any distortion in the image be present, this would mean the assumption of a constant magnification over the small scan ranges considered is false. It would therefore be impossible to determine the relative position of the quantum dot as it would require precise knowledge of how the magnification changes with respect to the scanning stage's position.

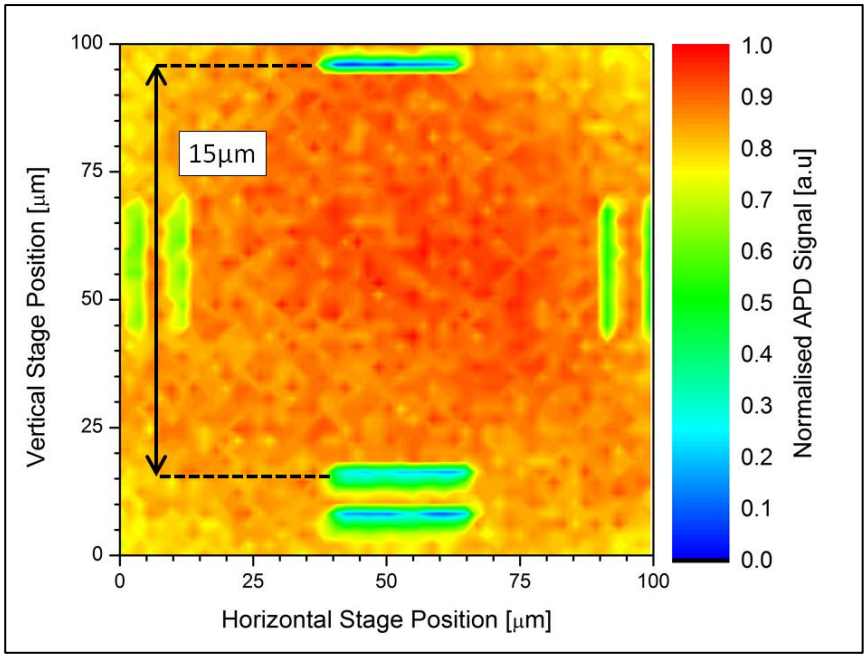

Figure 3-18 – Contour map showing reflected laser (λ_0=633 nm) signal from a single registration marker set when examined under a solid immersion lens. Areas of reduced signal intensity correspond to etched marker patterns.

The 2D contour map is present in Figure 3-18 which show a 15 µm by 15 µm registration grid with horizontal and vertical registration markers carefully aligned to the scanning stage axis. A scanning stage step size of 2 µm is used which, when accounting for the magnification of the SIL, corresponds to a resolution of better than 400 nm on the samples surface. By visual inspection, no obvious aberrations are apparent which would have been expected to manifest as curvature in the straight registration markers. A more precise measurement of the curvature is presented in Figure 3-19 where the relative separation of two markers is plotted as a function of position. The data is fitted well by a straight line with a gradient of $0.0 \pm 1.8\ \mathrm{nm\ \mu m^{-1}}$, confirming no significant distortions are present which would adversely affect the registration process.

For conventional dot registration, without the aid of a solid immersion lens, it was observed that relative drift between the sample and objective lens resulted in a continuous systematic error in the relative position. It has previously been stated, that when using a solid immersion lens, the travel distance of the objective lens is related to that of the excitation spot by the effective magnification. As such, the relative drift between the sample and the objective lens should also be reduced proportionally to the effective magnification of the SIL. For comparison with the system stability reported without the aid of a solid immersion lens ($1.99\ \mathrm{nm\ min^{-1}}$), the relative drift between the

quantum dot and a marker as measured under a solid immersion lens is presented in Figure 3-20.

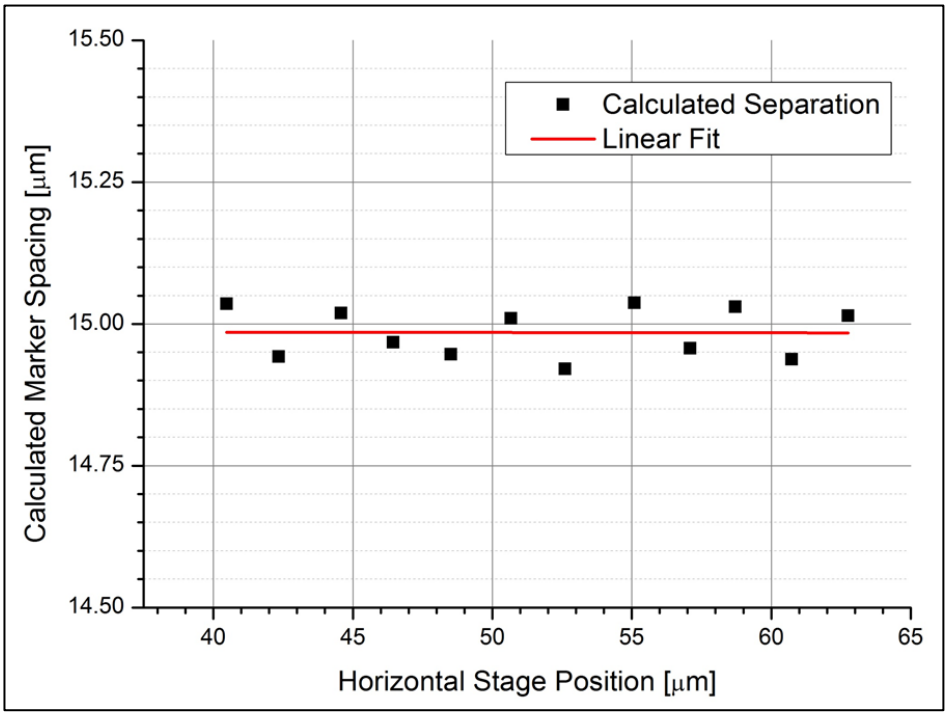

Figure 3-19 – Relative separation of the vertical registration markers (shown in Figure 3-18) as a function of horizontal position. A linear fit shows the separation is constant, and therefore no significant variation in the magnification is expected.

A relative drift rate of 0.12 nm min^{-1} is obtained which is significantly less than expected considering enhancements due to the magnification of the solid immersion lens alone. As the relative drift of the sample is subject to numerous environmental conditions, it is likely that the drift rate will fluctuate on a measurement by measurement basis. One such source of drift is considered to be vibrations as a result of back pressure within the helium return line due to the simultaneous operation of additional cryogenic systems. Whilst steps are already taken to minimise this affect using an additional expansion vessel, the affects cannot be controlled entirely. It is however enough for now to conclude that the use of a solid immersion lens shows a significant reduction in the drift rate, from 16.9 nm min^{-1} without a SIL, to as little as 0.9 nm min^{-1} with a SIL.

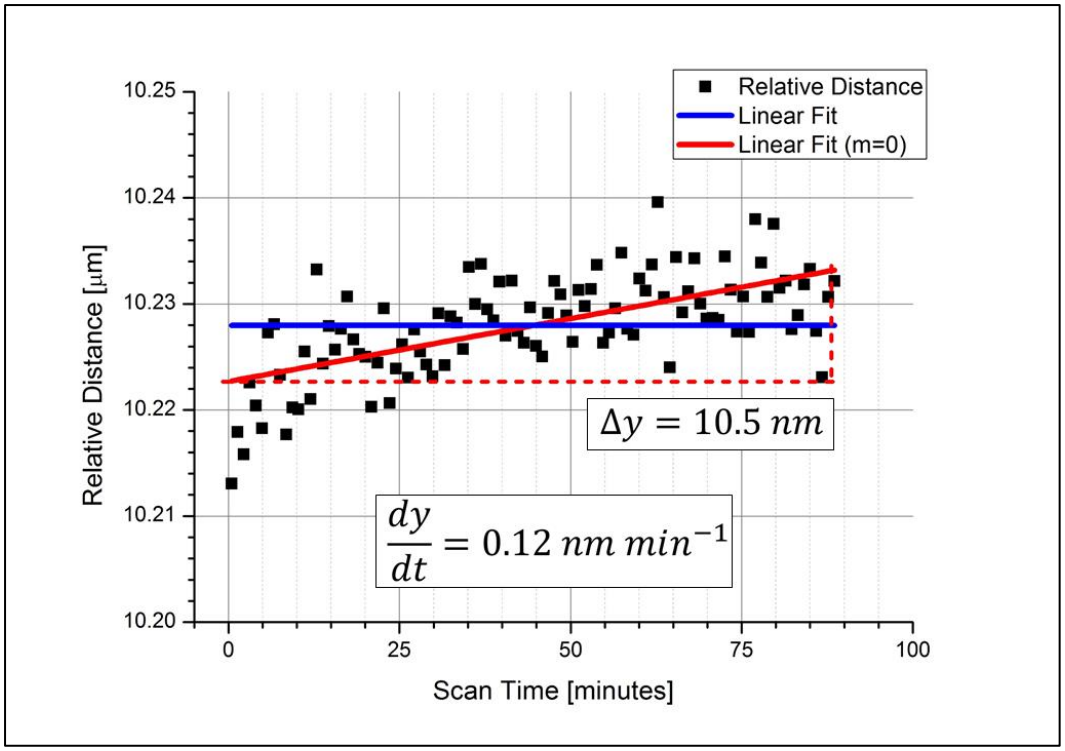

Figure 3-20 – Relative distance between quantum dot and registration marker as a function of time. An average drift rate of 0.12 nm min$_{-1}$ is calculated, which on the time scale of a single scan (~1.5 min) represents a negligible error.

As with conventional dot registration, it is seen that the distribution width was strongly dependent on the step size used to move the objective lens during scans. Without the aid of a solid immersion lens, the distribution width of the relative position of the quantum dot was seen to saturate at 52.8 nm (see Figure 3-11). This was the case for step sizes of the objective lens of less than a few hundred nanometres. When a solid immersion is used in the optical setup to register the position of a quantum dot, it should be seen that a similar step size for the objective lens is required. The reason the a similar step size should be required, is that the resolution of the system is increased by the SIL by the same factor which relates the translation of the objective stage to the translation of the focused spot on the samples surface. This is confirmed by measuring the position (in one axis) of a single quantum dot for various step sizes. A similar exponential decay is observed to that of the one in Figure 3-7, as shown in Figure 3-21, which suggest the resolution saturates at 10 nm. This distribution width is significantly better than that observed for conventional dot registration, which represents an improvement by approximately a factor of 5. This value is in good agreement with the magnification provided by the solid immersion lens, which is equal to the refractive index squared. For the cubic zirconia solid

immersion lens used, with a refractive index of 2.12 at 925 nm [31], the magnification is expected to increase by a factor of approximately 4.5.

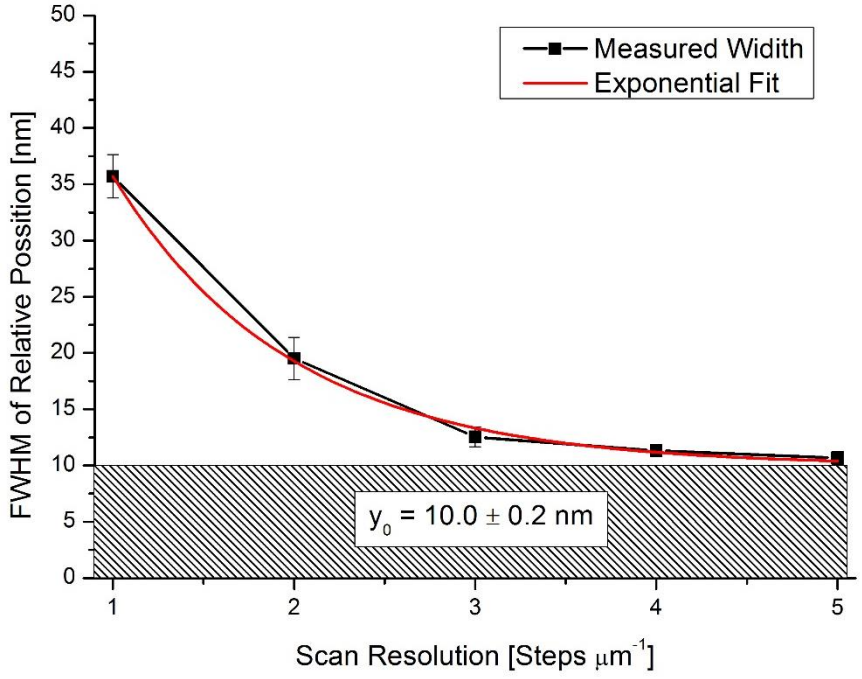

Figure 3-21 – FWHM for the relative position of a quantum dot measured with various scan resolutions in a single axis. An exponential decay is fit (red) to the data (black) which shows good agreement and predicts a maximum accuracy of 10 nm.

Based upon the data presented in Figure 3-21, it is proposed to use a scan resolution of 250 nm (4 steps μm^{-1}). If the resolution was increased to 200 nm, the FWHM was shown to decrease by 0.6 nm. Given this would result in a 25 % increase in the total scan time, it is likely to result in larger systematic errors than the 0.6 nm decrease in the measured distribution width.

Using the proposed scanning stage resolution of 250 nm, line scans are repeated 100 times in order to produce a statistical distribution for the relative position of the quantum dot. The peak registration accuracy observed was calculated to have a distribution width of 8.58 nm for the relative position. A histogram showing the variance in the calculated relative position between the quantum dot and one of the registration markers is presented in Figure 3-22. The Gaussian fit to the data results in an adjusted residual squared value of 0.949, confirming good agreement. The significance of this is that the Gaussian nature of the distribution suggests limitations in the accuracy of the technique are dominated by random noise, such as vibrations, intensity fluctuations or electronic instrumentation noise. It is therefore appropriate to use the average value calculated for

deterministic fabrication. Based on the 100 line scans used to generate the histogram, the error in the central position is calculated to be 0.36 nm $\left({}^{\sigma}/_{\sqrt{N}}\right)$.

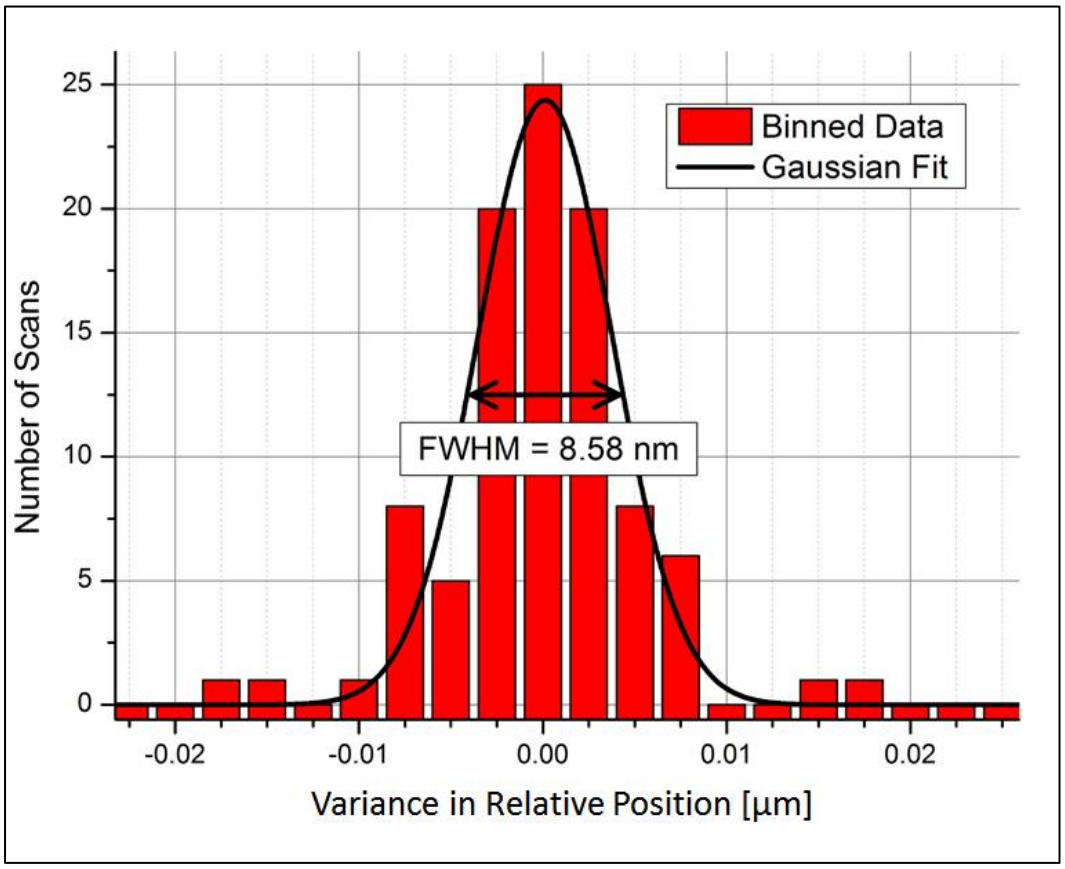

Figure 3-22 – Histogram of the variance in the relative positions (in a single axis) calculated for a quantum dot relative to a registration marker. A Gaussian peak (black) is fit to the measured data (red) which shows a FWHM of 8.58 nm. Based on 100 scans, the error in the mean position is calculated to be 0.36 nm.

In order to both confirm the reproducibility and validity of the claim of such a significant improvement in the distribution width due to the SIL, the positions of several quantum dots are registered, ideally to be used later in photonic structures. A scatter plot showing the distribution widths calculated for the relative position of each of the dots registered is shown in Figure 3-23.

It is clear from the scatter plot that the use of a solid immersion lens results in a measurable improvement in the achievable accuracies, with at best, an 82% reduction in the distribution width over the best accuracies achieved without the use of a solid immersion lens. Although significant variance exists in the values reported, the largest distribution width of approximately 30 nm still represents a 20 nm improvement due to the SIL.

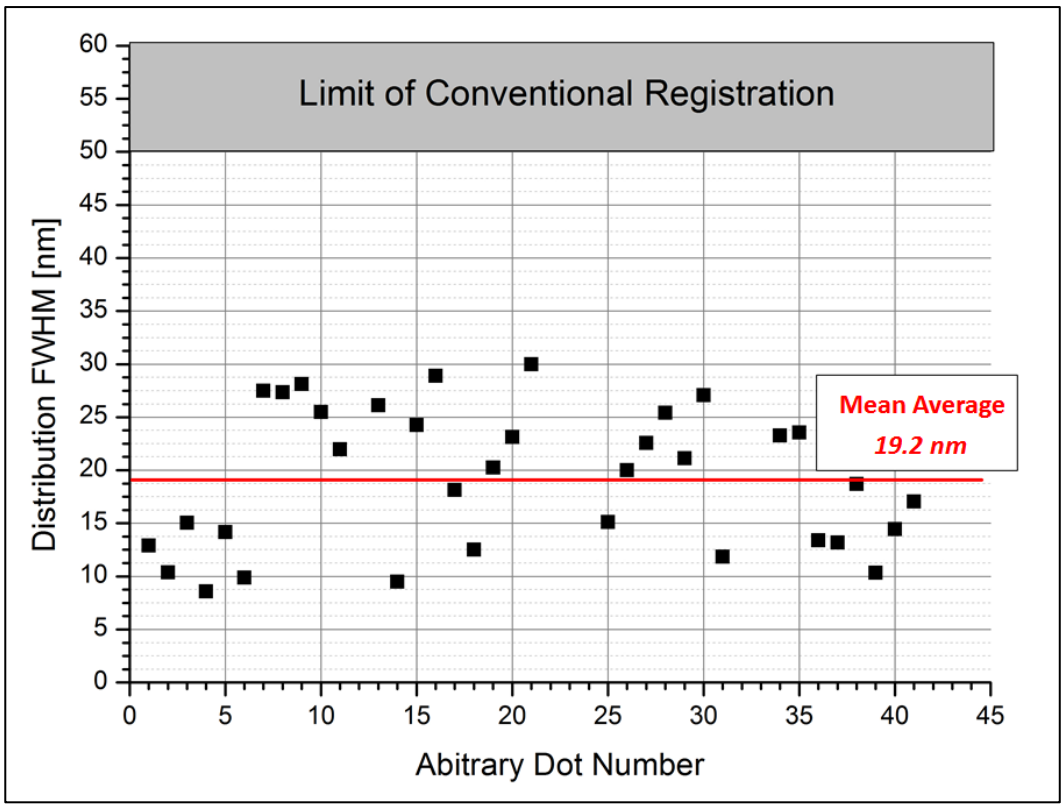

Figure 3-23 – Scatter plot showing the FWHM for the relative positions measured of several quantum dots using solid immersion lens enhanced dot registration. A mean distribution width of 19.2 nm is calculated, significantly below the 50 nm limit which is observed for conventional dot registration. A maximum and minimum distribution width of 30.0 nm and 8.6 nm respectively.

3.4. Conclusion

Using a scanning micro-photoluminescence setup, the statistical variance in the calculated relative position of a quantum dot has been measured, both with and without the use of a solid immersion lens. Without the use of a solid immersion lens, the smallest distribution width experimentally achieved was found to agree well with other groups who also report a distribution full width at half maximum of approximately 50 nm. It has been confirmed that the use of a solid immersion lens can significantly increase the accuracy of the dot registration technique, resulting in a distribution width of 8.58 nm at best for the position of a quantum dot relative to a registration marker.

Whilst in principle, numerous repeat scans may be performed to reduce the error in the calculated position, this can be time consuming. Due to the reduced distribution width observed when using a SIL, nearly 34 times as many scans would be required of the conventional registration setup in order to achieve the same error in the calculated position. Additionally, as the solid immersion lens effectively desensitises the registration

system to vibrations and drift between the sample and objective lens, systematic errors as a result of sample drift are shown to be reduced.

Although the solid immersion lens was found to damage the surface of the wafer, it has been shown that the use of a temporary SiO_2 layer can be used as a protective layer to mitigate this. SEM images, integrated photoluminescence contour plots and spectral comparisons of quantum dots before and after the deposition of SiO_2 have shown that the use of a SiO_2 layer has no detrimental effects on the sample, or the photoluminescence properties of the quantum dots.

3.5. References

[1] A. Imamoglu, D. Awschalom, G. Burkard, D. P. DiVincenzo, D. Loss, M. Sherwin, and A. Small, "Quantum information processing using quantum dot spins and cavity QED," *Phys. Rev. Lett.*, vol. 83, no. 20, pp. 4204–4207, 1999.

[2] S. M. Thon, M. T. Rakher, H. Kim, J. Gudat, W. T. M. Irvine, P. M. Petroff, and D. Bouwmeester, "Strong coupling through optical positioning of a quantum dot in a photonic crystal cavity," *Appl. Phys. Lett.*, vol. 94, no. 11, p. 111115, 2009.

[3] P. Lodahl, S. Mahmoodian, and S. Stobbe, "Interfacing single photons and single quantum dots with photonic nanostructures," *Rev. Mod. Phys.*, vol. 87, no. 2, pp. 347–400, 2015.

[4] R. J. Coles, D. M. Price, J. E. Dixon, B. Royall, E. Clarke, P. Kok, M. S. Skolnick, A. M. Fox, and M. N. Makhonin, "Chirality of nanophotonic waveguide with embedded quantum emitter for unidirectional spin transfer.," *Nat. Commun.*, vol. 7, no. 2015, p. 11183, 2016.

[5] D. Englund, D. Fattal, E. Waks, G. Solomon, B. Zhang, T. Nakaoka, Y. Arakawa, Y. Yamamoto, and J. Vučkovićc, "Controlling the spontaneous emission rate of single quantum dots in a two-dimensional photonic crystal," *Phys. Rev. Lett.*, vol. 95, no. 1, pp. 2–5, 2005.

[6] A. P. Foster, "Theoretical and experimental investigation of III-V semiconductor nanowire heterostructures," no. November, 2013.

[7] T. B. Hoang, A. F. Moses, H. L. Zhou, D. L. Dheeraj, B. O. Fimland, and H. Weman, "Observation of free exciton photoluminescence emission from single wurtzite GaAs nanowires," *Appl. Phys. Lett.*, vol. 94, no. 13, pp. 1–4, 2009.

[8] K. A. Dick, "A review of nanowire growth promoted by alloys and non-alloying elements with emphasis on Au-assisted III-V nanowires," *Prog. Cryst. Growth Charact. Mater.*, vol. 54, no. 3–4, pp. 138–173, 2008.

[9] T. Mårtensson and P. Carlberg, "Nanowire Arrays Defined by Nanoimprint Lithography - 2004 - Mårtensson et al.pdf," *Nano Lett.*, no. Cvd, pp. 8–11, 2004.

[10] L. K. Van Vugt, S. J. Veen, E. P. A. M. Bakkers, A. L. Roest, and D.

Vanmaekelbergh, “Increase of the photoluminescence intensity of InP nanowires by photoassisted surface passivation,” *J. Am. Chem. Soc.*, vol. 127, no. 35, pp. 12357–12362, 2005.

[11] B. N. J. Persson and N. D. Lang, “Electron-hole-pair quenching of excited states near a metal,” *Phys. Rev. B*, vol. 26, no. 10, pp. 5409–5415, 1982.

[12] M. N. Makhonin, A. P. Foster, A. B. Krysa, P. W. Fry, D. G. Davies, T. Grange, T. Walther, M. S. Skolnick, and L. R. Wilson, “Homogeneous array of nanowire-embedded quantum light emitters,” *Nano Lett.*, vol. 13, no. 3, pp. 861–865, 2013.

[13] C. Cheng and H. J. Fan, “Branched nanowires: Synthesis and energy applications,” *Nano Today*, vol. 7, no. 4, pp. 327–343, 2012.

[14] D. Q. Yang and E. Sacher, “Accurate assembly and size control of cu nanoparticles into nanowires by contact atomic force microscope-based nanopositioning,” *J. Phys. Chem. C*, vol. 111, no. 27, pp. 10105–10109, 2007.

[15] M. E. Reimer, G. Bulgarini, A. Fognini, R. W. Heeres, B. J. Witek, M. A. M. Versteegh, A. Rubino, T. Braun, D. Dalacu, J. Lapointe, P. J. Poole, and V. Zwiller, “Overcoming power broadening of the quantum dot emission in a pure wurtzite nanowire,” vol. 195316, pp. 1–9, 2016.

[16] J. Tatebayashi, Y. Ota, S. Ishida, M. Nishioka, S. Iwamoto, and Y. Arakawa, “Site-controlled formation of InAs/GaAs quantum-dot-in-nanowires for single photon emitters,” *Appl. Phys. Lett.*, vol. 100, no. 26, 2012.

[17] C. Matthiesen, A. Vamivakas, and M. Atatüre, “Subnatural Linewidth Single Photons from a Quantum Dot,” *Phys. Rev. Lett.*, vol. 108, no. 9, pp. 1–4, Feb. 2012.

[18] L. Hofstetter, A. Baumgartner, and S. Csonka, “Wet etch methods for InAs nanowire patterning and self-aligned electrical contacts,” pp. 1–9.

[19] P. Gallo, M. Felici, B. Dwir, K. Atlasov, K. F. Karlsson, A. Rudra, A. Mohan, G. Biasiol, L. Sorba, and E. Kapon, “Integration of site-controlled pyramidal quantum dots and photonic crystal membrane cavities,” *2008 Conf. Quantum*

Electron. Laser Sci. Conf. Lasers Electro-Optics, CLEO/QELS, vol. 263101, no. 2008, pp. 1–4, 2008.

[20] L. O. Mereni, V. Dimastrodonato, R. J. Young, and E. Pelucchi, "A site-controlled quantum dot system offering both high uniformity and spectral purity," *Appl. Phys. Lett.*, vol. 94, no. 22, pp. 10–13, 2009.

[21] C. Schneider, A. Huggenberger, M. Gschrey, P. Gold, S. Rodt, A. Forchel, S. Reitzenstein, S. Hofling, and M. Kamp, "In(Ga)As/GaAs site-controlled quantum dots with tailored morphology and high optical quality," *Phys. Status Solidi Appl. Mater. Sci.*, vol. 209, no. 12, pp. 2379–2386, 2012.

[22] J. Herranz, L. Wewior, B. Alén, D. Fuster, L. González, and Y. González, "Role of re-growth interface preparation process for spectral line-width reduction of single InAs site-controlled quantum dots.," *Nanotechnology*, vol. 26, no. 19, p. 195301, 2015.

[23] A. Dousse, L. Lanco, J. Suffczynski, E. Semenova, A. Miard, A. Lemaitre, I. Sagnes, C. Roblin, J. Bloch, and P. Senellart, "Controlled light-matter coupling for a single quantum dot embedded in a pillar microcavity using far-field optical lithography," *Phys. Rev. Lett.*, vol. 101, no. 26, p. 267404, Dec. 2008.

[24] C. Bentham, I. E. Itskevich, R. J. Coles, B. Royall, E. Clarke, J. O'Hara, N. Prtljaga, A. M. Fox, M. S. Skolnick, and L. R. Wilson, "On-chip electrically controlled routing of photons from a single quantum dot," *Appl. Phys. Lett.*, vol. 106, no. 22, p. 221101, 2015.

[25] K. Hennessy, A. Badolato, A. Tamboli, P. M. Petroff, E. H. Atatüre, J. Dreiser, A. Imamoğlu, K. Hennessy, A. Badolato, A. Tamboli, P. M. Petroff, and E. Hu, "Tuning photonic crystal nanocavity modes by wet chemical digital etching Tuning photonic crystal nanocavity modes by wet chemical digital etching," vol. 21108, pp. 1–4, 2005.

[26] K. H. Lee, F. S. F. Brossard, M. Hadjipanayi, X. Xu, F. Waldermann, A M. Green, D. N. Sharp, A J. Turberfield, D. A Williams, and R. A Taylor, "Towards registered single quantum dot photonic devices.," *Nanotechnology*, vol. 19, no. 45, p. 455307, Nov. 2008.

[27] P. B. Deotare, I. Bulu, I. W. Frank, Q. Quan, Y. Zhang, R. Ilic, and M. Loncar, “All optical reconfiguration of optomechanical filters,” *Nat. Commun.*, vol. 3, no. May, p. 846, 2012.

[28] L. I. Berger, *Semiconductor materials*. CRC Press, 1997.

[29] G. Bosshart, “Cubic Stabilized Zirconias,” *Schweizerisches Gemmol.*, vol. XVI, no. 4, pp. 244–256, 1978.

[30] M. E. Broz, R. F. Cook, and D. L. Whitney, “Microhardness, toughness, and modulus of Mohs scale minerals,” *Am. Mineral.*, vol. 91, no. 1, pp. 135–142, 2006.

[31] D. L. Wood and K. Nassau, “Refractive index of cubic zirconia stabilized with yttria,” *Appl. Opt.*, vol. 21, no. 16, p. 2978, Aug. 1982.

4. Deterministic Fabrication With Registered Quantum Dots

4.1. Introduction

In the previous chapter, it was demonstrated that the uncertainty in the relative position of a quantum dot via dot registration could be significantly reduced by more than a factor of 5 at best using a solid immersion lens. Whilst significant care was taken during the steps required to register the position of a quantum dot, compounded systematic errors will undoubtedly be present and carried forward. Although the accuracies quoted for the registration process provide an indication of the techniques accuracy, it is impossible to state how precisely a structure can be fabricated around a quantum dot using this value alone. This is considered to be the case regardless of whether a solid immersion lens is used or not, and therefore, independent confirmation of the overall deterministic fabrication accuracy is required.

In this chapter, the precision of the EBL which is fundamental for registration purposes is investigated to provide an estimate of systematic errors which may be introduced. A quasi-independent method of confirming the registration accuracy is then used by deterministically fabricating supplementary registration markers at pre-determined distances away from the registered quantum dot location. The quantum dot location is then re-registered relative to the new markers in order to provide the total error of deterministic fabrication.

Additionally, the properties of quantum dots during the registration process are closely monitored before and after being deterministically positioned within a nanobeam waveguide. Using the physical properties of the modal structure of the nanobeam waveguides, an additional, entirely independent, measurement of the total error in deterministic fabrication is calculated.

4.2. EBL Precision

Lithographic fabrication processes, prior to dot registration, are considered to be the dominant cause of systematic errors. Any variance in the relative positions between registration markers, which are used to measure the relative position of the quantum dot, as well as calibrating the magnification of the SIL, will induce errors in all subsequent steps. Additionally, similar fabrication errors of the re-alignment markers used by the EBL to realign the writing field prior to additional fabrication processes will also result in systematic errors. Therefore, in this section, the stability and accuracy of the EBL is investigated to determine at what precision sequential fabrication processes could be performed.

4.2.1. Sources of Error

Precise and reproducible fabrication using electron beam lithography is highly sensitive to a range of parameters. Initial steps prior to patterning a sample typically focus on ensuring the alignment of the electron beam is aberration and stigmation free. This process uses a series of short but intense exposures to pattern small dots on the samples surface. Despite not being able to develop the resist within the EBL to see the shape of the exposed dots, small amounts of contaminants present in the vacuum bind to the surface and provide sufficient contrast. Through iterative adjustments to the electromagnetic lenses, and position of the sample stage, it is possible to ensure the electron beam produces spherical contamination spots with a near optimal focus.

Whilst it is important to optimise parameters such as the beam shape to ensure high quality, reproducible fabrication steps, the errors introduced for dot registration purposes will be minimal. Rather, precise alignment of the electron beam co-ordinate system to that of the desired patterns on the sample represents a direct source of error.

Due to the finite resolution of the analogue to digital converter used to deflect the electron beam, allowing the exposed location on the samples surface to be adjusted, the smallest supported fabrication grid, 2500 μm^2 in size (50 μm by 50 μm), is used. In order to calibrate and align the electron beam to a specific grid, referred to as a 'write field', an automatic 'write field alignment' procedure is used. During initial wafer fabrication, where no pre-existing structures are present on the samples surface, contamination spots as previously described are used as a reference point. Using an interferometer, the position of the sample stage is moved a known distance away from the contamination

spot, varying on scales of tens of micrometres to hundreds of nanometres. Using image recognition software, the electron beam is deflected in an attempt to locate the identifying marker (contamination spot) at the reference point, and from which, the required deflection of the electron beam can be calibrated. Where pre-fabricated structures are already present, the technique is modified slightly as will be discussed later.

During write field alignment, several apparent sources of error are identified which may introduce systematic errors in the registration process. These may include effects such as sample drift or the finite resolution of the system used to determine the calibration. As such, the deflection of the electron beam may be distorted from that which is actually desired, resulting in the relative distance between the fabricated registration markers being wrong. As these markers are needed to calibrate the magnification observed through the solid immersion lens, as well as act as a reference point from which the position of a quantum dot can be registered, even a small error may be compounded such that it is significant. An example of the fabrication error which may occur as a result of this is shown in Figure 4-1.

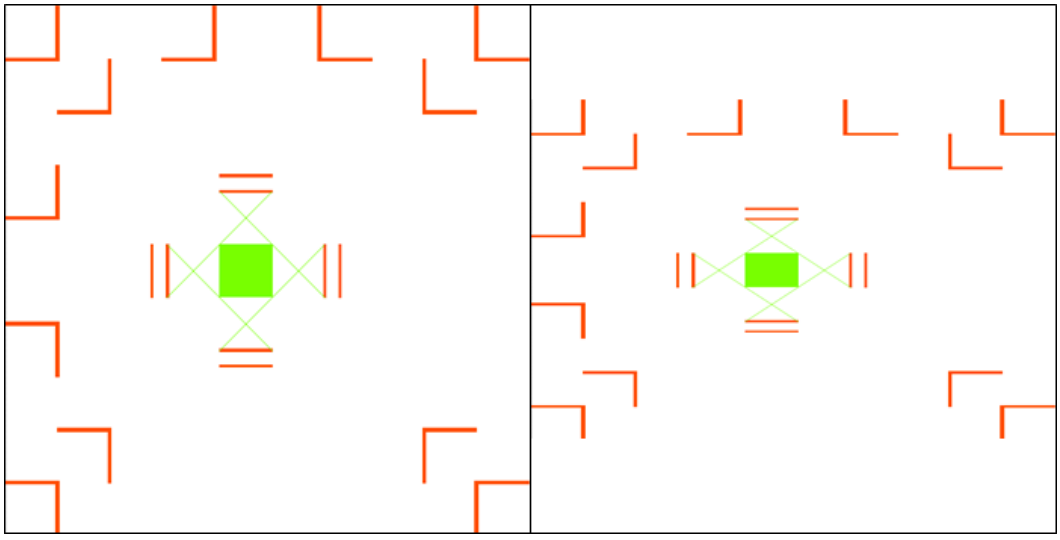

Figure 4-1 – Schematic depicting 'stretching' errors which may occur as a result of improper calibration in the deflection of the electron beam. (Left) Ideal desired pattern to be written by the EBL. (Right) Exaggerated resulting pattern if the calibration of the vertical axis is set incorrectly, resulting in the true marker spacing to be different from the desired value.

Additionally, by aligning the write field at a specific point on the sample, it is assumed that correct alignment will be maintained across the entirety of the sample. It is obvious however that if the sample is rotated with respect to the exposure plane, as shown in Figure 4-2, that not only will the initial calibration be incorrect, but each additional write

field will be distorted with respect to the every other write field. Structures fabricated on samples mounted at a significant angle to the exposure plane will therefore suffer from varying sizes, aspect ratios as well as stitching artefacts where proximity error correction is used.

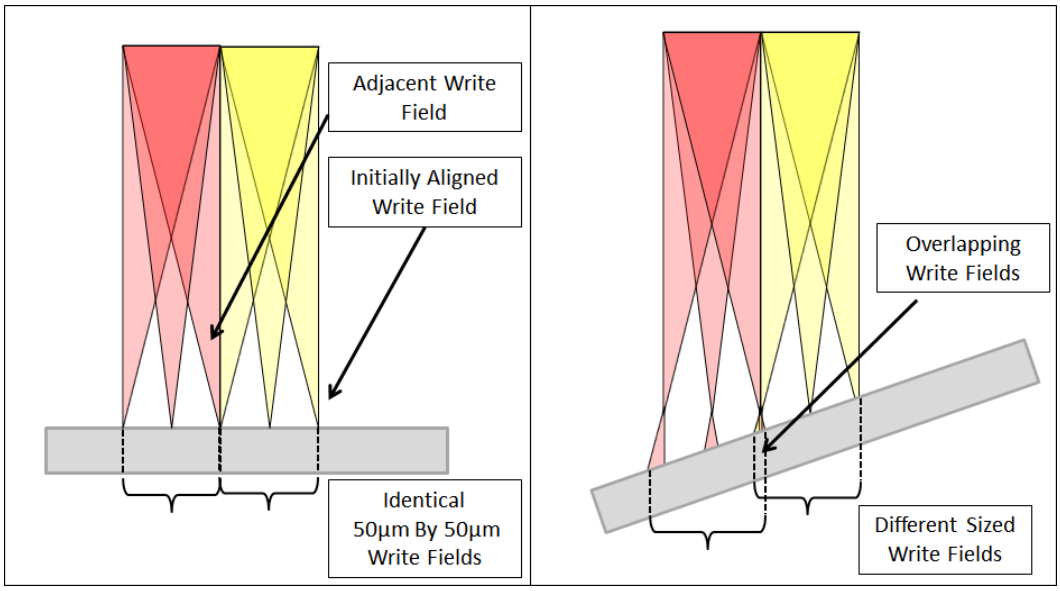

Figure 4-2 – Schematic showing how rotation of the sample with respect to the exposure plane of the EBL results in both local and relative changes in the desired pattern. (Left) shows a sample correctly aligned to the exposure plane resulting in uniform exposure. (Right) sample rotated with respect to the exposure plane with features exposed at varying sizes within the same write field.

Fortunately, sample misalignment which would cause an unwanted angle to the exposure plane is easily identified during initial fabrication steps through the use of contamination spots. Typically, contamination spots are created near the centre of the wafer, taking care to ensure they do not interfere with the desired fabrication steps. By creating additional contamination spots at the periphery of the sample wafer, it is possible to check if suitable alignment is maintained, and if not, appropriate steps to correct the angle can be taken prior to fabrication.

In contrast, the other types of error described are inherent to the operation of the EBL, and as such, very little can be done to minimise their impact. As a first step towards quantifying the precision and reproducibility of the EBL, the accuracy of the write field alignment procedure is measured. In order to provide sufficient contrast for numerous repeated scans, contamination spots will not be used as a reference point. The reason for this is that each successive scan will alter the shape of the surface contaminant which will bias results. Instead, pre-fabricated markers are used, as would be typical during post

registration fabrication steps, to re-align the write field to that of one used during initial marker fabrication. Unlike the write field alignment using contamination spots, a total of six independent discrete features are required to correctly calibrate position, magnification and rotation for both the horizontal and the vertical axis (three each).

By continuously performing the write field alignment to the same set of horizontal and vertical markers, and recording the calculated displacement of the sample, it is possible to identify if continual sample drift or random noise due to limitations in the measurement technique warrant further concern. Results of the alignment procedure are presented in Figure 4-3 as a function of time. As the time taken to perform a single line scan is negligible, a delay is used between each line scan of approximately 1 minute in order to determine the stability of the sample over long time scales, as may be required to fabricate large arrays of registration markers. Furthermore, to ensure the measurement processes does not itself induce or mask additional sources of error, an extended break is introduced between two alignments scans of 7 minutes.

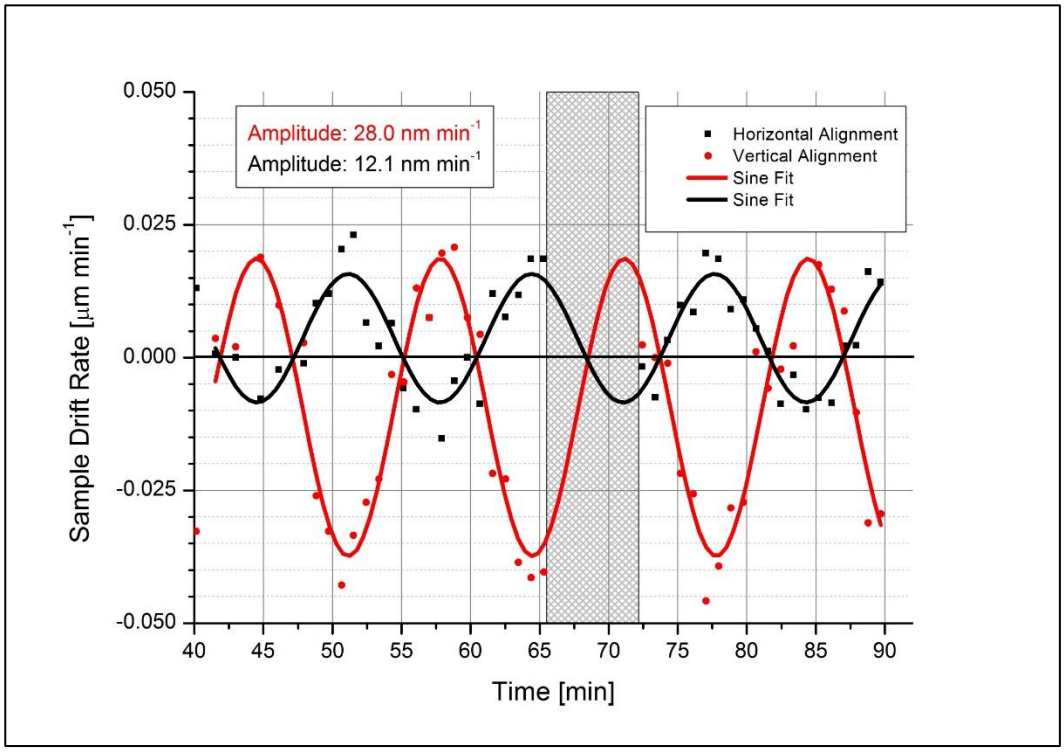

Figure 4-3 –Drift rate of the EBL calculated from the relative change in the positioned of the re-alignment markers. Both the vertical (red) and horizontal (black) direction appear to oscillate sinusoidally with a constant phase. The extended break between measurements is shown by the hashed lines at approximately 25 minutes.

A clear periodic sinusoidal trend exists in the drift rate for both the horizontal and vertical axis, approximately centred on about a zero drift rate. The periodic nature of the drift infers the influence of a perturbation, with a time period of

13.29 ± 0.01 minutes. As the phase of the sinusoidal trend is unchanged after the extended pause between alignment scans, it is unlikely that the measurements have any influence on the observed drift rates. Typically, oscillations of this nature are common in instruments which use proportional, integral and differential (P-I-D) parameters to control a system variable. Specifically, poor optimisation of the differential parameter will result in a driven oscillation about a target value.

For the Raith150 EBL system used, the sample stage is actively cooled using an external temperature controller. Under further inspection, it was found that temperatures were oscillating around the desired temperature with a time period corresponding to the sample drift rate in Figure 4-3. The observed sample drift is therefore likely due to thermal expansion and contraction of mechanical components. Optimised control settings were used to reduce temperature variations during sample exposures, and the system stability is tested again by repeating write field alignment scans.

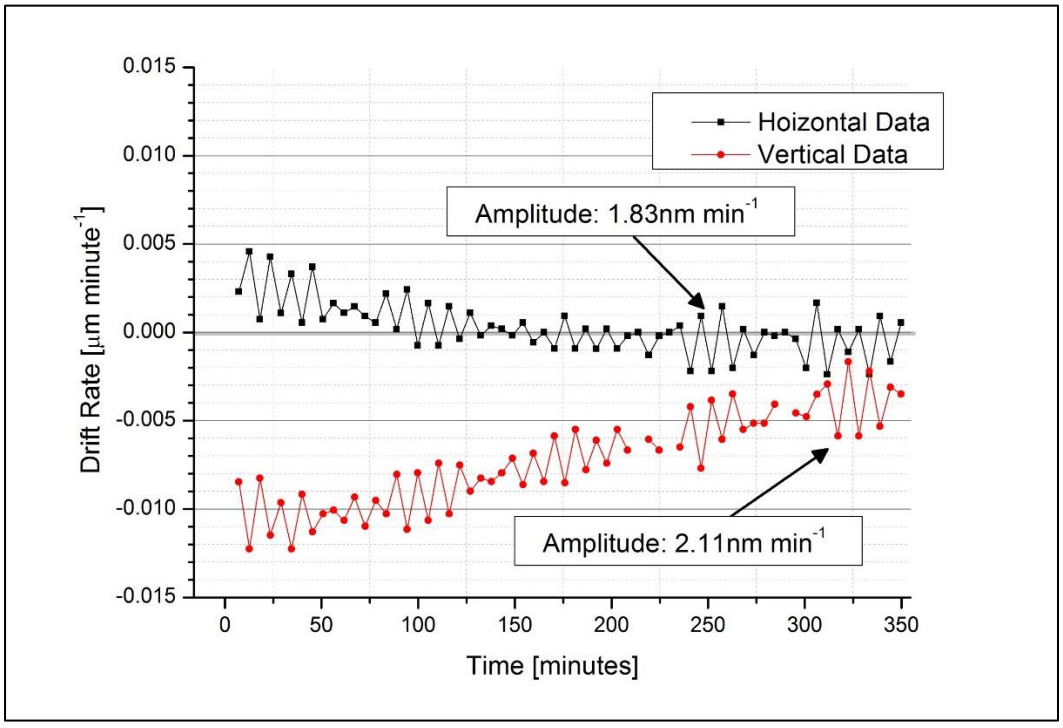

Figure 4-4 – Drift rate of the EBL as measured in Figure 4-3 with optimised thermal control parameters. The sinusoidal nature of the oscillations on long time scales is removed, revealing high frequency fluctuations.

The measured drift rates shown in Figure 4-4 show a significant reduction compared to previous values reported, with a general trend towards a drift rate of zero at long time scales. It is unclear whether the beating that is now present is due to the changes to the settings of the temperature controller, or if by removing the driven

oscillation, the beating signal is simply more visible. As the maximum amplitude of the high frequency oscillation is 2.11 nm min^{-1}, with the total drift rate tending towards zero at long time scales, this error is not considered significant. Furthermore, as the drift rate is expected to be centred on zero, the net drift averaged over long time periods will also be zero. The maximum expected error for a photonic structure, which typically takes one minute to expose the desired pattern, will be less than 2.78 nm if sufficient time is allowed to pass between loading the sample and exposure.

To confirm the fabrication accuracy of the EBL, a series of horizontal and vertical markers are etched into the GaAs membrane as shown in Figure 4-5. The sample is then re-loaded into the EBL and identical copies of the horizontal and vertical markers are patterned directly to the side and below the original markers. High resolution SEM images are taken so that the position of each marker can be compared with its corresponding displaced marker.

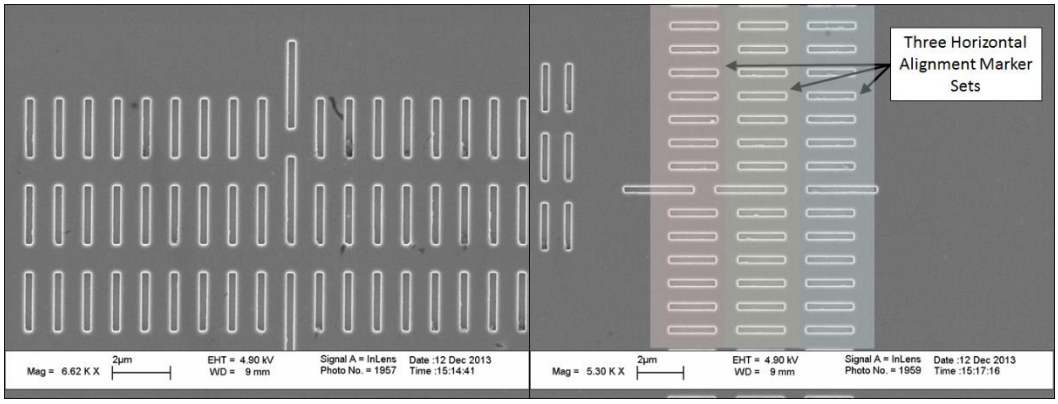

Figure 4-5 – SEM imageries Showing markers used to confirm the positional accuracy in which deterministic fabrication can be performed, relative to an existing set of fabricated markers. Three sets of vertical (left) and horizontal (right) alignment markers are shown in each SEM image, with a single set fabricated in the initial fabrication.

As the width of each marker may vary due to fluctuations from a variety of parameters during fabrication, such as the dose used to expose the electron beam resist or the etchant rate of the ICP, the central position of each marker is used to calculate the relative displacement. It is assumed here that any broadening of the markers will be symmetrical about the centre, and therefore the fitting procedure used to calculate the centre will be unbiased. It is noted that the reason for not including any error due to broadening of markers is that it is solely the error due to re-alignment of the EBL that is unique to the dot registration process. As such, the broadening of features fabricated by EBL will not have any significant effect on the registration accuracy, but rather, only the performance of photonic structures with critical dimensions. A graph depicting the

method used to calculate the centre of each marker is shown in Figure 4-6, where a Gaussian fit is performed to the exponentially increasing contrast surrounding the etched region.

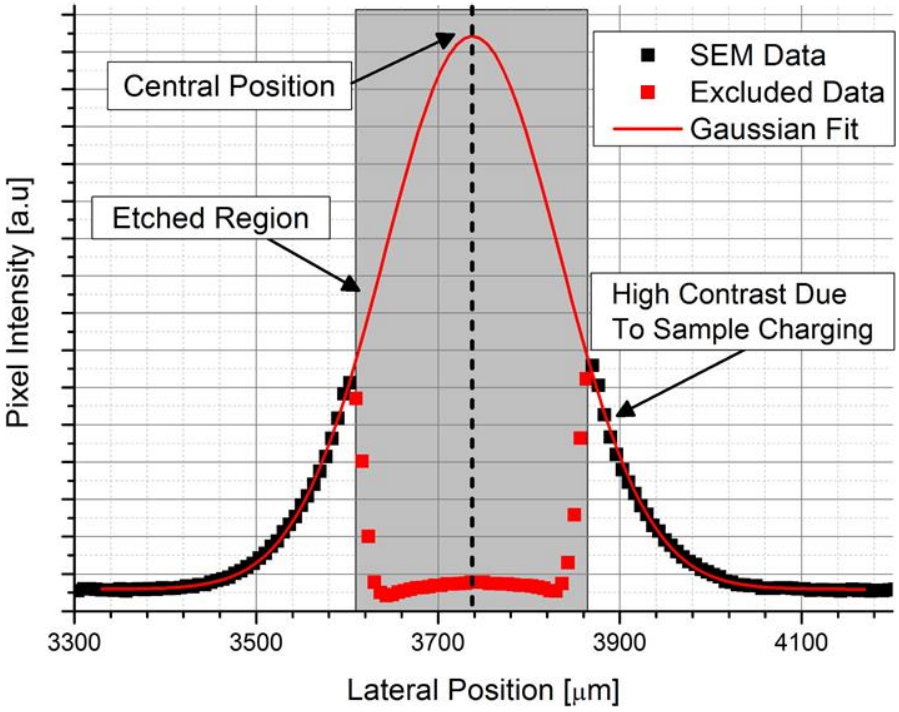

Figure 4-6 – line section through individual etched marker from an SEM image, as shown in Figure 4-5. Gaussian fit (red line) is fit to pixel intensities (back) which show an exponential increasing contrast near the etched markers due to localised charging. Data from the etched region (red) is excluded from the fit.

Using Gaussian fits to calculate the central position of several markers, and using a reference point on an image, such as the image edge, the relative displacement between marker sets is calculated. As several sources of errors are considered to affect the EBL, each with unique probability distributions, by examining histograms of the calculated relative displacements between markers, it is possible to identify if any individual source of error is significant. A comparison of probability distributions for various sources of error (sinusoidal, uniform and random) to that measured for the marker displacement is shown in Figure 4-7.

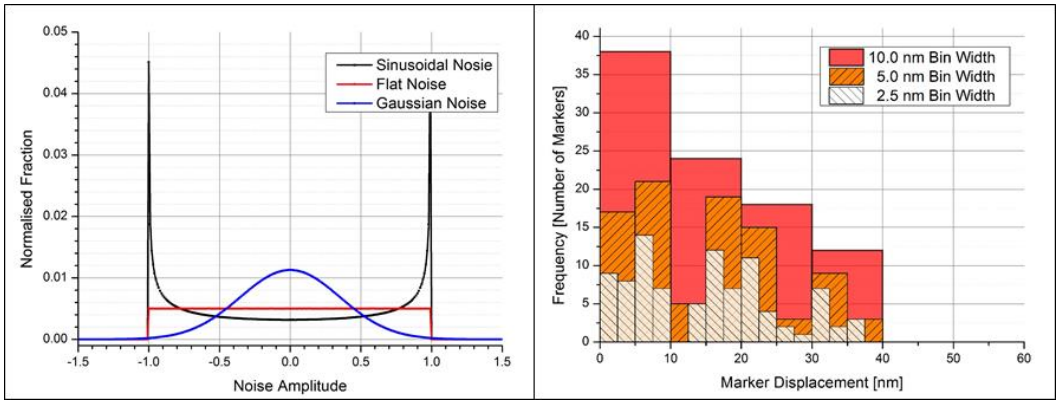

Figure 4-7 – (Left) Probability distribution functions for three common sources of error thought to affect deterministic fabrication of electron beam lithography. (Right) Histogram for various bin resolutions for the calculated absolute displacement between sequential deterministically positioned markers.

A range of bin widths have been considered for the measured marker displacement in order to resolve sharp features which may exist due to sinusoidal perturbations of the fabrication. It is concluded from the shape of the measured distribution that random noise, with a Gaussian profile, is primarily responsible for the displacements seen. Although the displacement is centred on zero, the large spread in measured values will likely be the limiting factor in deterministic fabrication. A mean of 15.10 nm is calculated for the absolute value of displacement which is comparable to the FWHM achieved during the optical dot registration process. Unlike dot registration however, where multiple iterations of a scan can be performed to reduce the error in the dots location, errors which occur during fabrication are absolute. Errors due to re-alignment of the EBL are therefore considered to be dominant over errors reported for solid immersion lens enhanced registration.

4.2.2. Quantum Dot Re-Registration

So far, errors have been calculated for the dot registration (see chapter 3), as well as the EBL, in an attempt to characterise the total error of deterministic fabrication. Unfortunately, this method alone cannot account for systematic sources of error which may result in a constant shift of the measured variable. A series of sacrificial quantum dots are therefore registered, with the proposal of fabricating additional registration markers a pre-determined distance away. By repeating the registration process relative to these markers, any measured difference between the expected marker separations to the measured marker separation will provide insight as to the total error of the registration process. This method is not entirely unbiased, as unless sources of systematic error are the result of an initial error which is random in direction and magnitude, the re-

registration of quantum dots will also be subject to the same systematic error. A specific example may be that of the drift rate of the cryostat relative to the scanning stage. Provided the direction and magnitude of the drift are random, then when re-registering the position of a quantum dot, an entirely different systematic error will be introduced. However, if the direction and magnitude remain constant between scans, then the position registered will report better agreement than it should. Whilst this does mean that re-registering the position of the quantum dot does not represent an entirely independent verification, it is considered to be sufficiently reliable to draw meaningful conclusions from.

To ensure no biasing is introduced in the re-registration of the quantum dots, only the newly fabricated re-registration markers are used to calibrate the magnification and the new position of the quantum dot. In order to confirm the identity of the registered quantum dot prior to re-registering its position, the approximate location of the quantum dot is scanned over, and the spectrum is recorded. Using a reference spectrum taken prior to the fabrication of the re-registration markers, the relative and absolute energies of quantum dot transitions are compared. Figure 4-8 presents a quantum dot identified for re-registration where power dependence has been performed to distinguish the neutral and changed exciton from the bi-excitonic states.

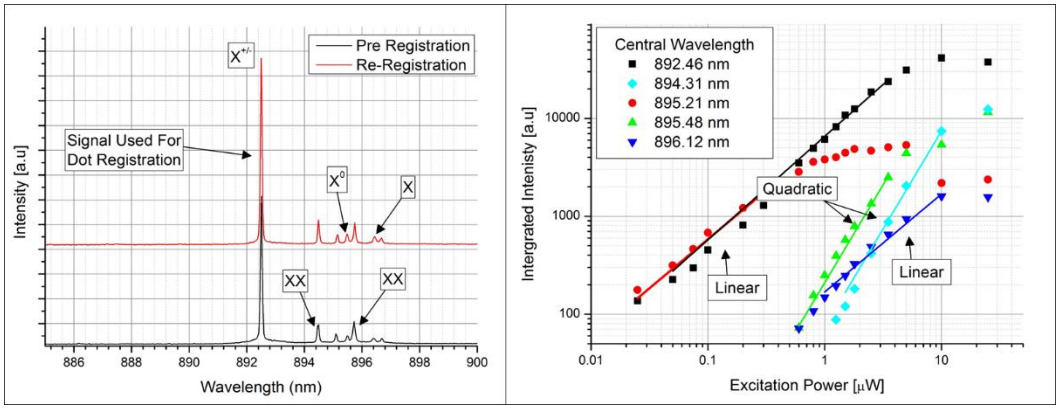

Figure 4-8 – (left) Spectral comparison of quantum dot taken prior to initial registration of its position (black) and after re-registration markers have been fabricated (red). (Right) Power dependence of observed photoluminescence used to distinguish neutral and charged excitonic states from bi-excitons ones.

Of the quantum dots which were identified during dot registration, and successfully had their positions re-registered, the minimum deviation between the expected distance between the quantum dot and the newly fabricated re-registration marker was calculated to be 13.7 nm. A histogram comparing the initial registered position to that calculated from the re-registration markers based on 100 repeated line scans is shown in

Figure 4-9. In contrast, the maximum difference between the desired separation between a quantum dot and the deterministically positioned re-registration marker was found to be 34.9 nm. Although these errors are significantly higher than the calculated error in the registered position, a review of contributing factors shows that these errors observed are representative of the system used, and are dominated by errors introduced by the EBL.

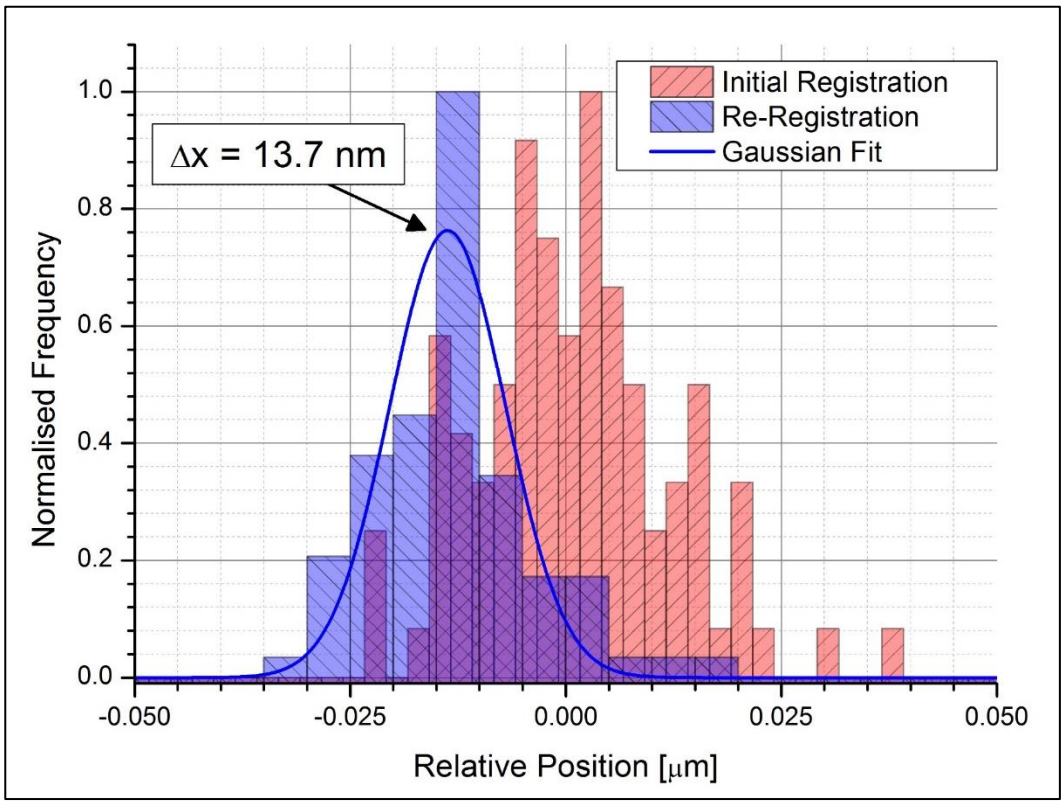

Figure 4-9 – Histograms showing the relative positions of quantum dots during registration processes. The distribution of positions measured during the initial registration (red) are compared to the positions measured relative to the re-registration markers (blue).

The successful demonstration of being able to deterministically fabricate a structure around a quantum dot with an offset of only 13.7 nm therefore represents a significant achievement towards realising scalable photonic structures. Considering this precision is comparable to the lateral size of the quantum dot, demonstration of optimal coupling of multiple quantum dots within a single photonic structure should be achievable.

4.3. Nanobeam Waveguides

In this section, dot registration and deterministic fabrication of suspended nano-beam waveguides are used to investigate the properties of quantum dots pre and post fabrication, hoping to identify and quantify any detrimental effects observed as a result of the fabrication. Additionally, the successful deterministic fabrication of a nanobeam

waveguide around a quantum will provide additional confirmation as to the accuracy of dot registration.

4.3.1. Bulk Characterisation

The nano-beam waveguide has been designed to act as circuitry to transport flying-qubits for quantum information processing. For efficient coupling, the exciton transition and the supported nanobeam waveguide mode should be both spatially and energetically matched. It is shown through FDTD simulations that the spectral bandwidth of the fundamental waveguide mode is large (> 10 nm) compared to the exciton linewidth of the quantum dot (<0.1 nm). Therefore, for a suitably located quantum dot, it is not expected that the quantum dot should exhibit a Purcell enhancement. In addition to this, as the primary purpose of the waveguide is to act as photonic circuity, it is desirable that by embedding the quantum dot in a waveguide, its emission properties are not adversely affected.

In order to quantitatively analyse any changes to the intrinsic properties of the quantum dot prior to the deterministic fabrication, optimal quantum dots were selected based their observed spectral line widths and relative spatial and spectral proximity to additional quantum dots or spectral features. Once a quantum dot is selected, it is extensively characterised with the following key attributes measured; optically active excitonic states, power dependence, fine structure splitting, lifetime (τ_1) and the coherence time (τ_2). Details regarding the experimental setup are provided in the experimental methods section (see chapter 2).

Spectral Features & Power Dependence

Several quantum dots which exhibit narrow, well isolated spectrum with readily identifiable charged states are selected for dot registration, such as that shown in Figure 4-10. Should the relative intensity, abundance or energy of any of the spectral features change as a result of the fabrication, then further investigation regarding the cause will be required in order for dot registration to maintain a viable technique.

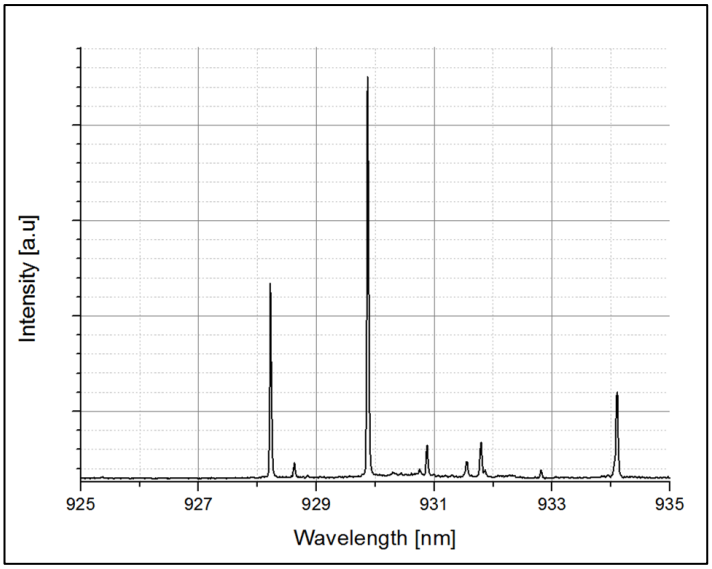

Figure 4-10 – Typical spectra at near saturation powers for a single quantum dot selected for dot registration. Multiple excitonic transitions are visible indicating the presence of numerous charged states.

It is observed during characterisation of samples that often numerous charged states are present for single quantum dots, likely indicating the presence of a structural defect nearbly, which readily acts as a donor or accepter of electrons and holes [1]. For InGaAs quantum dots in a GaAs matrix, the capture of electrons from the GaAs matrix and the wetting layer to the quantum dot is typically efficient due to the presence of multiple relaxation processes (such as Auger scattering, Phonon emission) [2]. As a result, the quantum dot, which is typically 10's of nm in size (laterally), is coupled to local continuum of states via the wetting layer which extends significantly beyond the quantum dot. Due to this, sensitivity to the extended environment surrounding the quantum dot, even with a relatively low defect density, can significantly affect the charge dynamics of the quantum dot.

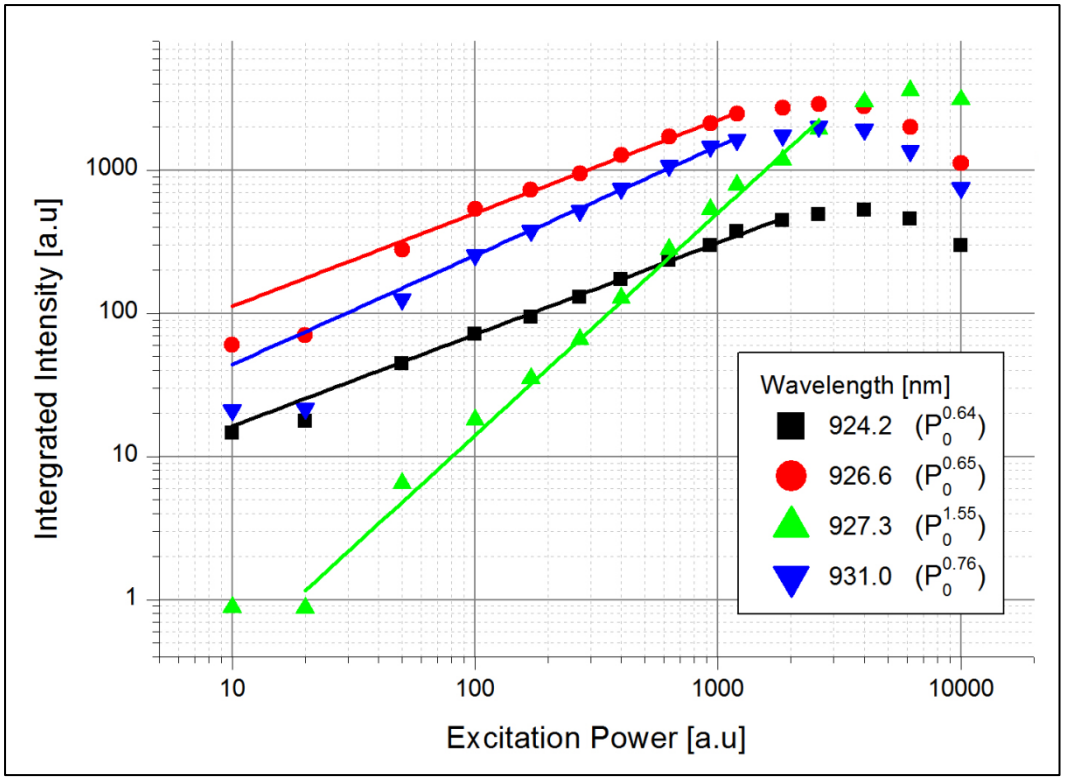

Figure 4-11 – Power dependencies of individual exciton transitions measured for a quantum dot chosen for dot registration.

Power dependence is used to provide information regarding the relative intensities of spectral peaks, as well as to distinguish charged and neutral excitons (X*) from bi-exciton states (XX). For the neutral and charged exciton, it is expected that the integrated signal intensity should vary linearly with excitation power, however, as the bi-exciton and charged bi-excitons intensity is proportional to both the excited carrier density and the probability of a neutral or charged exciton already being excited, a quadratic power dependence is expected [3].

Whilst these linear and quadratic power dependencies provide information which allows the identification of spectral features, it also provides insight regarding carrier dynamics in the vicinity of the quantum dot. As such, any deviation from the expected linear or quadratic relationship likely indicates the presence of local defects which result in non-radiative decay. Additionally, where multiple charged states are observed, a surplus of charge carriers may also result in a non-linear power dependence due to the multiple excitation and relaxation pathways supported [4].

The power dependencies of quantum dots chosen for dot registration reveal predominantly sub and super linear relationships with excitation power, with few

spectral lines following a linear or quadratic relationship, as presented in Figure 4-11. As discussed above, this likely indicates defects contained within the sample, where sub linear power dependencies indicate non radiative decay processes, which in turn result in a higher carrier population which facilitates super linear power dependencies for other excitonic states. By recording these power dependencies prior to the fabrication of any photonic structure, any deviation observed must be as a result of one or more of the subsequent fabrication processes.

Fine Structure Splitting

The maximum spectral resolution of the 75 cm focal length spectrometer used, as described in chapter 2, is approximately 30 μeV. This is comparable to the expected fine structure splitting of asymmetrical quantum dots, and it is therefore not be possible to resolve individual peaks. However, as only the presence of the splitting is of interest, it is not necessary to fully resolve the two peaks. A good approximation of the splitting can be therefore obtained by fitting a Gaussian peak to the observed spectra when measured as a function of polarisation, as shown in Figure 4-12. If the measurement basis is aligned to either the major or minor axis of the quantum dot asymmetry, then the recorded spectrum will be entirely due to a single fine structure transition. As this method is sensitive to relative intensity changes in the measured spectrum, polarisation dependence of optical elements is carefully removed by placing a half-wave plate followed by a linear polariser in the collection path. Measurements are taken for incremental rotations of the half waveplate, with the rotation axis of the linear polariser fixed.

For the quantum dots chosen for dot registration, analysis of the fine structure splitting present within the observed spectrums confirms the presence of neutral and bi-exciton transitions. Similarly, charged excitons are identified through the absence of any fine structure splitting. Surprisingly, due to the high resolution of the solid immersion lens and relatively low quantum dot density, estimated to be $\sim 10^8$ QD's cm^{-2}, multiple neutral exciton lines are also identified in a small number of the observed spectra. Although clustered growth of quantum dots is not uncommon, it is typically explained by an increased anisotropic flux of group III adatoms within the MBE chamber which exhibit a supressed diffusion length [5]. Under these conditions, it would be expected that 'chains' of quantum would form. The possibility of surface roughening or sputtering of metal defects cannot however be discounted.

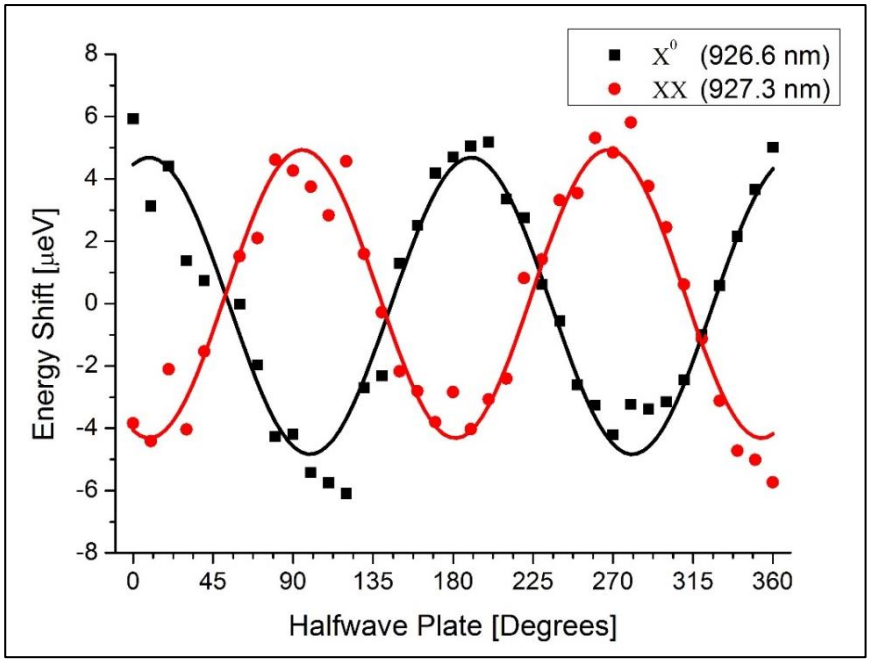

Figure 4-12: Measurement of the fine structure splitting for a registered quantum dot via a least squared fit to determine the central wavelength of polarisation dependant spectrum. A sinusoidal fit for the neutral (black) and bi-exciton (red) transition show they out of phase by a factor of π as predicted by conservation of spin. The fine structure splitting is calculated to be 9.44 μeV and 9.48 μeV for the neutral and bi-exciton transition respectively.

The presence of multiple neutral exciton states in a single spectrum will likely hinder the identification of charged excitons, and may also increases the sensitivity of neighbouring quantum dots to changes in its local environment. Therefore, should any spectral changes be observed due to the fabrication of a single mode photonic waveguide, it is probable that these affects will be exaggerated where multiple excitons are present.

Lifetime

Measurements of the lifetime of the quantum dots are performed as described in chapter 2, using a 80 MHz repetition rate, 100 fs pulse width, Ti:Si laser tuned into resonance with the wetting layer. As excited carriers in the wetting layer experience an increased local density of states with respect to quantum dots, carrier relaxation occurs significantly quicker as interactions via LO and LA phonon scattering is allowed. Typical relaxation rates for the bulk GaAs and wetting layer are therefore of the order of 10's of ps, significantly shorter than typical lifetimes of excitons in quantum dots [6]. Under pulsed excitation, it can be safely assumed that after ~ 100 ps, that carriers in the wetting layer or bulk GaAs have all but completely relaxed or been captured by a QD. Photoluminescence which occurs after these time scales is therefore the result of the recombination of an electron and hole which have been captured by a quantum dot and formed an exciton.

The lifetimes of several neutral and charged excitonic states have been measured for the quantum dots selected for dot registration, with two examples shown in Figure 4-13. Of the dots selected for dot registration, no deviation from the expected single exponential decay was observed and the calculated lifetimes agree well with reported values for other InGaAs quantum dots [7]. As the quantum dots are embedded within the bulk semiconductor, variations in the measured lifetimes are attributed to size fluctuations in the quantum dots, altering the confinement of the electron and hole wavefunctions and therefore the strength of the dipole interactions. The absence of any bi-exponential decay is taken as promising as its presence would indicate the presence of detrimental interactions of the quantum dot with the solid state environment [1][8][9].

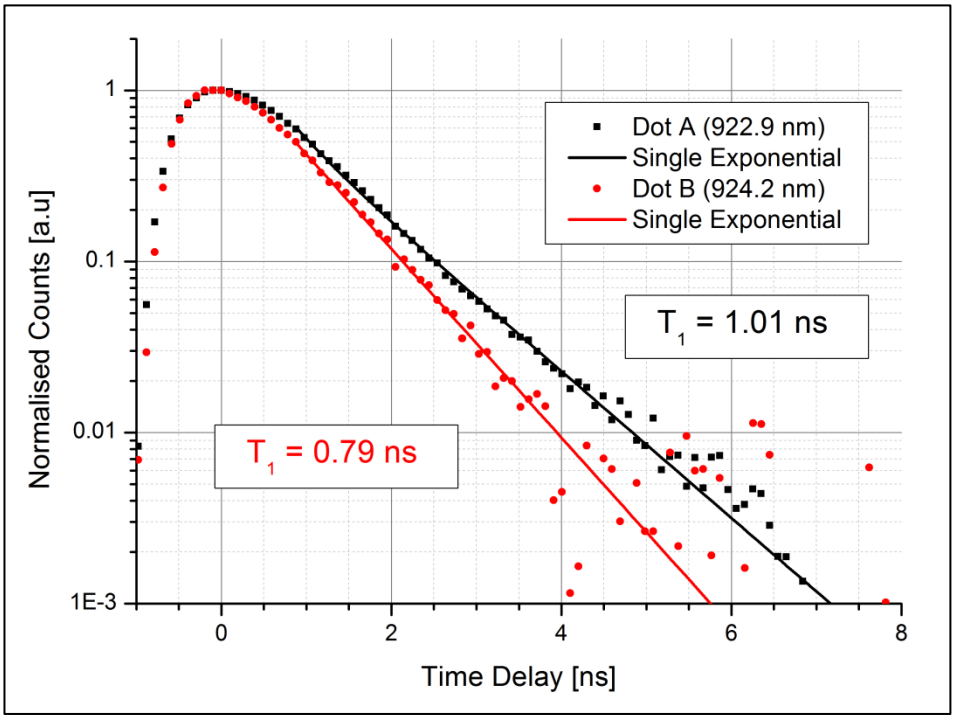

Figure 4-13 – Lifetime measurements for two different excitionic transitions observed in the bulk GaAs prior to registering the position of a quantum dot. Lifetime measurements agree well with typical values reported in the literature and show single exponential decays.

Coherence Time

The strength of the quantum dots interaction with its solid state environment is well captured by the coherence time. Direct measurements of the coherence time are performed using the Michelson Interferometer as described in Chapter 2 under continuous wave excitation. In order to reduce the significance of power broadening, excitation powers which result in intensities half of that of the saturation value are used.

As measurements were performed in a flow cryostat, low power measurements which would require extensive signal integration times are not feasible.

Spectral filtering is performed using the spectrometer, collecting the signal via a second beam path. A micrometre controlled slit is used to select the spectral bandwidth, which in order to remove diffraction and maintain optimal coupling into a single mode fibre is set to a width which corresponds to a bandwidth of approximately 0.5 nm. It is shown in Figure 4-14 that as a result of the broad bandwidth with respect to the exciton linewidth, the measured signal is expected to contain an incoherent background signal making up to approximately 10 % of the total intensity.

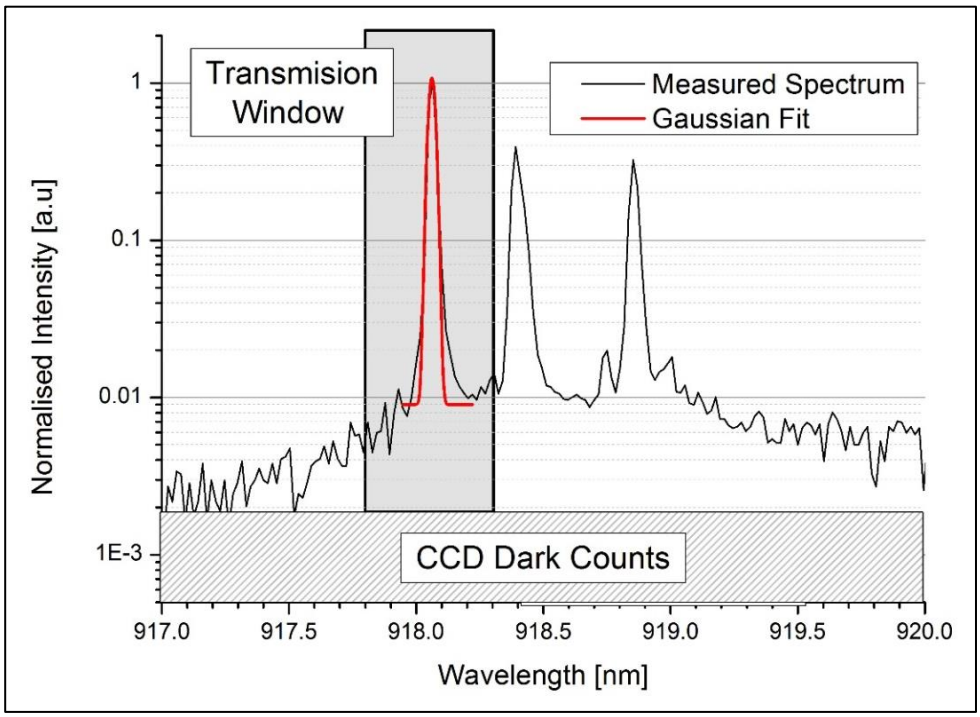

Figure 4-14: Normalised spectrum showing broad background present surrounding single quantum dot transitions. Due to the 0.5 nm spectral width of the spectrometer used to filter the photoluminescence, the transmitted signal is expected to contain incoherent emission with an intensity of ~ 10 % of total intensity.

The measured coherence time for the quantum dots registered, such as those shown in Figure 4-15, show general agreement with coherence times measured for InGaAs quantum dots located near the surface in bulk semiconductor [10][11]. They are however significantly lower than the coherence times observed for quantum dots far from the surface, which can be in excess of 500 ps [12][13]. Whilst the low coherence time of 158.8 ps for 'dot D' (see Figure 4-15) is representative of near surface quantum dots, the 46.1

ps coherence time for 'dot A' (see Figure 4-15) likely indicates a particularly unstable environment around the quantum dot. The average coherence time for all the exciton transitions which were measured is calculated to be 93.3 ps. Additionally, significant variance is observed in the coherence times of individual exciton transitions of the same quantum dot.

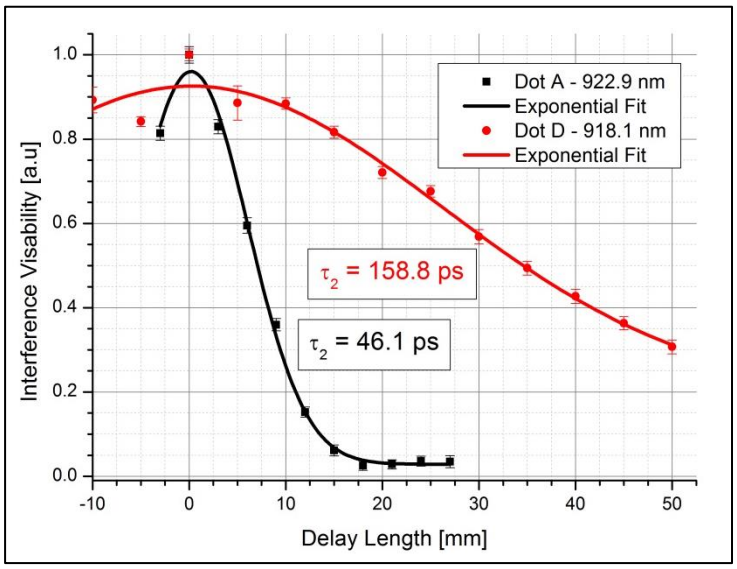

Figure 4-15: Michelson Interferometer Measurements of the coherence time for excitionic transitions of two separate quantum dots prior to dot registration. Both coherence times are significantly shorted than the flourier transform limited coherence ($\tau_2 = 2\tau_1$).

4.3.2. Waveguide Characterisation

As with the fabrication of additional markers for re-registration, the registered position of the quantum dots is used to fabricate a nanobeam waveguide with a quantum dot located at the centre. The width of the fabricated waveguide is chosen such that it supports the fundamental transverse electric modes (see chapter 1). A width of 280 nm has been calculated using finite difference in time domain simulations to support typical InGaAs quantum dot wavelengths with a minimum evanescent component. In order to compensate for proximity effects of the EBL as well as lateral etching of the hydrofluoric acid and ICP (see chapter 2), a fabrication width of ~ 320 to 340 nm is chosen to provide sufficient sacrificial material. Fabrication of the waveguides is rotated 45 degrees with respect to the crystal axis [110] such that both linear fine structure modes couple equally.

Scanning electron microscope images are taken of the fabricated waveguides, as shown in Figure 4-16. It is noted that small periodic ridges are present in the sides of the waveguides which are an artefact of the proximity correction used during fabrication.

These ridges represent a perturbation of the photonic band structure and will therefore result in scattering losses. Whilst undesirable, their presence is not thought to otherwise adversely affect the properties or photoluminescence of the quantum dots. Additionally, as a result of the recent upgrade to the EBL at the University of Sheffield, defects of this nature are removed. At the ends of the waveguide, a two period Bragg reflector, such as that proposed by Faraon et [14], is fabricated so that light coupled to the waveguide mode is diffracted 90 degrees. This is achieved using a repeating pattern of a half wavelength wide GaAs and air sections. This provides optimal coupling of photoluminescence from the waveguide into the objective lens.

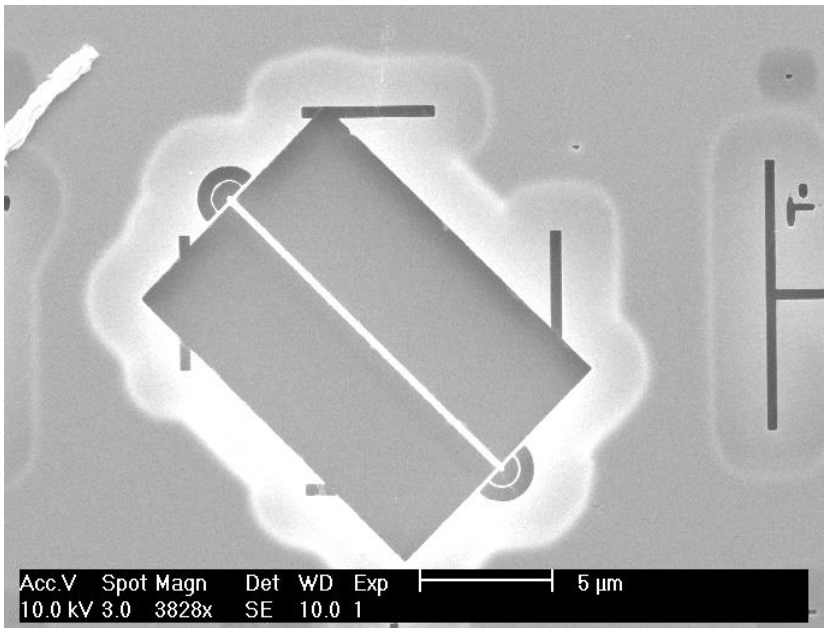

Figure 4-16: SEM of deterministically positioned nanobeam waveguide with a quantum dot located at the centre using solid immersion lens enhanced dot registration.

Spectral Confirmation

In order to measure the photoluminescence in suspended nanobeam waveguides, the quantum dot is excited using above bandgap excitation, as used during dot registration, which is focused onto the centre of the waveguide at the ideal location of the quantum dot. The waveguide coupled signal is observed by aligning the collection spot over either of the two outcouplers at the end of the waveguide. In order to ensure correct alignment of the collection path over the outcoupler, a second laser signal is passed through the collection optics so that it is incident on the sample. The simultaneous use of this second laser signal, a white light source and a CMOS camera enables accurate control of the collection path.

Of the 11 quantum dots registered which were embedded in a nanobeam waveguide, a total of 6 are seen to still exhibit photoluminescence after fabrication. Confirmation that photoluminescence of the 6 successfully registered quantum dots is from the one of the originally registered quantum dots, and not a different dot randomly located, is partially ensured by the low quantum dot density of the sample. This makes it statistically unlikely that a second quantum dot exists in the waveguide. Additionally, a comparison of the spectral features reveals the presence of characteristic features which were identified prior to fabrication, as shown in Figure 4-17.

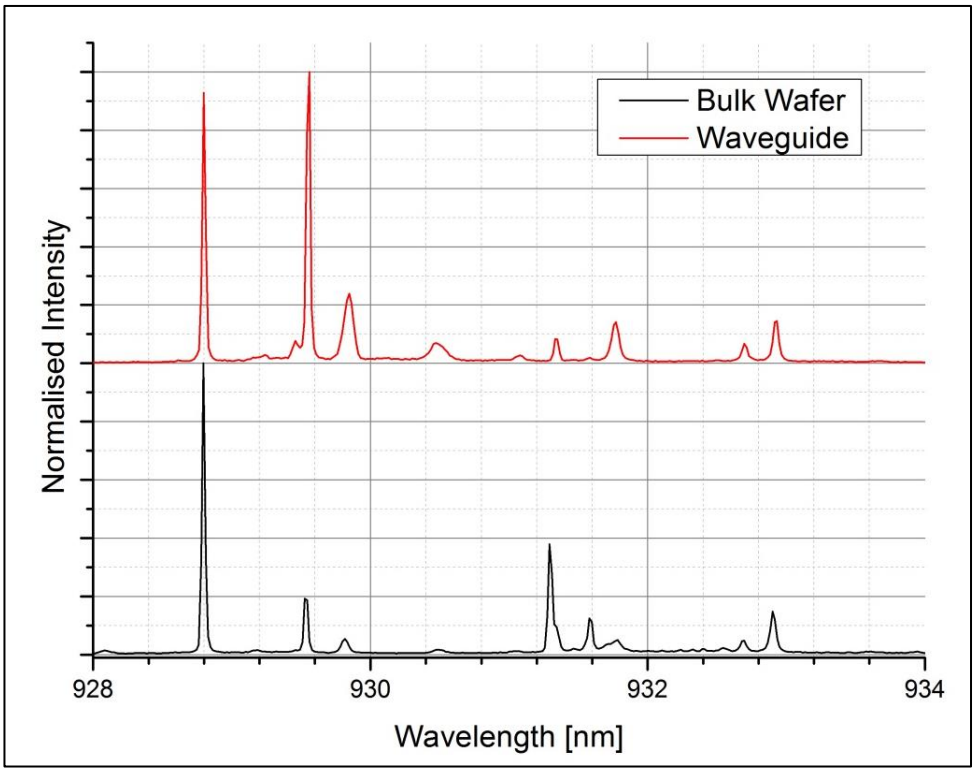

Figure 4-17: Spectral comparison for the same quantum dot prior to (black) and after (red) the deterministic fabrication of a nanobeam waveguide. The primary registered exciton transition at 928.8 nm is still present, however the relative intensity of several excitonic peaks appears to have changed, as well as the formation of new ones.

The primary exciton transition visible at 928.8 nm is clearly visible in both spectra in Figure 4-17 taken before and after the fabrication of the waveguide, indicating both that the quantum dot has successfully been registered and that the spectral properties may be preserved despite significant changes to the local dot environment. In addition to the primary peak at 928.8 nm, which was used to register the position of the quantum dot, several other excitonic transitions align well between the two spectra, such as the doublet around 932.8 nm.

Confirmation that 6 quantum dots have been successfully embedded within a nanobeam waveguide with readily identifiable spectral features represents a success rate of 54.5 %. Whilst this value is lower than would be expected due to the precision in the registration technique, it represents a significant achievement as it now enables the fabrication of scalable photonic structures with multiple quantum dots embedded in them. An explanation for the loss of quantum dots during the registration and deterministic fabrication process is presented in Appendix 1, which provides confidence that it is not the result of dot registration, but rather a property of the sample which requires further investigation.

Power Dependence

The exponents calculated by measuring power dependence of two quantum dots, referred to as dot 1 and dot 2, which show good spectral agreement for measurements taken before and after the fabrication of a waveguide, are presented in Figure 4-18. As is the case when comparing spectrum, where certain spectral features remain unchanged whilst others appear to change significantly, a similar affect is observed for the exponents calculated for the power dependence.

This affect is not surprising given the observed trend in spectral features, however, the lack of correlation between observed changes in the relative intensity of peaks, and changes in the exponent of the power dependence, suggests an additional mechanism affecting exciton states which are present after fabrication. This can be seen for instance in the spectrum shown for dot 1, where the relative intensity of the peak at 908.3 nm shows a significantly different relative intensity but exhibits an unchanged linear power dependence. Conversely, the peak at 910.0 nm shows only minor a variation in the relative intensity with a near constant power dependence between the two measurements.

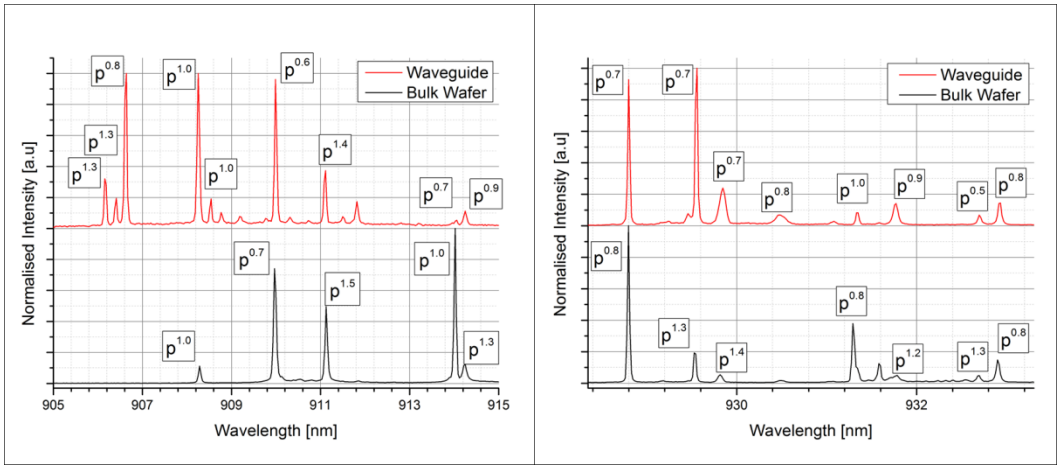

Figure 4-18: Spectrum showing power dependence exponent factors measured for spectral features measured both prior to (black), and after (red), the fabrication of a suspended nanobeam waveguide for Dot 1 (left) and Dot 2 (right).

When further examining the power dependence of spectral features, it is clear that for the quantum dot within the waveguide that the intensity of the photoluminescence is not well described by a single power law. The power dependence for several spectral peaks present in 'dot 1' is shown in Figure 4-19 for before and after the fabrication of a nanobeam waveguide. Although it is not surprising that the power dependence of an exciton transition changes in the nanobeam waveguide, the exact mechanism responsible for the change is hard to quantify. One such explanation may be the result of new charge traps created at the etched surface, which under different excitation powers, result in a local charging in the vicinity of the quantum dot affecting carrier dynamics and the rate of capture.

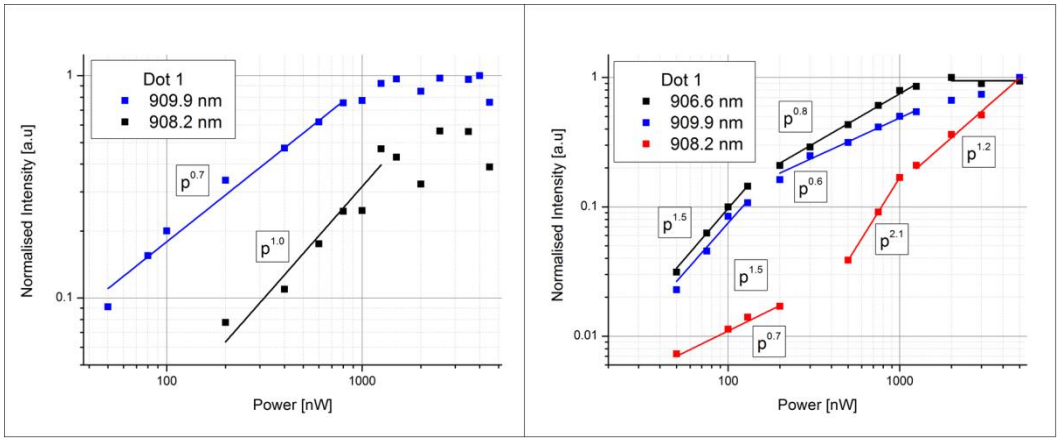

Figure 4-19: Power dependence for a selection of excitonic transitions present in 'Dot 1' before (left) and after (right) the deterministic fabrication of waveguide. Various regimes are identified for the power dependence of the excitonic transitions within the waveguide (right).

Lifetime

The confirmation of unchanged spectral features after the fabrication of a waveguide provides confidence that dot registration can be performed with minimal effect on the properties of the quantum dot. As power dependence measurements showed microscopic changes in the emission properties, lifetime measurements are performed in order to study the relaxation dynamics of the quantum dot.

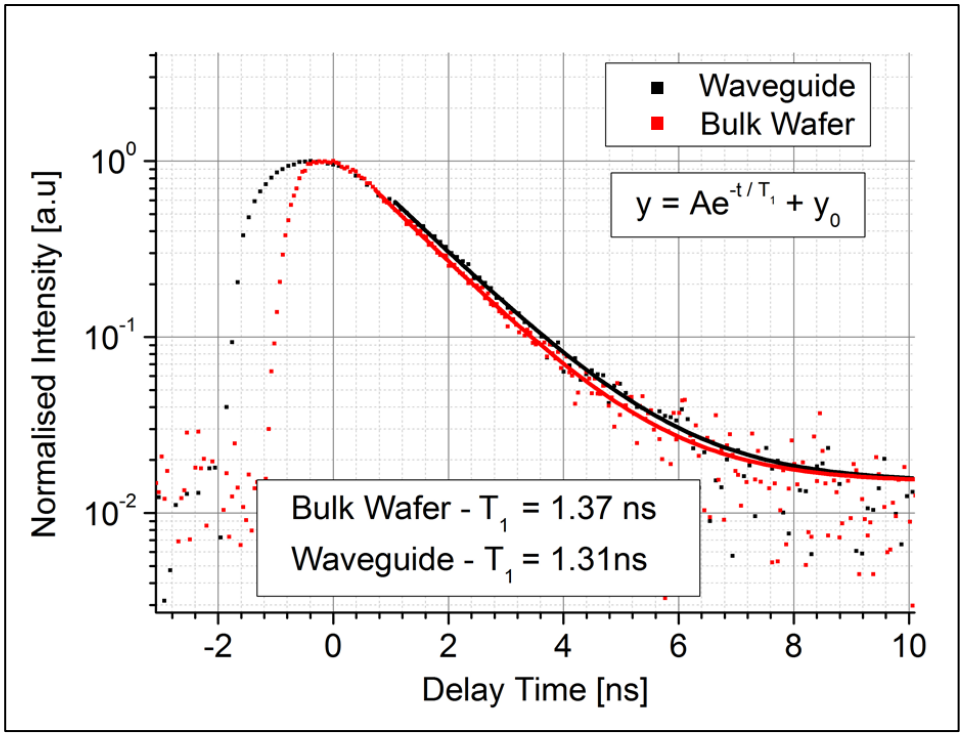

Figure 4-20 – Lifetime measurement of the 910.1 nm peak for dot 1 both before (black) and after (red) the fabrication of a nanobeam waveguide. Good agreement is found between the calculated lifetimes, showing a single exponential decay. An increase in the lifetime of carriers is however seen at times corresponding to the pulse arrival time.

A comparison of the lifetime measured for a single excitonic state is presented in Figure 4-20, both in the bulk wafer prior to fabrication, and once it is embedded within the waveguide. Measurements were carried out as described in chapter 2 using 100 fs pulsed excitation tuned to 870 nm. An excitation power was chosen in both cases such that the observed photoluminescence intensity was 80 % of the saturation intensity. The collected signal was filtered through the output slit of the spectrometer before detection via an APD with a response time of 400 ps.

A lifetime of 1.32 ns and 1.37 ns is obtained for the exciton transition in the bulk wafer and the waveguide respectively. The small difference between the two lifetimes measured is considered the result of the sensitivity of the exponential fit to the

background signal level. The absence of any change agrees well with theory as the waveguide is inherently lossy and should therefore not provide any Purcell enhancement. Additionally, good agreement between measured data and a single exponential fit provides confidence that the relaxation of the quantum dot is due to the spontaneous emission and is unaffected by interactions with phonons or a fluctuating charge environment.

As a point of discussion, the data shown in Figure 4-20 is centred at a time delay of 0 ns according to the time which corresponds to the peak intensity. The increased signal intensity at negative times for the quantum dot within the waveguide should therefore not be interpreted as the pulse arriving earlier, or over a longer period, but rather an increase in the effective lifetime of excited carriers which may be captured by the quantum dot. Although Effects of this type are typically attributed to an increased excitation power used to excite the quantum dot during the lifetime measurement, the excitation power was set to 80 % of the saturation power in both cases. This leads to the conclusion, in agreement with findings from the power dependence, that although the macroscopic spectral properties remain unchanged, carrier dynamics may be adversely affected due to the proximity of the etched surfaces.

The effect is not surprising considering the similarities between nanobeam waveguides and nanowires with embedded quantum dots. Although the QDs within the nanobeam waveguides are more spatially separated from edge of the nanobeam waveguide than QDs in nanowires, both systems will exhibit surface defect states. As a result, carriers generated via above bandgap excitation may relax into these states before further relaxing or being captured by a QD. Although in nanowire systems, this can lead to strong quenching, spectral wondering and blinking, the small QD sizes and large physical separation between the QD and etched surfaces in nanobeam waveguides likely act to reduce the prominence of these effects.

Further examination of this effect would likely require power dependent lifetime measurements, both before and after deterministic fabrication, in order to quantify this broadening. For now however, the good agreement between the extracted lifetimes represents a positive result, indicating that the properties of the QD itself are not adversely affected.

4.4. Optical Spin Readout

Dot registration has so far been shown via the fabrication of additional re-registration markers to have an accuracy of 13.7 nm in the best case. Additionally, the deterministic fabrication of nanobeam waveguides around quantum dots has confirmed that the spectral properties of the quantum dot may be preserved through the fabrication process. In this section, the technique of dot registration is applied to realise quantum dots embedded within nanobeam waveguide which are laterally displaced. The purpose of this displacement is to position the quantum dot at a chiral point so that emission of a photon is preferentially coupled to different directions based on the handedness of the polarisation. As the handedness of the emitted photons is directly related to the spin state of the exciton, the emission direction provides a method to directly read out the spin of the exciton.

The concept of chirality and selective propagation directions in waveguides is an area which has been extensively studied in other fields, especial ones related to radio technology [15]. Recent work has shown that for photonic crystal waveguides, which are analogous to nanobeam waveguides, that by manipulating the position of the quantum dot within the waveguide it is possible to selectively couple the spin of the emitted photon to the emission direction [16]. Because of the lattice nature of photonic crystal waveguide, it is possible to fabricate either symmetric or anti-symmetric waveguides with respect to the propagation direction as depicted in Figure 4-21. For the anti-symmetric case, the propagation direction results in a chiral symmetry between the electric field modes of the waveguide. As a result, the electric field overlap of a suitably located quantum dot with the photonic crystal waveguide mode results in efficient coupling of each spin state to different propagating modes.

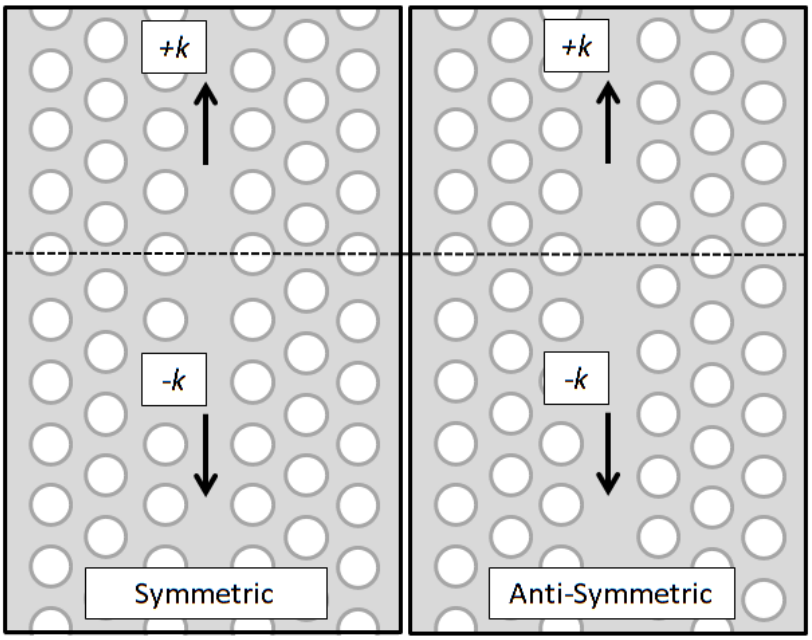

Figure 4-21: Schematic of a symmetric (left) and anti-Symmetric (right) photonic crystal waveguide produced by removing a single row of holes in for a given lattice axis. The symmetry is maintained or broken by shifting the phase crystal axis by a half period on one side with respect to the other.

In practice however, the performance of photonic crystal waveguides is highly sensitive to the size, shape and edge profile of the etched holes. Furthermore, the small lattice period results in a strong spatial dependence in the size and location of chiral points within the waveguide. Due to the infinite periodicity of nanobeam waveguides, the realisation of spin readout in a nanobeam waveguide therefore offers a more robust platform as the basis for quantum information processing.

Spin readout using nanobeam waveguides has previously been performed using a quantum dot displaced in a cross-waveguide in order to create a chiral point [17]. However, it is shown in this work that spin readout is possible in a single symmetric nanobeam waveguide due to the properties of the two fundamental optical modes supported.

The use of dot registration to demonstrate spin readout for quantum dots deterministically displaced form the centre of a waveguide presents an ideal opportunity to confirm the positional accuracy of dot registration independently from the registration process.

4.4.1. Simulations

The mechanism by which the spin of a photon emitted from a quantum dot couples preferentially to a waveguide mode in a single direction can be understood by examining the properties of the fundamental modes supported by the waveguide. Initially, it is not obvious that any mode other than that with the electric field perpendicular to the waveguide axis should be supported. Calculations of the waveguide modes at 950 nm were performed by R. Coles, which have been included with permission, as shown in Figure 4-22. Simulations were performed using a commercial discreet ordinate, finite difference in time domain eigenmode solver, Lumerical.

Calculations show the presence of two transverse electric field modes, referred to as TE_x and TE_y for electric fields aligned along the waveguide length and width respectively. For the TE_y mode, it can be see that a single anti-node exists, located at the centre of the waveguide. The relative phase of the electric field for this mode is calculated to be uniform across a slice in the x axis of the waveguide. In contrast, the TE_x mode has two anti-nodes located at either side of the waveguide, where the relative phase between the two sides of the waveguide flips from $\pm \pi/2$ to $\mp \pi/2$.

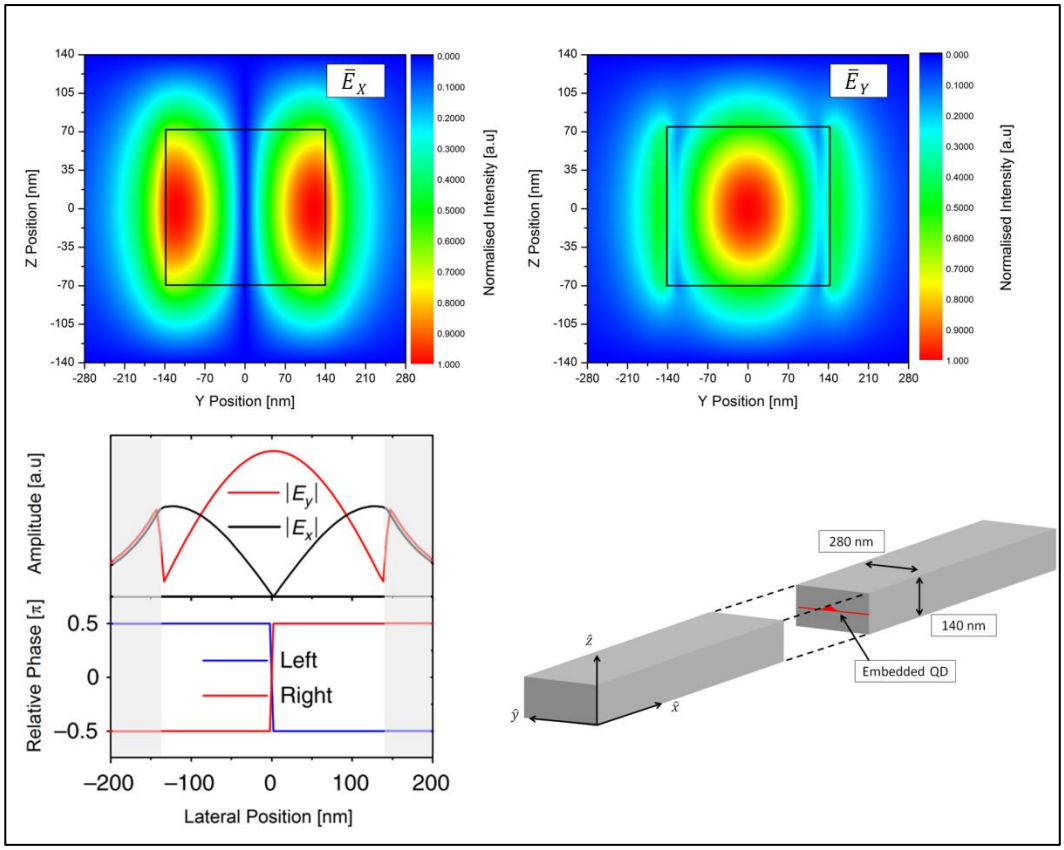

Figure 4-22 – Electric field profiles are shown for the two transverse electric modes TE_x (top left) and TE_y (top right) which have the electric field aligned along and perpendicular to the waveguide length respectively. The relative phase of the TE_x and TE_y modes is shown to switch between $+\pi/2$ to $-\pi/2$ at the centre of the waveguide (bottom left). A schematic of the waveguide is presented for reference (bottom right).

It can be seen that at a certain displacement, 90 nm from the centre of the waveguide, the amplitudes of the two electric field modes of the waveguide are equal. These points are referred to as 'C-Points' as they efficiently couple circularly polarised light. At this displaced point, the relative phase between the TE_x and TE_y modes is calculated to be $\pm \pi/2$ depending on the propagation direction of the mode. Similarly, the circularly polarised light emitted from an embedded quantum dot can be thought of as two orthogonal electric fields with a $\pm \pi/2$ phase shift between them, where the sign depends on the handedness of the polarisation. It can be seen therefore that due to the fixed phase between the two orthogonal electric fields of a given handedness of circularly polarised light, that the emission will be into a single mode, propagating in one direction. At the centre of the waveguide, where the amplitude of the TE_x mode is calculated to be zero, only the TE_y mode is supported, resulting in linearly polarised propagating modes.

Further simulations are performed to determine both the wavelength and positional sensitivity of the spin readout affect. Simulations are performed using a circularly

polarised dipole source at various lateral displacements. Flux monitors are used to record the transmitted power through each end of an infinitely long waveguide as a function of the dipole displacement. The contrast between the two propagation directions is calculated as the difference in the recorded flux, normalised to the total flux coupled to the waveguide. From the data presented in Figure 4-23, it can be seen that the contrast is insensitive to the wavelength of the emission. This is attributed to the weak confinement of the electric field mode within the waveguide.

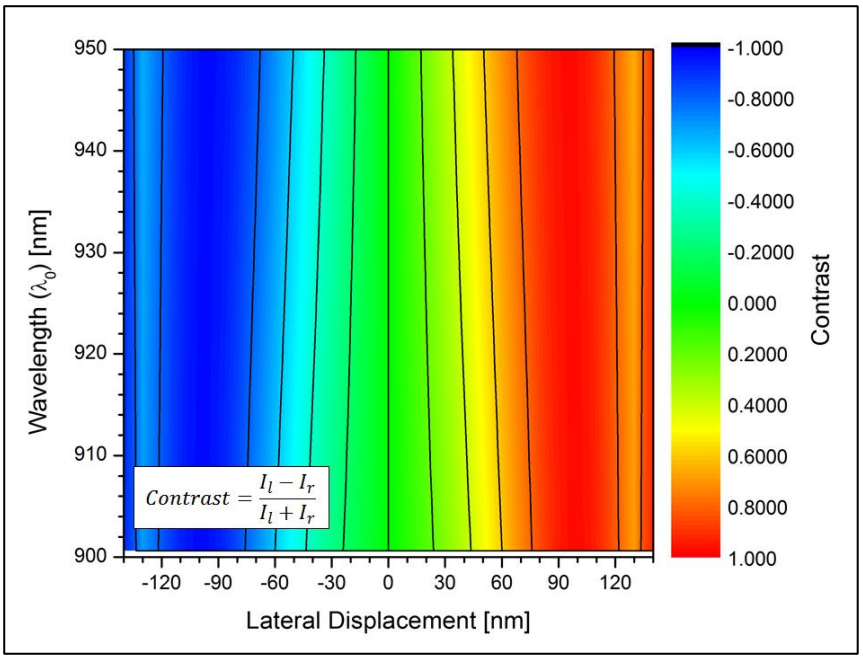

Figure 4-23 – Calculated contrast observed between the two emission directions for a circularly polarised dipole as a function of emission wavelength and lateral displacement within the waveguide. Contrast is defined as the difference between the measured signal intensity, normalised to the total signal intensity.

Simulations therefore show that spin readout should be possible within symmetric nanobeam waveguide structures due to the presence of a chiraly circularly polarised mode supported by the waveguide. Additionally, nanobeam waveguides should exhibit contrast between the two spin states equal to that of photonic crystal waveguides, whilst being less sensitive to fabrication defects or the emission wavelength.

4.4.2. Deterministic Spin Readout

Based on simulations, dot registration is used to deterministically position two quantum dots in a nanobeam waveguide. For one of the quantum dots (referred to as dot I), the waveguide is shifted within the EBL design file such that the quantum dot is displaced laterally 90 nm with respect to the centre so that it is located at the 'C-Point' of the waveguide. The other quantum dot (dot II) is kept at the centre of the waveguide ('L-

Point') as a control. Between the two quantum dots, it should be possible to detect directional and uniform spin readout respectively at each out-coupler. A schematic of the proposed devices is shown in Figure 4-24.

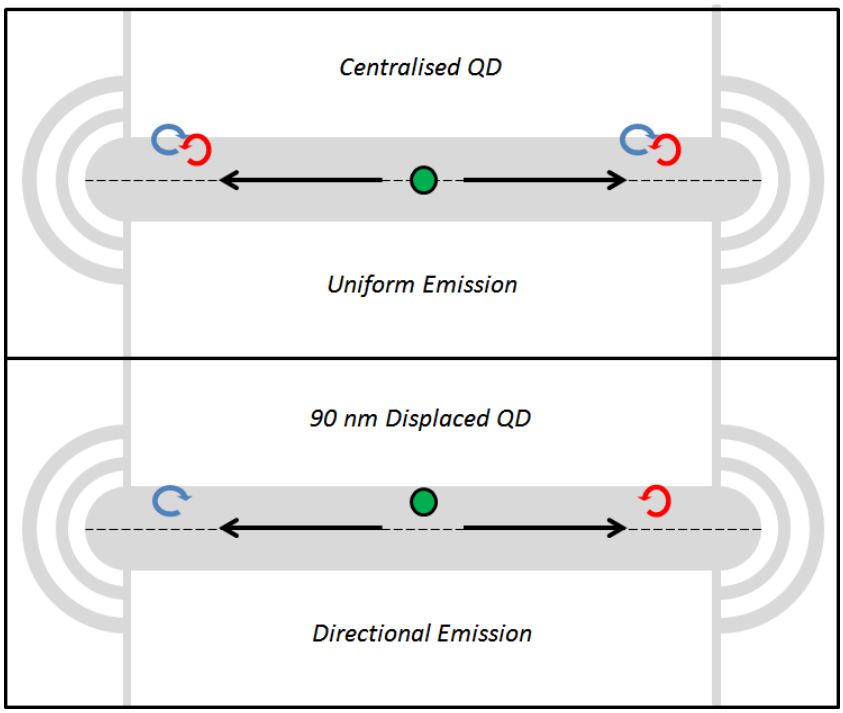

Figure 4-24: Sketch showing the proposed layout for displaced quantum dots to realise directional spin coupling. Dot I will be displaced 90 nm latteraly (bottom) with resepct to the waveguide axis and is expected to show preferential coupling of individual spin states. Dot II will be maintained in the centre of the waveguide (top) and should show uniform coupling of the spin states.

Confirmation that the quantum dots survived the fabrication processes without major spectral changes is performed by measuring the photoluminescence before and after fabrication. For the two dots selected, it is found that the primary peak used to register the position of the quantum dot has survived the fabrication process. A comparison of the spectrum for the two dots before and after fabrication is presented in Figure 4-25. It is interesting, that the displacement of the quantum dot closer to the surface of the waveguide did not result in more significant spectral changes, such as those discussed in section 4.3.2.

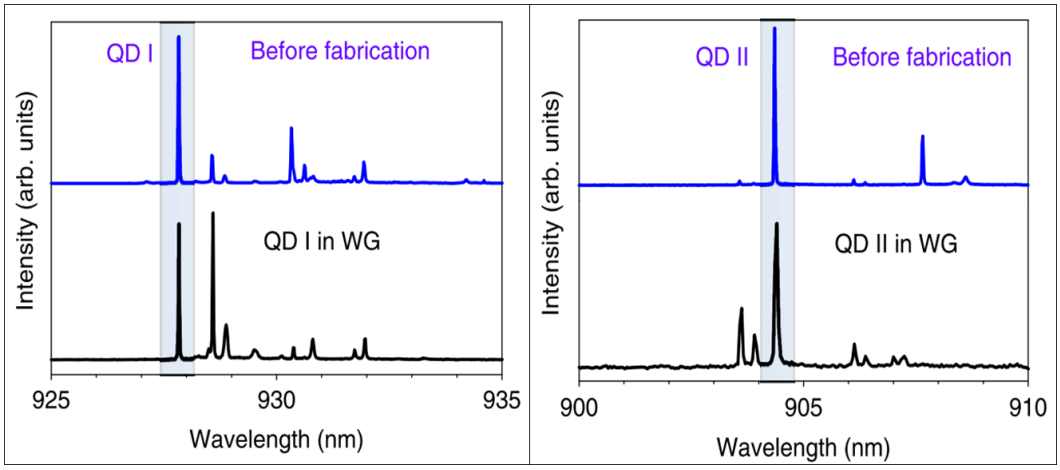

Figure 4-25: Spectral comparison of quantum dot I (left) and II (right) prior to, and after, the fabrication of nanobeam waveguide. The primary peak used for registration is highlighted which is show to be present after the fabrication of waveguides.

For neutral and charged excitons, the two optically active transitions (M = ± 1) are degenerate in energy, ignoring the fine structure splitting of neutral excitons. In order to distinguish the two spin states, a superconducting magnet is used to Zeeman split the transitions so that they may be resolved by conventional spectroscopic techniques. A solenoidal magnetic field is setup so that the field is parallel to the growth axis, referred to as the Faraday geometry. The coupling of the quantum dot to the magnetic field arises via interactions with the spin of electrons and holes, which for the optically bright neutral exciton transitions can be included in the Hamiltonian as an additional potential with a factor of $\pm g_X \mu_B B_Z$. Here, g_X represents the exciton g-factor given by the contributions of the electron and hole g-factors, and B_Z represents the external magnetic field applied in the growth direction.

The resulting eigenenergies and eigenstates are given by Equation 4-1 and Equation 4-2 respectively [18]. At high magnetic field strengths, the mixing of the two bright states due to the fine structure splitting becomes negligible, and the eigenstates tend towards pure states.

$$E_{\uparrow,\downarrow} = \frac{1}{2}\left(\delta_0 \mp \sqrt[2]{(g_X \mu_B B_Z)^2 + {\delta_1}^2}\right) \tag{4.1}$$

Equation 4-1: Eigenenergies for neutral exciton bright states. $\boldsymbol{\delta_0}$ is the splitting of the bright and dark excitonic states and $\boldsymbol{\delta_1}$ is the splitting between the bright states due to the electron hole exchange interaction.

$$\left|X_{\uparrow,\downarrow}\right\rangle = \frac{\left(|\uparrow\rangle \pm \left(\sqrt[2]{1+\Delta^2} \mp \Delta\right)|\downarrow\rangle\right)}{\sqrt{2}\sqrt{1+\Delta^2 \mp \Delta\sqrt[2]{1+\Delta^2}}};\ \Delta = \frac{g_X \mu_B B_Z}{\delta_1} \tag{4.2}$$

Equation 4-2: Eigenstates for neutral exciton bright states

Measurements of the directionality achieved for the displaced quantum dot (dot I) are performed by measuring the photoluminescence from the left and right out couplers as a function of the magnetic field strength. Excitation is performed using an above bandgap laser at a fixed excitation power focused on the centre of the waveguide at the quantum dots location. The total photoluminescence spectrum measured from both the left and right out coupler is shown in Figure 4-26. It can be seen clearly that a high degree of contrast is achievable between the two collections paths, measured to be 92 ± 3 % and 80 ± 3 % for the left and right outcouplers respectively.

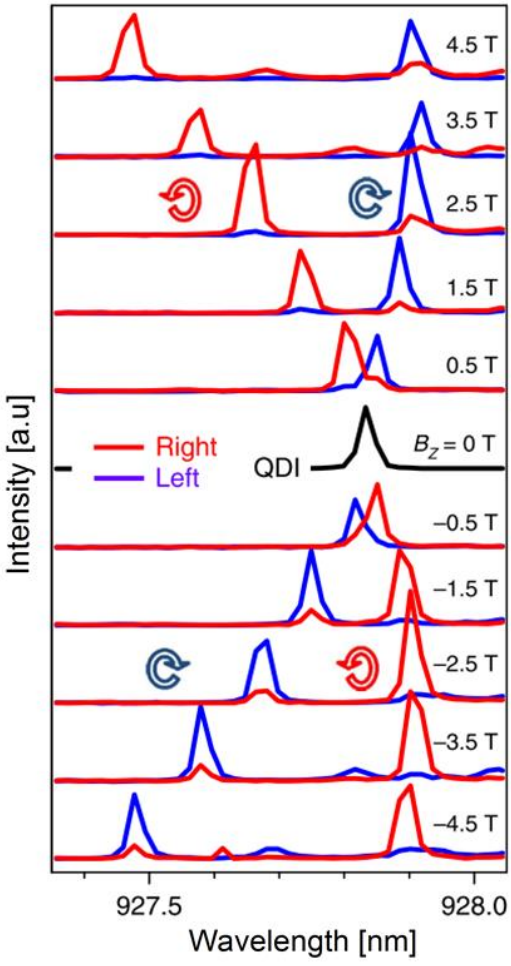

Figure 4-26 – Signal measured from the left (blue) and right (red) outcouplers of the nanobeam waveguide for dot I as a function of magnetic field strength. Spectral artefacts which may have explained spin readout are discounted by scanning the magnetic field in the positive and negative directions.

The measurements of Figure 4-26 and the contrast values deduced are in good agreement with the simulated values of Figure 4-23 for a dot at a chiral point. However, the simulations of Figure 4-23 were carried out for an infinitly long waveguide. In reality, the presence of out couplers results in a reflected component in the signal which not only reduces the contrast observed in each direction, but also acts to shift the position of the maximum contrast. Repeating the FDTD simulations to include outcouplers at the end of the waveguide results in the revised position dependence of spin readout, as shown in Figure 4-27. It is therefore concluded that the positional accuracy of the deterministically fabricated quantum dot must be within 15 nm in order to explain the strong agreement between simulated and measured results.

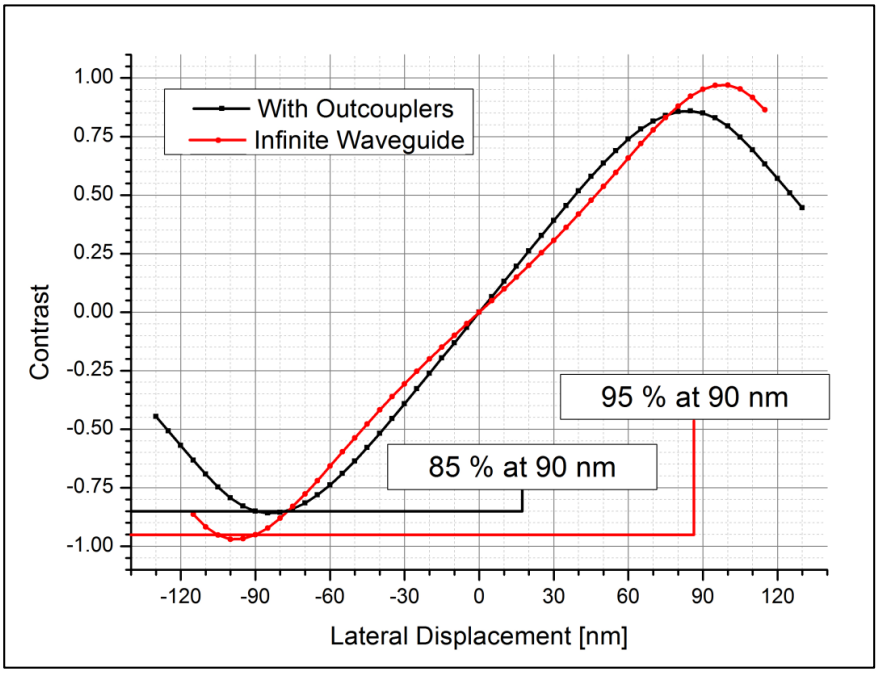

Figure 4-27 – FDTD simulations of the contrast expected for a quantum dot emitting at 925 nm for various displacements in an infinite waveguide (red) and one terminated with outcouplers (black).

Additionally, measurements of quantum dot II located at the centre of the waveguide show good agreement with simulations which predict uniform coupling. A signal contrast of 3 ± 6 % and 24 ± 4 % is measured for the left and right outcouplers respectively. The worst deviation of 24 % is seen to correspond to a shift of ~ 20 nm, again, in good agreement with the total accuracy calculated via re-registration of quantum dots (13.7 nm at best). Spectra taken from the left and right outcouplers for dot II are presented Figure 4-28.

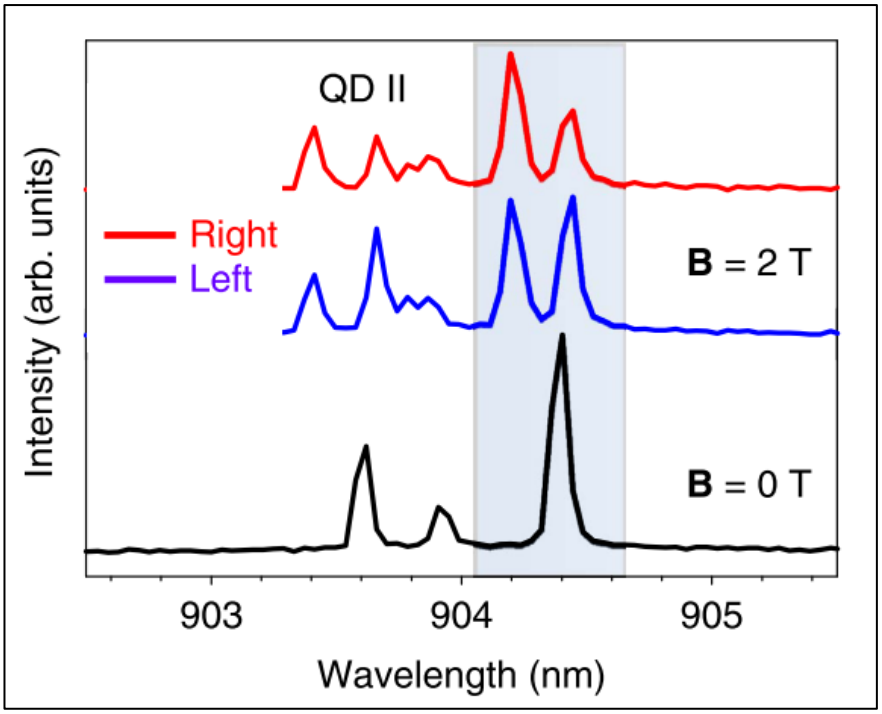

Figure 4-28 – Demonstration of uniform spin readout at large magnetic fields for Dot II as expected for a quantum dot located in the centre of a waveguide. Signal collected out of the left (blue) and right (red) outcouplers show clear indications of both Zeeman split spectral peaks.

Whilst both dots show good agreement with simulations and provide confidence in the dot registration technique, there is an apparent asymmetry in the contrast measured which is not predicted in simulations, even when including additional components such as outcouplers. It is possible that due to the simplistic nature of the models which approximate the source as a point dipole, that any asymmetry in the quantum dot itself may affect measurements. Additionally, defects in the fabrication of the outcouplers which increases or decreases the reflected signal of one path with respect to the other could introduce asymmetry in the contrast. An extreme case is shown in Figure 4-29 where the previously modelled infinitely long waveguide is terminated at one end with an outcoupler. Whilst it is not thought that the fabrication defects typically associated with EBL and ICP etching will result in significant differences between the outcouplers, it may nevertheless influence the contrast.

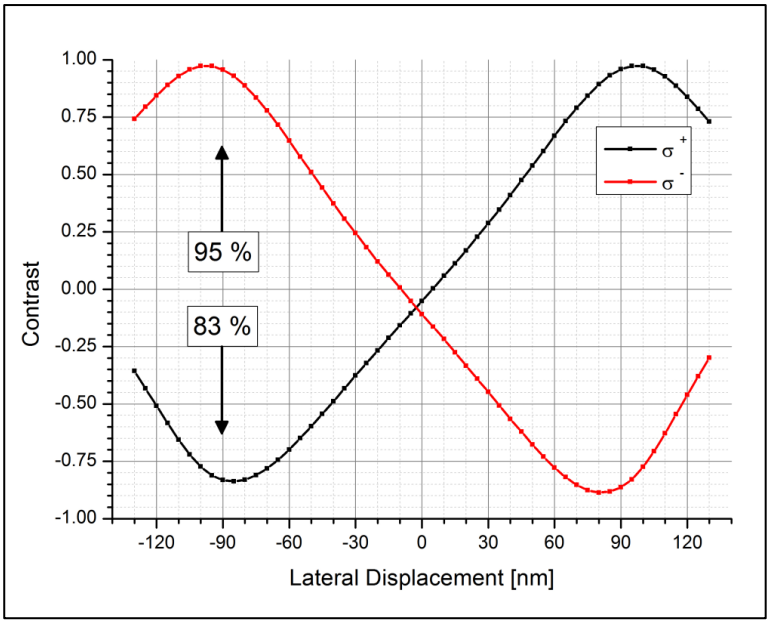

Figure 4-29 – Position dependence of spin readout for a quantum dot emitting at 925 nm in an infinitely long waveguide, terminated at only one end with an outcoupler. This predicts an asymmetry of up to 12 % for a quantum dot displaced 90 nm.

4.5. Conclusions

The technique of solid immersion lens enhanced dot registration has been tested in this chapter to determine the accuracy and reliability that a structure can be deterministically fabricated around a quantum dot. It was shown through the fabrication of re-registration markers at a pre-determined distance from the quantum dot, that they could be positioned within 13.7 nm of the original registered position. Additionally, the fabrication of nanobeam waveguides, and in particular the demonstration of position dependent spin readout, provided further confirmation of the positional accuracy of the dot registration technique. It was concluded that in order to explain small discrepancies between simulations and experimental results, a registration error of ~ 20 nm was sufficient, in good agreement with the value obtained from re-registration measurements. It is concluded therefore that deterministic fabrication can be realised with a precision comparable to the lateral sizes of the quantum dot.

Additionally, the reliability of the registration technique has been demonstrated by characterising the performance of quantum dots prior to and after the fabrication of nanobeam waveguides. Measurements of the spectral properties show that it is possible to embed a quantum dot within a nanobeam waveguide with known spectral properties with a success rate of greater than 50 %.

4.6. References

[1] A. N. Vamivakas and M. Atatüre, “Photons and (artificial) atoms: an overview of optical spectroscopy techniques on quantum dots,” *Contemp. Phys.*, vol. 51, no. 1, pp. 17–36, Jan. 2010.

[2] D. Richter, R. Hafenbrak, and K. D. Jöns, “Carrier dynamics in InAs / AlAs quantum dots : lack in carrier transfer from wetting layer to quantum dots.”

[3] H. Z. Song, T. Usuki, S. Hirose, K. Takemoto, Y. Nakata, N. Yokoyama, and Y. Sakuma, “Site-controlled photoluminescence at telecommunication wavelength from InAs/InP quantum dots,” *Appl. Phys. Lett.*, vol. 86, no. 11, pp. 1–3, 2005.

[4] M. H. Baier, A. Malko, E. Pelucchi, D. Y. Oberli, and E. Kapon, “Quantum-dot exciton dynamics probed by photon-correlation spectroscopy,” *Phys. Rev. B - Condens. Matter Mater. Phys.*, vol. 73, no. 20, pp. 1–5, 2006.

[5] F. Heinrichsdorff, A. Krost, M. Grundmann, D. Bimberg, F. Bertram, J. Christen, A. Kosogov, and P. Werner, “Self organization phenomena of quantum dots grown by metalorganic chemical vapour deposition,” *J. Cryst. Growth*, vol. 170, no. 1–4, pp. 568–573, 1997.

[6] B. Ohnesorge, M. Albrecht, J. Oshinowo, A. Forchel, and Y. Arakawa, “Rapid carrier relaxation in self-assembled InxGa1-xAs/GaAs quantum dots.,” *Phys. Rev. B. Condens. Matter*, vol. 54, no. 16, pp. 11532–11538, 1996.

[7] P. Borri, W. Langbein, S. Schneider, U. Woggon, R. Sellin, D. Ouyang, and D. Bimberg, “Ultralong Dephasing Time in InGaAs Quantum Dots,” *Phys. Rev. Lett.*, vol. 87, no. 15, pp. 1–4, Sep. 2001.

[8] P. Lodahl, S. Mahmoodian, and S. Stobbe, “Interfacing single photons and single quantum dots with photonic nanostructures,” *Rev. Mod. Phys.*, vol. 87, no. 2, pp. 347–400, 2015.

[9] C. Santori, D. Fattal, J. Vučković, G. S. Solomon, E. Waks, and Y. Yamamoto, “Submicrosecond correlations in photoluminescence from InAs quantum dots,” *Phys. Rev. B*, vol. 69, no. 20, pp. 1–8, May 2004.

[10] C. Santori, D. Fattal, J. Vucković, G. S. Solomon, and Y. Yamamoto,

"Indistinguishable photons from a single-photon device.," *Nature*, vol. 419, no. 6907, pp. 594–7, Oct. 2002.

[11] S. Ates, S. Ulrich, S. Reitzenstein, A. Löffler, A. Forchel, and P. Michler, "Post-Selected Indistinguishable Photons from the Resonance Fluorescence of a Single Quantum Dot in a Microcavity," *Phys. Rev. Lett.*, vol. 103, no. 16, pp. 1–4, Oct. 2009.

[12] C. Matthiesen, A. Vamivakas, and M. Atatüre, "Subnatural Linewidth Single Photons from a Quantum Dot," *Phys. Rev. Lett.*, vol. 108, no. 9, pp. 1–4, Feb. 2012.

[13] S. G. Carter, T. M. Sweeney, M. Kim, C. S. Kim, D. Solenov, S. E. Economou, T. L. Reinecke, L. Yang, A. S. Bracker, D. Gammon, and E. Economou, "Supplementary Material : Quantum control of a spin qubit coupled to a photonic crystal cavity," no. March, pp. 1–6, 2013.

[14] A. Faraon, I. Fushman, D. Englund, N. Stoltz, P. Petroff, and J. Vučković, "Coherent generation of non-classical light on a chip via photon-induced tunnelling and blockade," *Nat. Phys.*, vol. 4, no. 11, pp. 859–863, 2008.

[15] R. Ro, V. V. Varadan, and V. K. Varadan, "Electromagnetic activity and absorption in microwave chiral composites," *IEE Proc. H Microwaves, Antennas Propag.*, vol. 139, no. 5, p. 441, 1992.

[16] I. Söllner, S. Mahmoodian, L. Midolo, A. Javadi, G. Kir, T. Pregnolato, H. El-ella, E. H. Lee, J. D. Song, S. Stobbe, and P. Lodahl, "Deterministic photon – emitter coupling in chiral photonic circuits," *Nat. Nanotechnol.*, vol. 10, no. 9, pp. 775–778, 2015.

[17] I. J. Luxmoore, N. A. Wasley, A. J. Ramsay, A. C. T. Thijssen, R. Oulton, M. Hugues, S. Kasture, V. G. Achanta, A. M. Fox, and M. S. Skolnick, "Interfacing Spins in an InGaAs Quantum Dot to a Semiconductor Waveguide Circuit Using Emitted Photons," *Phys. Rev. Lett.*, vol. 110, no. 3, p. 37402, Jan. 2013.

[18] P. Michler, *Single Quantum Dots: Fundamentals, Applications and New Concepts*. Springer, 2003.

5. Waveguide Coupled Resonance Fluorescence

5.1. Introduction

For optical quantum information processing, the coherence time, which can be used to determine the indistinguishability of a photon source, can also be used as a measurement of the quality of the system. In order to realise high fidelity quantum operations, many schemes such as teleportation and linear computation require that the emission of sequential photons be coherent with one another. If scalable photonic architectures are therefore to be realised, the emission of single photons must be indistinguishable from those emitted by other single photon sources [1]. As such, many schemes exist for the generation of single photons with long coherences, including parametric down conversion [2], trapped ions [3], colour centres [4] as well as quantum dots.

In this chapter, resonant excitation of a quantum dot embedded in a nanobeam waveguide is demonstrated, where it is shown that the coherence of the emitted photons is significantly improved when compared to those generated using above bandgap excitation. As an introduction to the work presented, a brief discussion of coherence with respect to photons is first given as well as a discussion of recent works which have also demonstrated resonant excitation. This is followed by a discussion of the proposed excitation geometry using nanobeam waveguides to efficiently prevent the excitation laser from being detected, whilst maintaining efficient coupling of photons emitted from the quantum dot. Finally, experimental results are presented with a summary of key findings discussed in the conclusion section at the end.

5.1.1. Coherence

The coherence of photons emitted from an individual quantum system can be characterised by its coherence time, T_2, given by the Heisenberg time-energy uncertainty principle $\Delta E \Delta T_2 \geq h/2\pi$. Here, ΔE represents the uncertainty in the emission energy of the photon which occurs over the timescale ΔT_2. In practice, when considering the emission of multiple photons from several single photon sources, or an ensemble of time delayed single photons from the same single photon source, the time T_2 becomes a directly measurable property which enables the quantification of the coherence time [5].

As the coherence time is a measure of the phase relationship of spectral components between light trains, it is related to the lifetime (T_1) of the intensity distribution by the Fourier transform. The spectral width of photons emitted from a quantum dot is therefore limited by the spontaneous emission rate ($\Gamma = \frac{1}{T_1}$). In this so called Fourier transform limit, the coherence time has a maximum value of $T_2 = 2T_1$. As the properties of quantum dots are strongly influenced by their solid state environments, coherence times are however typically much less than the exciton lifetime (typically < 200 ps for near surface QD's [6][7]). The reduction in the coherence time is attributed to pure dephasing, which is the loss of coherence without emission of a photon [8] due to interactions of the excited state with photons, phonons and charge fluctuations in the surrounding environment. In the simplest interpretation, the influence of the dephasing mechanisms are assumed to be Markovian, and the rate of dephasing can be characterised by $\Gamma_{dp} = \frac{1}{T_2^*}$ [9]. The resulting Lorentzian spectral linewidth can therefore be characterised by the spontaneous emission lifetime and coherence times given by Equation 5-1.

$$\frac{1}{T_2} = \frac{1}{2T_1} + \frac{1}{T_2^*} \tag{5.1}$$

Equation 5-1 – Relationship between the coherence time T_2 and the lifetime of spontaneous emission T_1 including the loss of coherence due to pure dephasing on the time scale T_2^*

Under above bandgap excitation of quantum dots, numerous charge carriers are generated in the surrounding bulk semiconductor which may be captured by a quantum dot. As the number of carriers generated increase with excitation power, so too does the interaction of charge fluctuations with the quantum dot. This leads to an increase in the rate of pure dephasing [10]. For the excited carriers generated, as a result of the continuum of states, capture of these carriers into the wetting layer and quantum dot is highly efficient and occurs over times scales of 10's ps [11]. In order for these excited carriers to be captured into the quantum dot, multiple inelastic scatters occur which quickly removes any coherence between the excited state and the excitation laser. Additionally, because of the different relaxation pathways available, the production of excitons in the quantum dot experiences timing jitter, which further acts to reduce the coherence time [12].

5.1.2. Resonance Fluorescence

As a result of induced de-coherence in quantum dots when using above bandgap excitation, the use of quasi-resonant, p-shell, and resonant, s-shell, excitation are of considerable interest [13]. By resonantly exciting the exciton transition, which is lower in energy than the bandgap of the bulk semiconductor, no excited carriers are created, and the manipulation of the exciton state may be coherent. For single mode lasers, the linewidth of the excitation laser (~ MHz) is typically much smaller than the natural linewidth of the exciton transition (~ GHz), even in the absence of pure dephasing. In order to describe the process of resonant absorption and emission, the absorption and emission coefficients of photons proposed by Weisskopf [14] for the exponential decay rate of spontaneous emission are modified by Heitler to account for the vastly different linewidths [15]. The resulting intensity distribution for resonantly emitted photons is given by Equation 5-2.

$$w(k_{laser}) = \sum_{\lambda} \left| b_{\lambda,laser}(\infty) \right|^2 = \frac{2\pi}{\hbar \Gamma k_0 c} \frac{E_0 I_0(k_{laser})}{[(k_0 - k_{laser})^2 + \hbar^2 \gamma^2 / 4]} \tag{5.2}$$

Equation 5-2 – Spectral intensity distribution of resonance fluorescence when the excitation laser has a significantly narrower spectral width than the natural width than the exciton transition, given by $I_0(k_{laser})$. Γ *represents the lifetime of the transition and the natural linewidth is given by* γ.

The total intensity of the resonance fluorescence is therefore proportional to the intensity distribution of the resonant laser, $I_0(k_{laser})$. As the laser line is significantly narrower than the natural linewidth of the quantum dot, the denominator is approximately constant over the range where $I_0(k_{laser}) \neq 0$. Therefore, the intensity distribution of the emitted photons has exactly the same spectral shape as the excitation laser. Following the uncertainty principle arguments of earlier, the emitted photons are coherent with the resonant excitation laser, and take on the coherence time $T_2 = T_{2,Laser}$. This is however only true under extremely low excitation powers, as will be discussed, and is referred to as the Heitler regime.

When exciting the exciton transition with a narrow resonant laser, under low excitation powers, it is shown above that the emission line shape is identical to that of the excitation laser. In order for this to be true, the exciton must retain some memory of the absorbed photon, otherwise the spectral emission profile would simply be the same as the natural linewidth of the exciton. As a result, the absorption and emission of resonant photons cannot be considered as separate events. This leads to the question of what state the quantum system is in, and when absorption or emission has occurred. As the emission

lifetime is still given by $\Gamma = \frac{1}{T_1}$, a measurement of the excited state population can be performed via an inelastic scattering on time scales shorter than $\frac{1}{\gamma}$. However, by probing the systems on such time scales, the coherence of the system is interrupted and the linewidth is given by $\gamma\hbar$. It is therefore shown that while the coherence of a quantum dot can be significantly improved, taking on the coherence of the resonant excitation source under low excitation powers, at higher excitation powers, the coherence of the quantum dot is diminished.

5.1.3. Laser Suppression

To date, efforts to realise resonance fluorescence, the spectrally resonant excitation and emission of photons, of quantum dots have relied on specialised excitation and collection geometries in order to distinguish the photons emitted from the quantum dot with respect to the excitation laser. These techniques, which typically employ novel excitation and collection geometries, off chip filtering or destructive interference of the emitted photons with the excitation laser, are poorly suited for scalable quantum information processing architectures. A brief review of significant milestones which preceded the work presented here is discussed in order to demonstrate the significance of waveguide coupled resonance fluorescence with strong laser rejection.

In order to spatially separate the resonance fluorescence from the excitation laser, a novel excitation regime of quantum dots located in a weak microcavity has been proposed by Muller et al. [18]. By introducing the excitation laser at the side of the micro cavity, the propagation direction of the resonant laser is orthogonal to that of the cavity coupled resonance fluorescence. A lifetime for the quantum dot was reported of 290 ps, which represents a modest Purcell enhancement and likely contributes to improved signal levels. Whilst this technique proved it was possible to realise a useful source of single photons with a significantly improved lifetimes and coherences, it ultimately relies on off chip collection and detection. The significant losses associated with optical collection, such as beam splitters and fibre coupling will therefore likely limit the number of useful photons. A similar method of exciting and collecting with orthogonal polarisations rather than directions is used by Matthiesen et al to achieve a high levels of laser rejection off chip [19], however it is again noted that the problems associated with off-chip detection remain.

5.2. Excitation Regime

Work in this chapter demonstrates the realisation of resonant excitation of a quantum dot, with the resonance fluorescence efficiently coupled into a nanobeam waveguide [20]. It is noted that significant technical challenges remain in order to realise on chip detection [21], and so off chip detection is performed using a diffraction grating at the end of a waveguide to efficiently couple light into the collection optics. In order to provide sufficient laser rejection from the scattered resonant laser and resolve the emission of resonant photons off chip, polarisation rejection is used. Resonant excitation is therefore performed using linearly polarised light, with the collected signal filtered through a second linear polariser which is orthogonal to the first. The revised experimental setup for the bath cryostat described in chapter 2, including polarisation optics, is shown in Figure 5-1. It is noted that in order to maintain a highly linearly polarised excitation laser onto the sample, the linear polarisers are placed as close as possible in the optical path to the to the cubic beam splitter. Additionally, as optical components between the initial and final linear polariser, such as lenses and beam splitters, also exhibit birefringence, the initial linearly polarised light is partially rotated to an elliptical polarisation. A zero order Soleil-Babinet compensator is therefore used to correct for this, which allows for strong laser rejection.

As discussed earlier, resonant fluorescence is a quasi-excitation process, where the absorption and emission of a photon cannot be distinguished, which couples the laser with the excitonic states of the quantum dot. In order to efficiently couple the excitation laser, a Weierstrass solid immersion lens (sSIL) [22] was mounted on top of the nanobeam waveguide. Although the presence of outcouplers on the waveguide alter the far-field profile of emitted light, resulting in little collection enhancement due to the solid immersion lens, the decreased excitation spot size it provides results in a significant increase in the power density. Therefore, for the same local field strength, the intensity of the resonant laser can be reduced by a factor of r^2 which reduces the intensity of scattered light. As the diffraction limited spot size is proportional to the refractive index, for a ZrO_2 sold immersion lens, $r^2 \approx 4.5$ at 920 nm. The reduced excitation power in combination with a higher spatial resolution results in better suppression of scattered laser signal from the collection path.

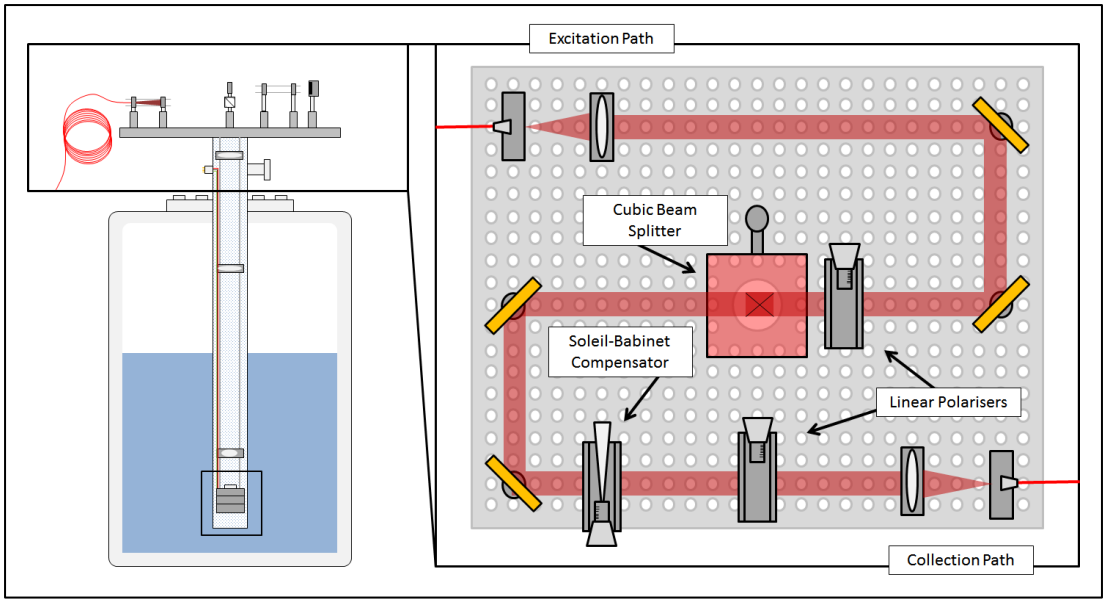

Figure 5-1 – Bath cryostat experimental setup for resonance fluorescence. The fibre coupled excitation path is linearly polarised prior to splitting through a 50:50 cubic beam splitter. Telescopic optics are used to focus and collimate the excitation laser to the sample within the cryostat, and simultaneously couple the resonance fluorescence back to the cubic beam splitter. The collected signal is deflected through a Soleil-Babinet compensator and second linear polariser, orthogonal to the first, prior to coupling into a single mode fibre. Bandpass filters used to filter the above bandgap excitation are not show.

Nanobeam waveguides are fabricated at regular intervals on the sample, aligned to the [100] crystal axis of the GaAs, as shown in Figure 5-2. This orientation is chosen as the linearly polarised states of the fine structure split neutral excitons, polarised along the [110] and [1$\underline{1}$0] axis, as well as the circularly polarised charged excitons will couple equally to the waveguide [23]. An out-coupler is fabricated at one end of the waveguide in order to optimally couple resonance fluorescence along the collection path. As a result of the asymmetric shape of the waveguide, the excitation spot can be spatially separated from the collection spot by more than 10 µm for suitably located quantum dots.

The solid immersion lens is placed on the surface of the sample and using an optical microscope is positioned above the nanobeam waveguide. High viscous bonding is used to secure the solid immersion lens to the sample so that it can be mounted into the bath cryostat without moving when the air is removed. Care is taken throughout the process to ensure the waveguide is not collapsed as result of the solid immersion lens using a white light source to observe the sample through the solid immersion lens.

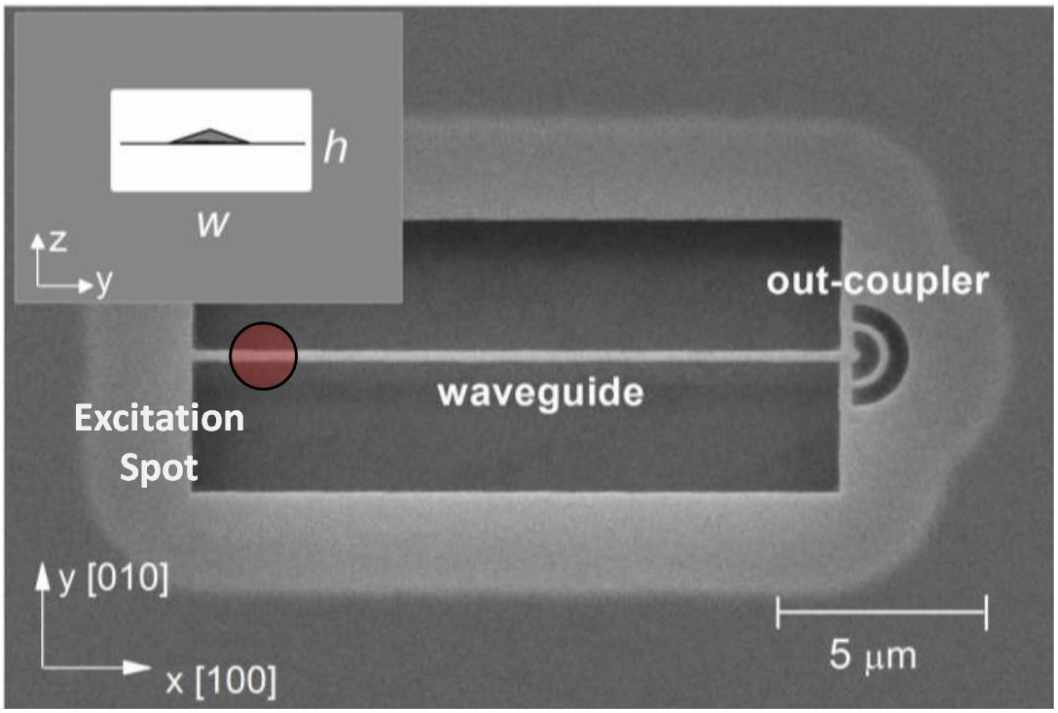

Figure 5-2 – SEM of a 15 μm long nanobeam waveguide fabricated in the [100] crystal axis with a single out-coupler at one end. The insert show a representation of a pyramidal quantum dot embedded within the 280 nm wide, 140 nm high waveguide.

5.3. Nanobeam Waveguide Laser Suppression

Nano-beam waveguides have been previously shown to support two orthogonal transverse electric field modes (see chapter 4), referred to as TE_x and TE_y, with the electric field aligned parallel and perpendicular to the waveguide axis respectively. It is not clear however what fraction of a linearly polarised resonant excitation laser will couple to either of these modes. Simulations are therefore used in order to demonstrate that it should be possible to achieve strong laser rejection as a result of the orthogonal k-vectors of the excitation laser and the waveguide modes. Additionally, due to the different spatial profiles of the TE_x and TE_y modes, simulations are used to determine the optimum polarisation basis for the excitation laser to reduce coupling to the waveguide.

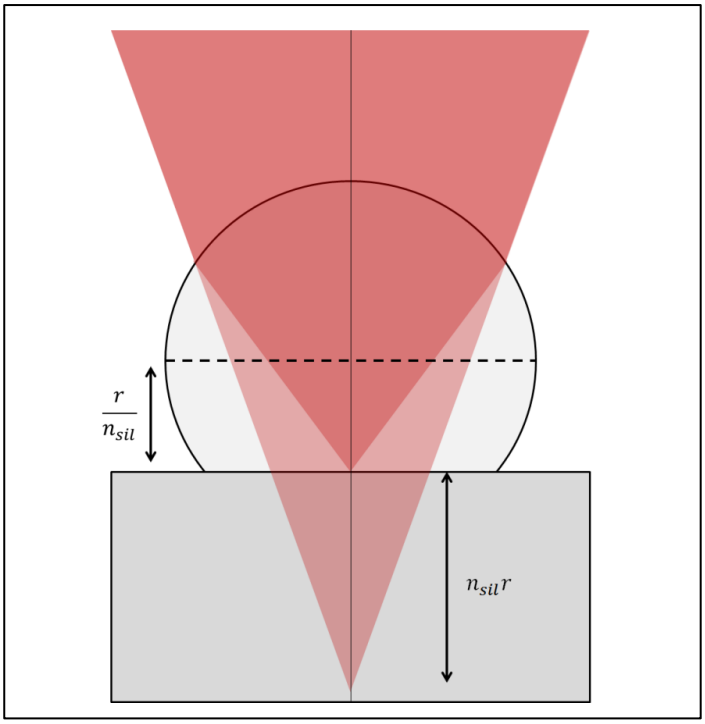

Figure 5-3 – Diagram depicting the apparent and real focal points of Weierstrass solid immersion lens where r is the radius of the lens and n_{sil} is the refractive index.

The excitation geometries used to excite a quantum dot in a waveguide with and without a solid immersion lens are both simulated for a photoluminescence setup with an objective lens with a numerical aperture of 0.5. For the 1 mm diameter ZrO_2 solid immersion lenses used, any objective lens with a numerical aperture greater than 0.35 would correspond to waist size of the excitation beam larger than the radius of the solid immersion lens at its equator (a height of $^{r}/_{n_{sil}}$ above the samples surface). This can be seen from simple trigonometry when examining Figure 5-3. Therefore when considering the case of the solid immersion lens, the excitation laser is modelled as coming from an effective numerical aperture of 2.13 ($N.A = n_{sil}sin(\theta)$) as it corresponds to the maximum numerical aperture possible.

Calculations are setup with field monitors positioned at several points along an infinitely long waveguide as shown in Figure 5-4. Due to the evanescent component of both the TE_x and TE_y modes (see chapter 1), the field monitors are set at twice the width and height of the waveguide to fully account for all contributions coupled to the waveguide. As a result of the finite spot size of the focused beam, and scatter from surfaces of the waveguide, monitors positioned close to the focal point experience an increased flux from scattered light which is not coupled to a waveguide mode. Flux monitors are therefore positioned up to 9 µm from the focal point at a spacing of 0.5 µm to determine

the fraction of power coupled to the waveguide at an infinite distance from the excitation spot.

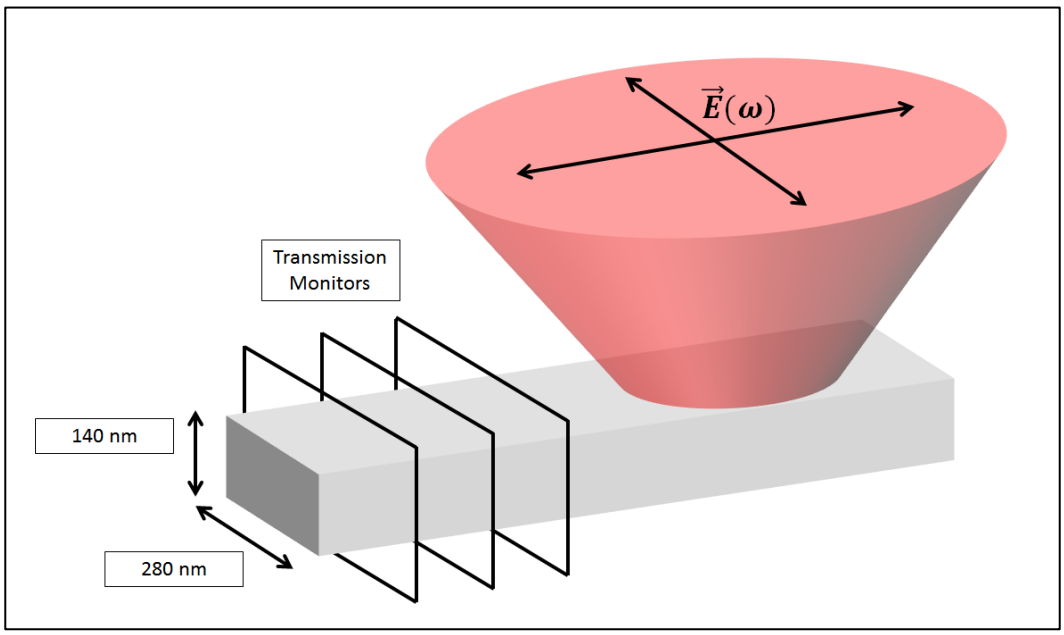

Figure 5-4 – Depiction of simulation to determine the fraction of excitation power coupled to the waveguide using flux monitors at incremental distances away from the excitation spot. The polarisation of the excitation spot is changed between parallel and perpendicular with respect to the waveguide length.

For all cases considered, the percentage of the power coupled to the waveguide is presented in Figure 5-5. It can be readily seen that for both with and without the solid immersion lens, the intensity of the light coupled to the waveguide is calculated to fluctuate in close proximity to the excitation spot. This is attributed to scattered laser light passing through the exaggerated flux monitors and is seen to fall off quickly a short distance from the excitation spot. When no solid immersion lens is used, the coupled power to the waveguide mode is shown to be relatively insensitive to the polarisation of the excitation source. For the numerical aperture of 0.5 modelled, it is expected that less than 10^{-4} % of the excitation power used would couple to the waveguide mode. This low coupling rate is expected given the lack of overlap between the incident electric field and the supported waveguide modes.

When modelling the solid immersion lens, the results of the coupled power to the waveguide suggest a strong dependence on the polarisation basis of the excitation laser. When the electric field is polarised parallel to the waveguide length, the coupled power is approximately 10^{-4} % of the excitation power, agreeing well with values calculated without a solid immersion lens. The coupled power is shown to increase significantly to

2×10^{-3} % when the electric field is rotated perpendicular to the waveguide axis. This is attributed to the significant reduction in the excitation spot size which increases the overlap of the electric field with the fundamental TE_Y waveguide mode.

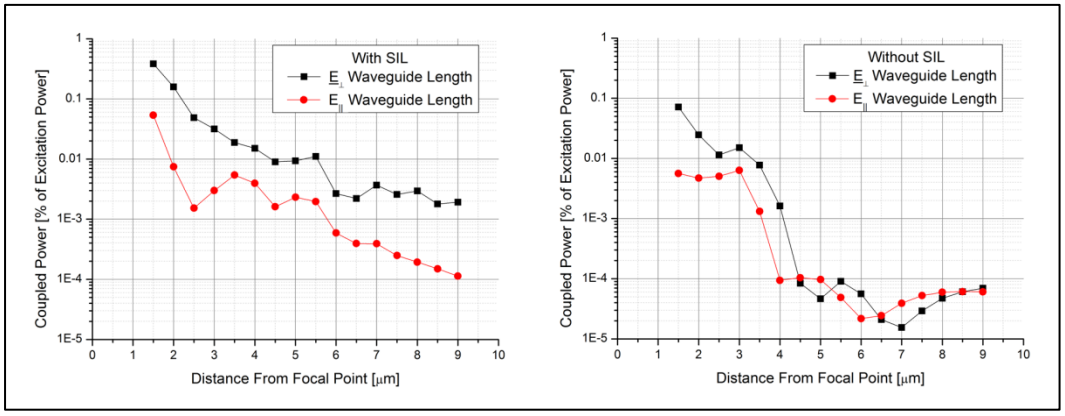

Figure 5-5 – Coupled power into the waveguide modes for an excitation beam linearly polarised parallel and perpendicular to the waveguide length at a wavelength of 925 nm. (left) Power coupled when the waveguide is positioned under a ZrO_2 (n=2.13) solid immersion lens with an effective numerical aperture of 2.13. (right) Power coupled for an objective lens with a numerical aperture of 0.5.

Based on these simulations, it is expected that using a solid immersion lens, and exciting with the laser polarised along the length of the waveguide, a similar laser rejection ratio should be achievable as if no solid immersion lens had been used for the same excitation power. As the power density of the excitation spot is increased by approximately 4.5 when using a solid immersion lens, it should be possible to use lower excitation powers to achieve the same signal intensity. Therefore, the total power coupled to the waveguide when using the solid immersion lens is expected to be 4.5 times lower than would have been without using a solid immersion lens.

5.4. Optical Measurements

The waveguides used in this work were fabricated at random locations on the sample. Therefore a relatively high quantum dot density (~ 10^9 QD's cm^{-2}) was used to ensure a sufficient number of randomly located quantum dots were positioned within the waveguides. Excitation of quantum dots was performed near the end of the waveguide, as shown in Figure 5-2, far away from the out-coupler. Initial measurements used above bandgap excitation to examine the spectral properties of several quantum dots located in the waveguide. This information is used to determine the relative location of the quantum dots as the intensity of the observed photoluminescence at a fixed power varies

with the excitation location. Additionally, it enabled measurements of the observed spectrum to determine the exciton transition energy.

Initial attempts to observe resonance fluorescence of a quantum dot were unsuccessful, despite clear evidence using above bandgap excitation that the resonant laser was tuned to the quantum dot transition energy. Similar affects are reported by others which show that very few quantum dots inherently exhibit resonance fluorescence (as low as 1 in 50 for QD's far below the surface [11]). As quantum dots are seen to interact strongly with the solid state environment, it is difficult to be sure of the exact mechanism preventing resonance fluorescence. It is known however that quantum dots are prone to spectral diffusion and blinking due to fluctuations in the local electrostatic environment [24][25]. The cause of these effects for quantum dots in the bulk semiconductor is attributed to the strong degree of anisotropy in the wetting layer, resulting in deep carrier traps [26]. For quantum dots in etched photonic structures, these effects are expected to be pronounced due to roughening of the surface [27], and we note that spectral changes are also reported for quantum dots fabricated in nanobeam waveguides (see Chapter 4).

As a result of these charge traps, the quantum dot sees a continuous tunnelling of electrons and holes between itself and the wetting layer, reducing the time in which the quantum dot is initialised in to ground state. It has been shown however that the use of a weak non resonant laser can be used to re-initialise quantum dots in certain circumstances, enabling the observation of resonance fluorescence. This is explained as the generation of additional carriers which occupy local defect states which were otherwise perturbing the quantum dot. If the carrier relaxation rate into a deep level defect state is higher than the tunnelling rate from the quantum dot, charge fluctuations can be significantly reduced [28].

We therefore show that using a small amount of above bandgap excitation, such that a negligible photoluminescence contribution is detected, the local charge environment is stabilised and the quantum dot ground state is re-initialised enabling resonance fluorescence is observed. The observed fluorescence for various excitation regimes is shown as a function of the laser detuning from the exciton transition energy in Figure 5-6. The background noise, which is primarily attributed to the dark current of the APD, is shown to be at approximately 750 counts s^{-1} which is calculated by blocking the excitation paths of both the resonant and above band gap lasers. When the above bandgap excitation is unblocked, a small contribution of approximately 300 counts s^{-1} is

measured on-top of the background signal. This represents a weak photoluminescence signal generated from the quantum dot indicating the transition is optically active.

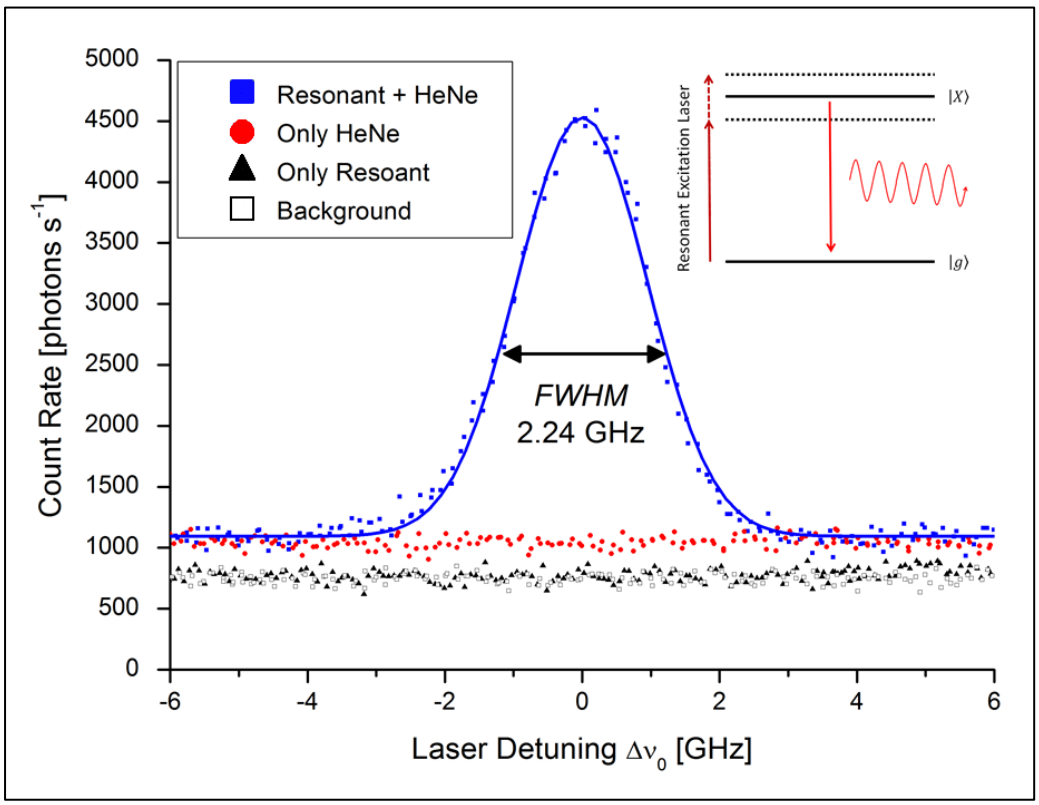

Figure 5-6 – Observed resonance fluorescence for a quantum dot as a function of the excitation laser detuning. The background signal when both the above bandgap and resonant laser are blocked is shown (gray) to be ~ 750 photons s^{-1}, attributed to dark counts on the APD. Under above bandgap excitation only (red), a background level of ~ 1050 photons s^{-1} is measured resulting in ~ 300 photons s^{-1} due to photoluminescence. When only the resonant laser is incident with no above band gap stabilisation of the exciton ground state (black), a background of ~ 790 photons s^{-1} is measured, with 40 photons s^{-1} attributed to the resonant laser. The optically gated resonance fluorescence is shown (blue) to have a peak intensity of ~ 4590 photons s^{-1}, which corresponds to a background subtracted peak count rate of ~ 3500 photons s^{-1}.

When the above bandgap excitation laser is blocked again, and the resonant laser unblocked, a small increase of roughly 40 counts s^{-1} is measured on-top of the dark counts of the APD. This count rate agrees well with the expected laser coupling calculated in simulations of 10^{-4} % of the excitation power when accounting for the total collection efficiency of the system which is estimated to be 0.5 %[3]. A measurement of 40 counts per second corresponds to an excitation power of a few nW's, in close agreement with the excitation power used.

[3] Detection efficiency of 0.5 % is calculated from an estimations of; APD quantum efficiency (30 %), waveguide coupling (50 %), out-coupler (50 %), cubic beam splitter (50 %), total fibre coupling losses (50 %) and filtering through the monochromator (25 %).

When the above bandgap laser is unblocked again, and the quantum dot is simultaneously excited with the above bandgap and resonant laser, a clear resonance fluorescence peak is observed as a function of the laser detuning from the exciton transition energy. A peak count rate of more than 4500 counts s^{-1} is recorded, which corresponds to a background subtracted peak intensity of 3500 counts s^{-1}. This intensity corresponds to a resonance fluorescence signal nearly 90 times larger than the background scattered resonant laser. When including the contribution of above bandgap excitation, the ratio of the resonance fluorescence to the remaining background signal drops to a value slightly in excess of 10. It is expected that for a quantum dot in a waveguide with a more stable charge environment, the non-resonant excitation should not be needed.

The lineshape of the measured resonance fluorescence is well fit by a Gaussian peak, and a full width half maximum of 2.24 GHz is obtained. This corresponds to a coherence time of nearly 240 ps, significantly less than the lifetime of the quantum dot, as will be discussed shortly. As the calculation of the spectral linewidth from Figure 5-6 is determined by slowly scanning (t_{scan} > 10 s) the frequency of the resonant laser, charge fluctuations on time scales much shorter than the scanning rate of the laser will lead to spectral wandering of the exciton transition. This, in combination with pure dephasing, result in the inhomogeneous broadening of the exciton transition observed, resulting in the calculation of a low coherence time.

A lifetime measurement of the quantum dot was also performed using a pulsed Ti:Sp laser tuned into resonance with the wetting layer as discussed in Chapter 2. An APD with a time resolution of 400 ps is used in conjunction with a single photon counting module to record the arrival time of the photons with respect to the excitation pulses. The recorded data is normalised and shown in Figure 5-7 with a single exponential fitted, giving a lifetime of 1.2 ± 0.1 ns. This lifetime is in good agreement with typical values observed in both the bulk wafer and other nanophotonic structures for InGaAs quantum dots.

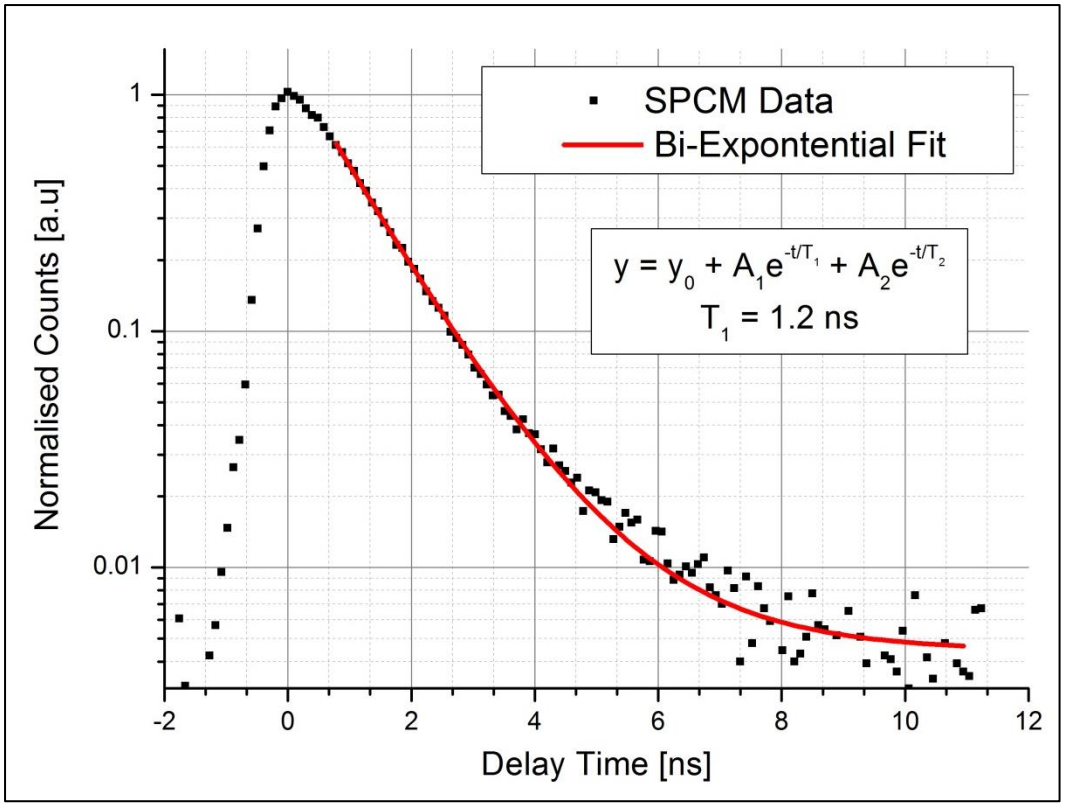

Figure 5-7 – Lifetime measurement of the quantum dot examined for resonance fluorescence

In the Fourier transform limit, the coherence time of the quantum dot is twice the radiative lifetime ($T_2 = 2T_1$). From the coherence time calculated from the linewidth measured in Figure 5-6, the ratio of the coherence time to the lifetime is roughly 10 times less than this limit ($T_2 : T_1 = 0.2 : 1$). The coherence time of the quantum dot is further studied by measuring the first order correlation function using a Michelson interferometer, with further details regarding the setup provided in Chapter 2. Measurements are performed in the low power regime for both above band gap and resonant excitation fixed at zero detuning from the exciton transition energy in order to reduce power and inhomogeneous broadening from induced fluctuations in the local charge environment. Low power measurements for the above bandgap laser were performed with the excitation laser set to half the power of saturation. For resonant excitation, the saturation power can be defined by the Rabi frequency (Ω) given as $^{1}/_{(T_1\sqrt[2]{2})} \approx \Omega_{sat}$ [19] with the low power regime defined as $\Omega < \Omega_{sat}$. An excitation power of ~ 0.6 Ω_{sat} is therefore used. We distinguish this low power regime from the Heitler regime which requires ultra-low excitation powers of $\Omega \ll \Omega_{sat}$.

The measured interference visibility as a function of the relative path delay for both the above bandgap and resonant excitation measurements of the coherence time are shown in Figure 5-8. A coherence time for above bandgap excitation is obtained of 154 ± 5 ps, which is less than the inferred coherence time from the linewidth measured in Figure 5-6. It is not surprising that the coherence length is shorter during above bandgap excitation than that inferred from the linewidth obtained by scanning the resonant laser as it is well established that the presence of above bandgap excitation induces a fluctuating charge environment for the quantum dot. The reduced coherence time can be explained by an increase pure dephasing due to a less stable charge environment under above bandgap excitation, as well as an increased contribution of spectral wondering.

Under resonant excitation, with a fixed zero detuning from the central exciton transition energy, the coherence time is shown to increase to 640 ± 40 ps. This is significantly higher than the 240 ps coherence time determined from the linewidth in Figure 5-6, suggesting that spectral wandering is especially pronounced for the quantum dot studied. As the shorter coherence length of 240 ps was obtained when scanning the resonant laser slowly across the exciton transition, the integrated signal includes contributions from the inhomogeneous linewidth, where the quantum dot transition energy is perturbed from the homogeneous value. By fixing the wavelength of the resonant laser at the peak intensity, which corresponds to the peak of the homogeneous transition, when the exciton transition wanders from this value due to the fluctuating environment, it is no longer resonant with the laser and no photons are produced. The photons which are produced are therefore more coherent as a result. The ratio of the coherence time to the lifetime under resonant excitation, with a constant zero detuning form the exciton transition energy, is thus determined to be $T_2 : T_1 \approx 0.5 : 1$ and represents an increase relative to the coherence time calculated using above bandgap excitation of more than four times.

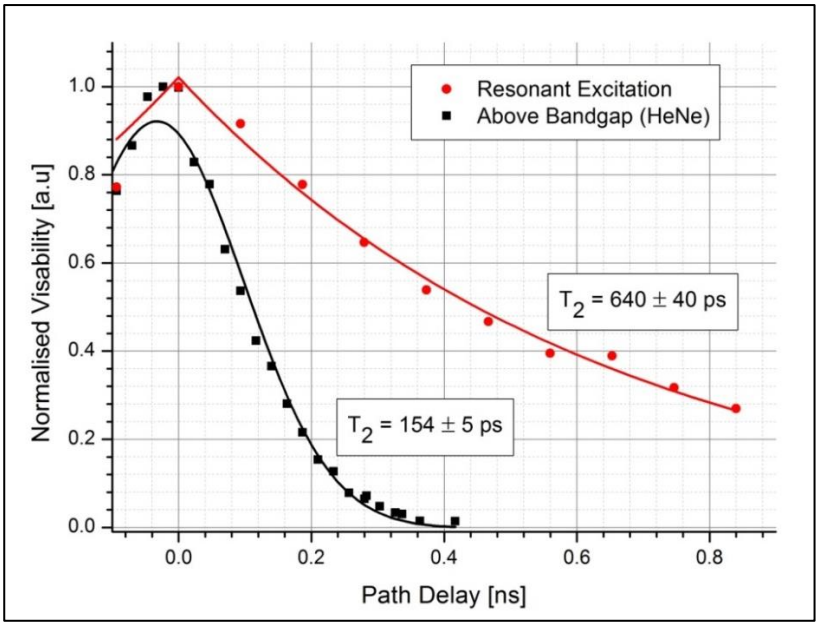

Figure 5-8 – Coherence times measured for the quantum dot in the waveguide using above bandgap excitation (black) and resonant excitation (red) via a Michelson interferometer. Coherence times are fitted to a single exponential which calculate coherence times of 154 ps and 640 ps for the above band gap and resonant excitation respectively.

The coherence times measured using the Michelson interferometer correspond to the total coherence times of photons emitted from the quantum dot. The values obtained for the coherence time of emitted photons, of 640 ps and 154 ps for resonant and above bandgap excitation respectively, in combination with the measured lifetime, 1.2 ns, can be used to determine the coherent ratio, given by $^{T_2}/_{2T_1}$. As discussed in section 5, in the Fourier transform limit, where there is no pure dephasing, $T_2 = 2T_1$, and the coherent ratio would be equal to 1. For the case of above bandgap excitation this ratio is calculated to be ~ 0.06, indicating de-coherence the result of pure dephasing on timescales much shorter than the lifetime ($T_2{}^* = 165\,ps$). Under resonant excitation, the coherent ratio is calculated to be significantly higher at ~ 27 %, and the pure dephasing time is increased to greater than 870 ps, attributed to the reduced number of carriers created as a result of the lower power of the above bandgap excitation.

In order to confirm the single photon characteristics, the auto-correlation function is measured using the Hanbury – Brown – Twiss setup described in Chapter 2. Measurements are performed for both above bandgap and resonant excitation at near saturation intensities. As the auto-correlation measurement is sensitive to the background signal levels, the background signal intensities are recorded so that the data can properly normalised. For the above bandgap excitation, the background is recorded by offsetting the monochromator by a small amount from the resonant transition. The

signal ratio relative to the background count rate is observed to be 0.89[4]. Under resonant excitation, this ratio is calculated to be 0.82 and is determined by detuning the resonant laser from the quantum dot transition by several GHz[4]. The background is then subtracted from the measured coincidence counts as described in reference [29], and the normalised auto-correlation measurements are shown for the above bandgap and resonant excitation in Figure 5-9.

A clear dip at a zero time delay for the above bandgap excitation shows the strongly anti-bunched nature of the photons and confirms the emission is from a single photon source. The lifetime extracted from the auto-correlation function also agrees well with that calculated from direct measurements of the lifetime shown in Figure 5-7. A similar dip at zero time delays is seen under resonant excitation confirming both that measurements are performed with strong suppression of the resonant laser, and that the resonance fluorescence is an anti-bunched single photon source. The peaks however at times close to a zero time delay are intrinsic of bunched photon emission, and are fitted with an exponential decay with a corresponding decay time of 4 ns. In an attempt to explain the presence of this bunched photon statistics, three mechanisms are identified which could be responsible; Rabi oscillations, the above bandgap excitation, and spectral diffusion.

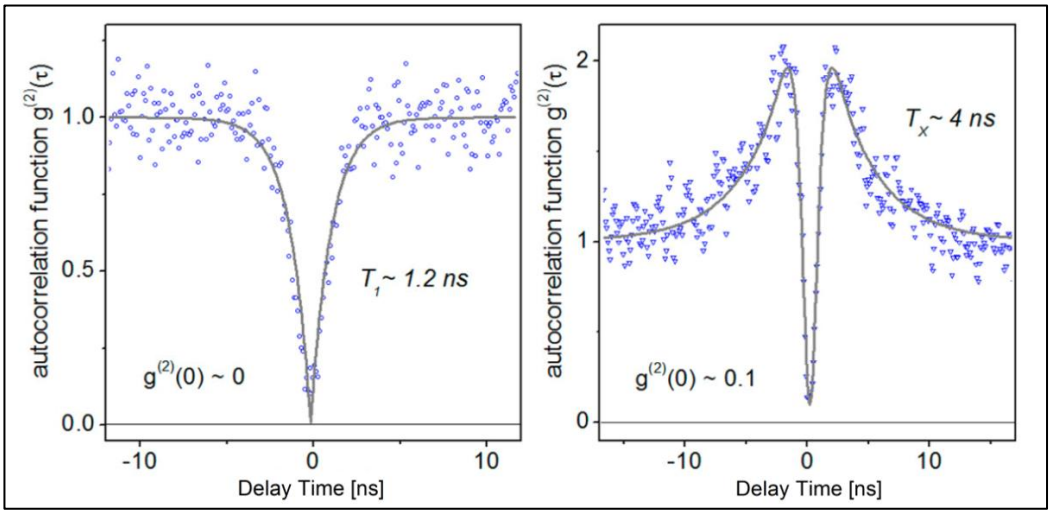

Figure 5-9 – Auto correlation measurements for above bandgap excitation (left) and resonant excitation (right) at near saturation intensities. A clear dip at t=0 is present under both excitation regimes confirming single photon emission. The bunched emission under resonant excitation as shown by the increased correlation measurement exhibits exponential decay with a decay time of 4 ns.

[4] The signal to noise ratio is calculated as $\rho = \frac{S}{S+B}$ where S is the actual signal intensity of the quantum dot and B is the background count rate due to all other sources.

Under high resonant excitation powers, the exciton state can be coherently rotated around the bloch sphere between the ground and excited stated. As a result the auto-correlation function includes an exponential decaying oscillating term related to the Rabi frequency (Ω) given by Equation 5-3 [30]. As the resolution of our system is limited to 400 ps due to the time response of the APD, it may appear as a bunching in the auto-correlation function. However, these Rabi oscillations are not considered to introduce a significant bunching affect for excitation powers below the saturation power, corresponding to a Rabi frequency of $\Omega_{sat} = 0.6$ GHz [30]. As the excitation power used corresponds to a Rabi frequency of 0.5 GHz, it is concluded that this is not the cause of the observed bunching seen Figure 5-9.

$$g^{(2)}(t) = 1 - exp(-\eta|t|)\left\{\cos(\mu|t|) + \frac{\eta}{\mu}\sin(\mu|t|)\right\} \quad (5.3)$$

$$\eta = \frac{\frac{1}{T_1}+\frac{1}{T_2}}{2} \; ; \; \mu = \sqrt{\Omega^2 + \left(\frac{1}{T_1} - \frac{1}{T_2}\right)^2}$$

Equation 5-3 – auto-correlation function where 't' represents the relative time delay between coincidences, Ω is the Rabi frequency given by $\sqrt{\frac{P}{T_1 T_2 P_0}}$ where T_1 and T_2 are the exciton lifetime and coherence time respectively and P and P_0 are is excitation power and saturation power.

As the quantum dot is initialised using above bandgap excitation in order to realise resonance fluorescence, the capture and release of carriers from the local environment represents an additional mechanism for excitation. It is reported however that the capture and release of carriers due to the optical gate affect typically occurs on microsecond time scales [31]. It is therefore unlikely that the bunching which occurs on a 4 ns time scale is attributed to it to the presence of charge traps.

We therefore concluded that this bunching is the result of instabilities caused by spectral diffusion and that the 4 ns decay constant represents the fluctuation time of the homogeneous exciton transition over the observed inhomogeneous linewidth. This can be seen more clearly by considering the Fourier transformed linewidths, calculated from the coherence times measured of 154 ps and 640 ps, which correspond to linewidths of 3.4 GHz and 0.5 GHz respectively. It can be seen that a small shift of the transition frequency for the 0.5 GHz wide homogeneous linewidth can result in the exciton transition being tuned off resonance with the excitation laser, as shown in Figure 5-10. This results in the emission of single photons in packets corresponding to when the quantum dot is on and off resonance with the excitation laser.

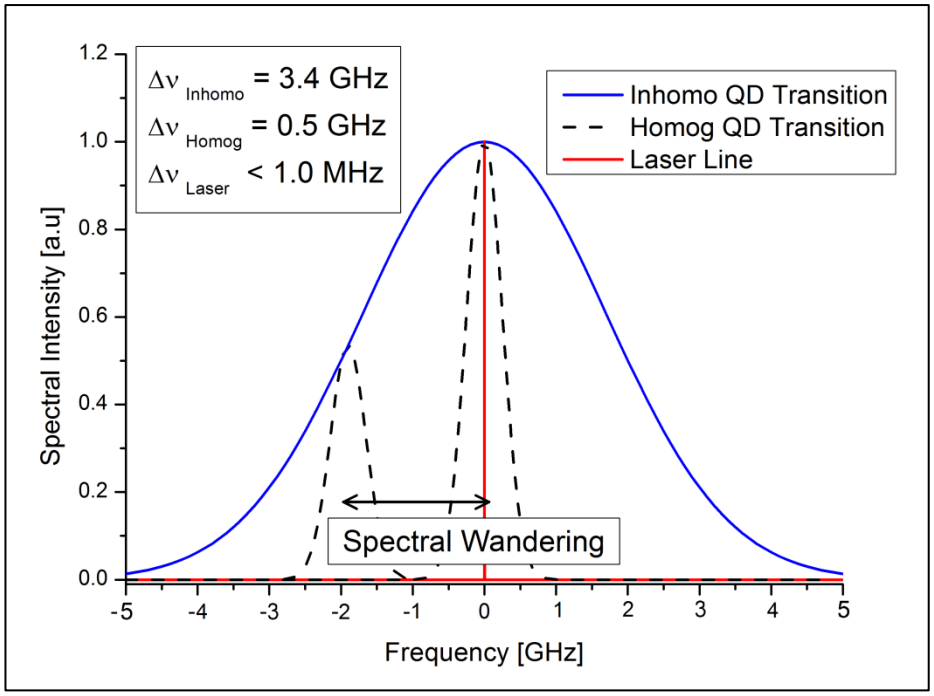

Figure 5-10 – Depiction of spectral wondering of the homogeneous linewidth ($\boldsymbol{\Delta\nu = 0.5\ GHz}$) which results in the observation of a broader inhomogeneous linewidth ($\boldsymbol{\Delta\nu = 3.4\ GHz}$). A small shift in the transition energy of the homogeneous line is shown to result in the detune the resonant excitation.

5.5. Conclusions

It has been shown that under resonant excitation, the coherence of the quantum dot can be improved by more than four times with respect to that measured under above bandgap excitation. This represents a potentially significant increase in the coherent ratio of photons generated from 6 % to 27 %. Furthermore, the demonstration of resonance fluorescence emitting efficiently into a photonic structure has been achieved whilst maintain a high degree of suppression of the resonant laser. This therefore represents a significant achievement for the realisation of coherent single photons within nanophotonic structures.

The interactions of the quantum dot with its solid state environment are shown to be partially overcome with the use of a resonant laser, although it is clear much work is still needed to better understand and control these interactions.

5.6. References

[1] C. Santori, D. Fattal, J. Vucković, G. S. Solomon, and Y. Yamamoto, "Indistinguishable photons from a single-photon device.," *Nature*, vol. 419, no. 6907, pp. 594–7, Oct. 2002.

[2] A. Crespi, R. Ramponi, R. Osellame, L. Sansoni, I. Bongioanni, F. Sciarrino, G. Vallone, and P. Mataloni, "Integrated photonic quantum gates for polarization qubits.," *Nat. Commun.*, vol. 2, p. 566, 2011.

[3] B. Lounis and W. E. Moerner, "Single photons on demand from a single molecule at room temperature," *Nature*, vol. 407, no. 6803, pp. 491–493, Sep. 2000.

[4] A. Beveratos, S. Kühn, R. Brouri, T. Gacoin, J. P. Poizat, and P. Grangier, "Room temperature stable single-photon source," *Eur. Phys. J. D*, vol. 18, no. 2, pp. 191–196, 2002.

[5] F. Jelezko, A. Volkmer, I. Popa, K. Rebane, and J. Wrachtrup, "Coherence length of photons from a single quantum system," *Phys. Rev. A*, vol. 67, no. 4, p. 41802, Apr. 2003.

[6] I. J. Luxmoore, N. A. Wasley, A. J. Ramsay, A. C. T. Thijssen, R. Oulton, M. Hugues, S. Kasture, V. G. Achanta, A. M. Fox, and M. S. Skolnick, "Interfacing Spins in an InGaAs Quantum Dot to a Semiconductor Waveguide Circuit Using Emitted Photons," *Phys. Rev. Lett.*, vol. 110, no. 3, p. 37402, Jan. 2013.

[7] M. N. Makhonin, J. E. Dixon, R. J. Coles, B. Royall, I. J. Luxmoore, E. Clarke, M. Hugues, M. S. Skolnick, and A. M. Fox, "Waveguide Coupled Resonance Fluorescence from On-Chip Quantum Emitter," 2014.

[8] J. L. Skinner and D. Hsu, "Pure Dephasing of a Two-Level System," *J . Phys. Chem. Spectrosc. Excit. Dyn. Condens. Mol. Syst. J. J. Phys. Chem*, vol. 90, no. 90, pp. 4931–4938, 1986.

[9] P. Lodahl, S. Mahmoodian, and S. Stobbe, "Interfacing single photons and single quantum dots with photonic nanostructures," *Rev. Mod. Phys.*, vol. 87, no. 2, pp. 347–400, 2015.

[10] M. E. Reimer, G. Bulgarini, A. Fognini, R. W. Heeres, B. J. Witek, M. A. M.

Versteegh, A. Rubino, T. Braun, D. Dalacu, J. Lapointe, P. J. Poole, and V. Zwiller, "Overcoming power broadening of the quantum dot emission in a pure wurtzite nanowire," vol. 195316, pp. 1–9, 2016.

[11] H. S. Nguyen, G. Sallen, C. Voisin, P. Roussignol, C. Diederichs, and G. Cassabois, "Optically Gated Resonant Emission of Single Quantum Dots," *Phys. Rev. Lett.*, vol. 108, no. 5, p. 57401, Jan. 2012.

[12] S. Ates, S. Ulrich, S. Reitzenstein, A. Löffler, A. Forchel, and P. Michler, "Post-Selected Indistinguishable Photons from the Resonance Fluorescence of a Single Quantum Dot in a Microcavity," *Phys. Rev. Lett.*, vol. 103, no. 16, pp. 1–4, Oct. 2009.

[13] L. Besombes, J. Baumberg, and J. Motohisa, "Coherent Spectroscopy of Optically Gated Charged Single InGaAs Quantum Dots," *Phys. Rev. Lett.*, vol. 90, no. 25, p. 257402, Jun. 2003.

[14] D. J. Diestler and H. D. Ladouceur, "An alternative derivation of the Wigner-Weisskopf approximation," *Opt. Commun.*, vol. 20, no. 1, pp. 6–9, 1977.

[15] W. Heitler, *The Quantum Theory of Radiation (Dover Books on Physics)*. Dover Publications, 2003.

[16] Y. Zhao, "Resonance Fluorescence and Electron Spin in Semiconductor Quantum Dots," *Diss. Submitt. to Comb. Fac. Nat. Sci. Math. Ruperto–Carola-University Heidelberg. Ger.*, 2009.

[17] C.-Y. Lu, Y. Zhao, A. N. Vamivakas, C. Matthiesen, S. Fält, A. Badolato, and M. Atatüre, "Direct Measurement of Quantum Dot Spin Dynamics using Time-Resolved Resonance Fluorescence," *Phys. Rev. B*, vol. 81, p. 35332, 2009.

[18] A. Muller, E. B. Flagg, P. Bianucci, X. Y. Wang, D. G. Deppe, W. Ma, J. Zhang, G. J. Salamo, M. Xiao, and C. K. Shih, "Resonance Fluorescence from a Coherently Driven Semiconductor Quantum Dot in a Cavity," *Phys. Rev. Lett.*, vol. 99, no. 18, pp. 2–5, Nov. 2007.

[19] C. Matthiesen, A. Vamivakas, and M. Atatüre, "Subnatural Linewidth Single Photons from a Quantum Dot," *Phys. Rev. Lett.*, vol. 108, no. 9, pp. 1–4, Feb.

2012.

[20] M. N. Makhonin, J. E. Dixon, R. J. Coles, B. Royall, I. J. Luxmoore, E. Clarke, M. Hugues, M. S. Skolnick, and A. M. Fox, “Waveguide coupled resonance fluorescence from on-chip quantum emitter,” *Nano Lett.*, vol. 14, no. 12, pp. 6997–7002, 2014.

[21] G. Reithmaier, S. Lichtmannecker, T. Reichert, P. Hasch, K. Müller, M. Bichler, R. Gross, and J. J. Finley, “On-chip time resolved detection of quantum dot emission using integrated superconducting single photon detectors.,” *Sci. Rep.*, vol. 3, p. 1901, 2013.

[22] S. Yadav, G. Kaur, C. Technology, and U. Pradesh, “A PLANATIC POINT ANALYSIS OF SOLID IMMERSION L ENS,” vol. 8, no. 3, pp. 385–396, 2015.

[23] C. Tonin, R. Hostein, V. Voliotis, R. Grousson, A. Lemaitre, and A. Martinez, “Polarization properties of excitonic qubits in single self-assembled quantum dots,” *Phys. Rev. B*, vol. 85, no. 15, pp. 1–9, Apr. 2012.

[24] R. G. Neuhauser, K. T. Shimizu, W. K. Woo, S. A. Empedocles, and M. G. Bawendi, “Correlation between Fluorescence Intermittency and Spectral Diffusion,” pp. 3301–3304, 2000.

[25] A. Reinhard, T. Volz, M. Winger, A. Badolato, K. J. Hennessy, E. L. Hu, and A. Imamoğlu, “Strongly correlated photons on a chip,” *Nat. Photonics*, vol. 6, no. 2, pp. 93–96, 2011.

[26] A. Majumdar, E. D. Kim, and J. Vuˇ, “Effect of photogenerated carriers on the spectral diffusion of a quantum dot coupled to a photonic crystal cavity,” vol. 195304, pp. 1–6, 2011.

[27] A. Majumdar, A. Faraon, E. D. Kim, D. Englund, H. Kim, P. Petroff, and J. Vučković, “Linewidth broadening of a quantum dot coupled to an off-resonant cavity,” *Phys. Rev. B - Condens. Matter Mater. Phys.*, vol. 82, no. 4, pp. 1–5, 2010.

[28] H. S. Nguyen, G. Sallen, C. Voisin, C. Diederichs, and G. Cassabois, “Supplemental material for: Optically-gated resonant emission in single quantum dots,” no. 2, pp. 2–4, 2011.

[29] R. Brouri, A. Beveratos, J.-P. Poizat, and P. Grangier, “Photon antibunching in the fluorescence of individual color centers in diamond,” *Opt. Lett.*, vol. 25, no. 17, p. 1294, 2000.

[30] E. B. Flagg, A. Muller, J. W. Robertson, S. Founta, D. G. Deppe, M. Xiao, W. Ma, G. J. Salamo, and C. K. Shih, “Resonantly driven coherent oscillations in a solid-state quantum emitter,” *Nat. Phys.*, vol. 5, no. 3, pp. 203–207, Jan. 2009.

[31] H. S. Nguyen, G. Sallen, C. Voisin, P. Roussignol, C. Diederichs, and G. Cassabois, “Optically gated resonant emission of single quantum dots.,” *Phys. Rev. Lett.*, vol. 108, no. 5, p. 57401, Feb. 2012.

6. Summary and outlook

This section provides a summary of the work presented in the experimental sections, Chapter 3, 4 & 5 along with key results. Following this, related and ongoing research efforts are briefly discussed.

6.1. Chapter Overview

6.1.1. Dot Registration

Quantum dots provide a scalable source of single photons for nanophotonic structures. However there remain significant technological challenges to achieve some of the essential technological prerequisites, including site controlled growth and deterministic fabrication of photonic structures with quantum dots at optimal locations. Much of the current research is primarily focused on realising scalable, site controlled growth, using lithographic processes to introduce nucleation sites prior to the MBE or MOCVD. The work presented in Chapter 3 builds on the technique of dot registration, where the relative position between a quantum dot and a pre-fabricated marker is determined using a two channel scanning micro-photoluminescence setup. It is shown that aberration free imaging of the sample surface is possible through a super spherical solid immersion lens, which can be used to increase the accuracy of the dot registration technique. Additionally, it was shown that the use of a temporary SiO_2 hard mask can be used to protect the surface of the sample during the registration process without affecting the optical properties of the quantum dots. Under optimal conditions, the minimum FWHM of the measured relative position of the quantum dot was 8.53 nm. The use of solid immersion lens enhanced dot registration is therefore shown to result in the most precise measurements of the relative position of a quantum dot to date.

6.1.2. Deterministic Fabrication

In order to realise scalable photonic circuits, either using nucleated growth of quantum dots or dot registration, the accuracy of the chosen technique must be sufficient that it is at least statistically favourable for a quantum dot to be ideally located within the photonic structure. Additionally, the performance of many photonic components is highly dependent on the spectral properties of the photons emitted from the embedded quantum dots. It is therefore important that the fabrication processes does not significantly affect the spectral properties of the quantum dot.

In Chapter 4, the positional accuracy of the solid immersion lens enhanced dot registration processes is confirmed via two independent methods. Firstly, the fabrication of additional re-registration markers are used to confirm the registration accuracy by repeating the registration processes. The repeated registration process uses new markers which have been deterministically positioned a set distance from the previously calculated quantum dot location. A minimum displacement of 13.7 nm is observed between the re-registered positions relative to the original registered position. Secondly, the positional accuracy of the dot registration processes is further confirmed by deterministically positioning a quantum dot at a 'C point' of a nanobeam waveguide so as to couple circularly polarised light, which is then placed in a magnetic field. The contrast of the two spectrally resolved spin states measured out of the two outcouplers agrees well with predicted values via FDTD simulations with a 15 nm error in the position of the quantum dot. Inaccuracy in the dot registration technique is primarily attributed to instabilities in the EBL process, which were found to result in an average positional error of 15.1 nm between sequential fabrication processes.

Throughout the fabrication processes used to confirm the positional accuracy of dot registration, the spectral properties of the quantum dots were recorded. It was shown that in the majority of cases, the spectral peak used to register the position of the quantum dot was still present after fabrication steps. Further discussion regarding any observed changes in the spectral properties is presented in section 6.2 along with other future work. The ability to selectively embed a quantum dot, based on its spectral properties, within a photonic structure, with an accuracy of 13.7 nm at best, has therefore been demonstrated by solid immersion lens enhanced dot registration.

6.1.3. Resonance Fluorescence

Quantum dots are an ideal source of single photons which can be efficiently coupled into photonic circuits, with up to 95% and 70% efficiency reported for linearly and circularly polarised light respectively [1]. This ability to directly embed quantum dots within nanophotonic devices is key to the potential scalability which may be achieved. Unfortunately, the strong interaction which quantum dots exhibit with their solid state environment results in significantly reduced coherence times. In attempts to reduce fluctuations in the solid state environment, and therefore increase the coherence times, direct excitation of carriers in the wetting layer, or quasi-resonant excitation of the quantum dot detuned by one LO phonon are widely investigated [2]. More recently,

resonant excitation has been demonstrated which has been shown to significantly improve the coherence times of emitted photons, although novel excitation and collection geometries are required to filter the resonant excitation laser [3][4]. In Chapter 5, it is shown that for a quantum dot in a nanobeam waveguide, the waveguide can be used to efficiently filter the resonant laser from the resonantly emitted photons due to the small overlap between k-vectors of the excitation laser and the waveguide mode. Simulations of exciting the waveguide orthogonally to the waveguide propagation direction were found to be in good agreement with experimental results, which predicted strong laser suppression, with only 10^{-4} % of the incident laser coupled into the waveguide. The use of resonant excitation was shown to result in a signal to laser ratio slightly in excess of 10:1, whilst simultaneously resulting in more than a fourfold increase in the coherence length of the emitted photons than compared to using above bandgap excitation. This therefore represents the first demonstration of coherence enhanced single photons efficiently coupled to a nanophotonic structure.

6.2. Outlook

Work presented in this thesis, as well concurrent work by others within the LDSD group has demonstrated significant advances in the field of nanophotonic circuits. This has in turn resulting in the exploration of additional research paths, of which several are briefly discussed here.

6.2.1. In-Situ Lithography

The process of dot registration, whilst a significant achievement, has demonstrated that the sequential processing steps required in order to carry out dot registration inevitably result in compounding errors. Based on the work by Senellart [5], where in-situ optical lithography was demonstrated using a negative photoresist to fabricate micropillars around a quantum dot with an accuracy of 50 nm, preliminary work has been undertaken to demonstrate the fabrication of EBL alignment markers around a suitable quantum dot. It is envisaged that a sample spin coated in photoresist may be studied at cryogenic temperatures in order to locate a suitable quantum dot through measurements of its photoluminescence. Then, using a lower wavelength laser at high powers, the photoresist surrounding the quantum dot can be exposed, leaving a pattern in the developed resist which can be used to align the wright field for conventional electron beam lithography.

Preliminary work, carried out during this thesis, has already been performed to demonstrate both the feasibility of using photoresists at cryogenic temperatures as well as the ability to use two independent lasers to measure the photoluminescence from quantum dots and expose the resist in a desired pattern. In order to prevent the strain due to thermal contraction deforming and shattering the photoresist, it was necessary to fabricate discretised areas of photoresist. Images of two separate samples, one entirely coated in photoresist and the other with discretised regions, which have been thermally cycled using the liquid helium flow cryostat, are shown in Figure 6-1.

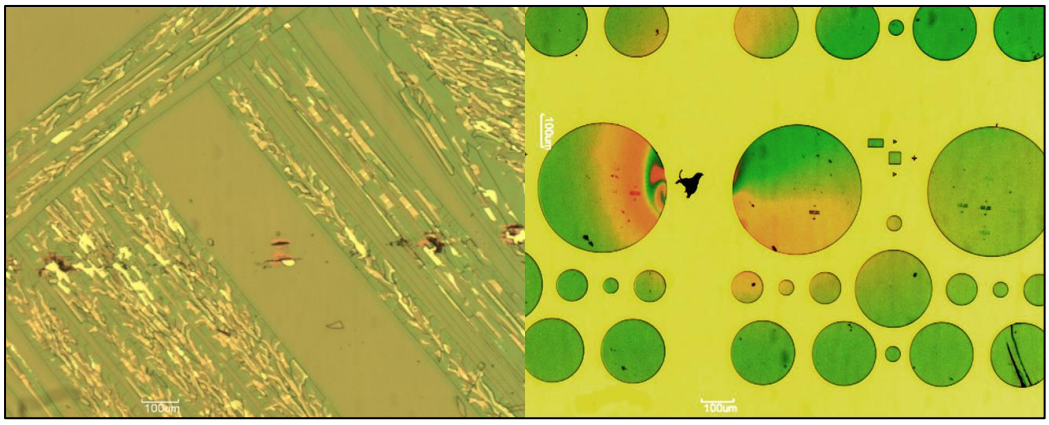

*Figure 6-1 – Optical images of S1805 photo resist after thermal cycling to ~**4k** using a liquid helium flow cryostat. (left) Significant cracking and flaking of the photoresist when the entire sample is spin coated due to thermal strain. (right) Intact photoresist disks which were free to expand and contract during thermal cycling.*

In order to expose the photoresist, sufficient energy needs to be absorbed in order to break chemical bonds, affecting its solubility to a given solvent. As the absorbed energy of the photoresist is strongly wavelength dependent, two colour excitation enables the photoluminescence spectrum to be observed through the resist without significantly developing the resist in the area around the quantum dot. The use of a second, shorter wavelength laser, can then be used to develop specific areas of the surface in the desired pattern. For the preliminary work presented, an 808 nm diode laser is used to observe the photoluminescence spectrum from the quantum dots under the photoresist. A green diode laser with a wavelength of $\sim 500\, nm$ is used to expose the photoresist in the desired pattern near the quantum dots location. A recorded spectrum through the photoresist, as well as a developed pattern in the photoresist is shown in Figure 6-2.

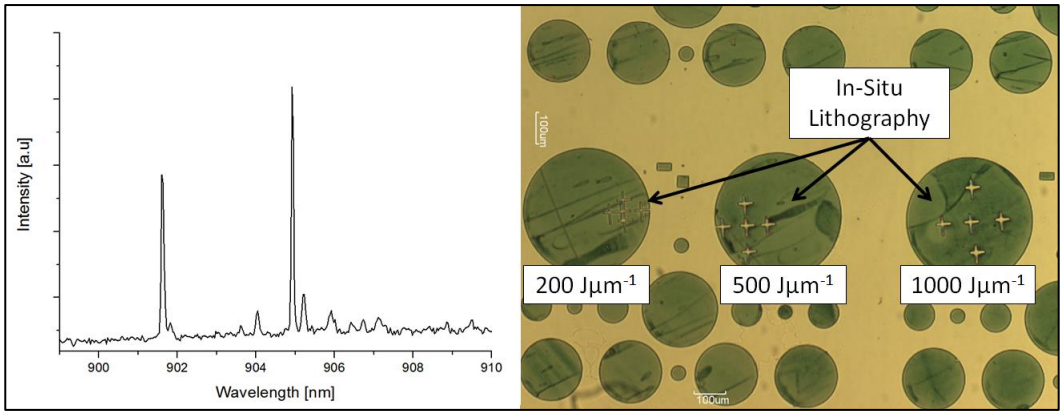

Figure 6-2 – (left) Spectrum of quantum dot observed through the S1805 photoresist, excited using an 808 nm diode laser. (right) Optical microscope image of developed photoresist after various asymmetric crosses have been patterned into the photoresist using a green diode laser.

6.2.2. Fabrication Induced Spectral Changes

It is known that quantum dots are sensitive to changes in their local environment, and as such, effects such as spectral wandering and blinking have been widely reported [6]. Typically, these unwanted characteristics are present as a result of a high defect density in the sample, or due to the close proximity of the quantum dot to a surface or material boundary. The fabrication steps following dot registration, which involved the fabrication re-registration markers or nanobeam waveguides, was therefore performed with the expectation that similar affects may manifest. Promisingly, for the technique of dot registration, it was observed that for successful deterministic fabrication steps, minimal change in spectral properties of the registered exciton transition was observed.

This however was not found to always be the case, with the appearance of new exciton transitions, as well as the disappearance of existing ones, observed for several quantum dots after the fabrication of additional structures. As a spectral comparison was needed to help locate and confirm the identity of individual quantum dots during the re-registration and nanobeam waveguide measurements, the changes to the spectral properties are well documented. An example of the unwanted spectral changes which were observed in several quantum dots is presented in Figure 6-3.

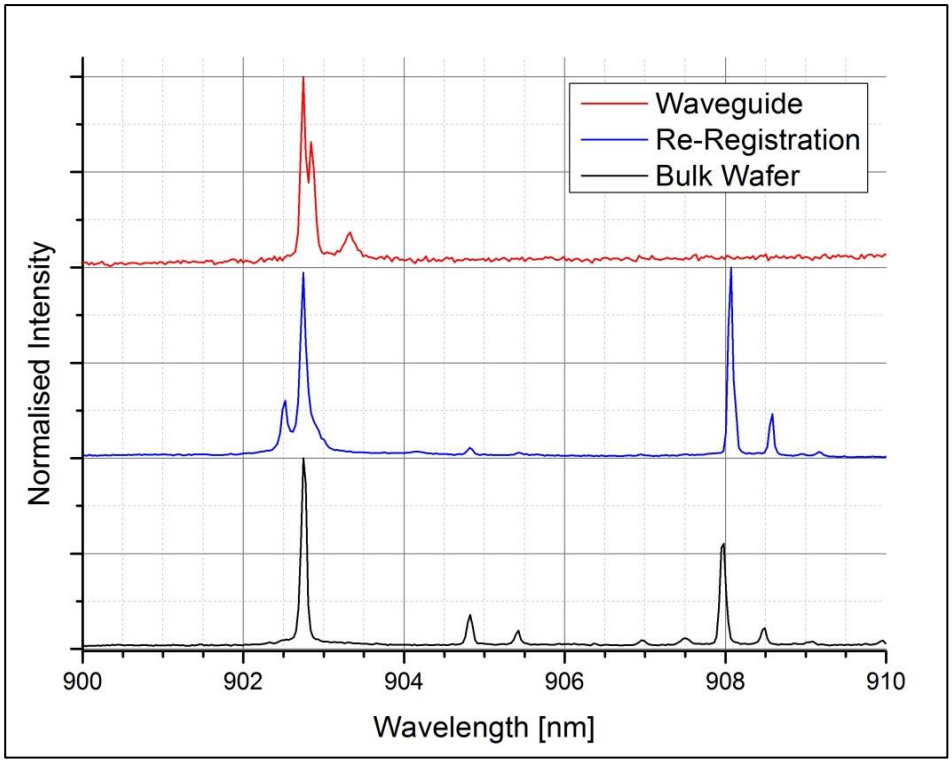

Figure 6-3 – Spectral comparison of a quantum dot at the three stages used to investigate the technique of solid immersion lens enhanced dot registration; initial registration (black), re-registration (blue) and embedded within a nanobeam waveguide (red)

It can be seen that as a result of the fabrication of additional re-registration markers, a second transition, not present in the initial registered spectrum, appears at 902.5 nm. Spectral changes are again observed as a result of the fabrication of the nanobeam waveguide, which shows the complete disappearance of the two exciton transitions located at 908 nm and 908.5 nm. Whilst effects of this type may be explained as a result of the fabrication of the nanobeam waveguide, which may introduce charge traps at surfaces near the quantum dot, it is not obvious as to why the fabrication of re-registration markers at a distance of 5 µm from the quantum dot would result in such a significant change.

Initial thoughts are that defects, possibly due to sputtering of metal during the MBE growth, may result in a quantum dot that is sensitive to changes in the extended environment. Additionally, strain induced by thermal contraction may be affected by the removal of material over the micron scale distances considered here. These affects, as well as the influence of the fabrication processes, which make use of inductively coupled plasma etching and electron beam lithography, will likely warrant further investigation to determine the cause of the spectral changes observed.

6.2.3. Single mode diode waveguides

With dot registration and resonance fluorescence demonstrating that it is possible to realise a reliable source of single photons with enhanced coherence, the problem of how to tune two or more quantum dots into resonance with each other needs to be addressed before scalable photonic circuits may be realised. As a first step towards this, preliminary work examining the photoluminescence of quantum dots embedded in nanobeam waveguides fabricated from a 170 nm thick membrane P-I-N heterostructure has been investigated. A waterfall plot showing the observed photoluminescence as a function of the applied bias for a quantum dot in a 330 nm wide waveguide is shown in Figure 6-4. The observed photoluminescence is visible over a tuneable range of more than 2 nm, providing a broad spectral window for techniques such as dot registration to find multiple spectrally similar quantum dots.

It is hoped that through advanced wafer processing techniques, using multiple lithographic processes, that it may be possible to independently tune one or more quantum dot embedded within the same nanophotonic structure. Without this ability, scalable photonic circuits utilising multiple quantum dots tuned into resonance with each other will not be possible.

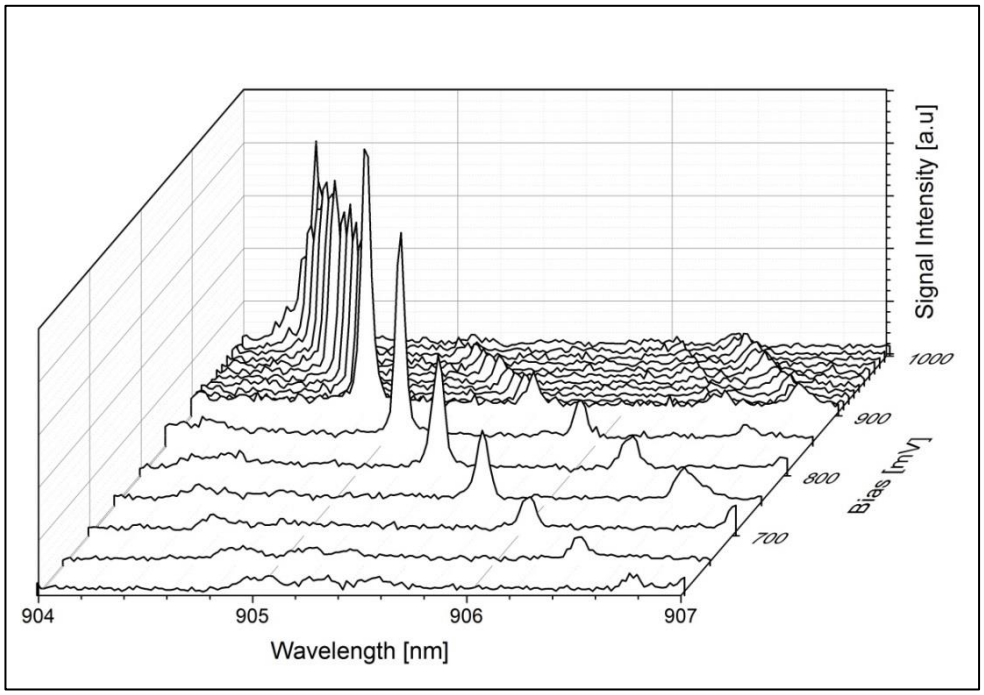

Figure 6-4 – Waterfall plot of observed photoluminescence for a quantum dot embedded in a 170 nm deep by 330 nm wide P-I-N waveguide. Excitation is performed using a HeNe laser focused on the quantum dots location above the waveguide, whilst simultaneously collecting the photoluminescence from an outcoupler.

6.2.4. Spin-initialisation

In addition to the work presented in Chapter 4, where it was demonstrated that the spin of an excitonic state could be preferentially coupled to a propagation direction in the nanobeam waveguide, the reverse of this should also be true. By using resonant excitation, coupled to the waveguide via one of the outcouplers at the end of the waveguide, the excitonic state should see either a left or right handed polarised electric field. The ability to initialise the spin of the exciton state in this way may be of little use for the purpose of resonance fluorescence, however, for devices such as quantum repeaters, it represents a method for ensuring the uni-directional propagation. Work on spin initialisation is currently underway within the LDSD group at Sheffield.

6.3. References

[1] R. J. Coles, “Quantum Optical Circuits using III-V Nanophotonic Structures,” no. April, 2015.

[2] L. Besombes, J. Baumberg, and J. Motohisa, “Coherent Spectroscopy of Optically Gated Charged Single InGaAs Quantum Dots,” *Phys. Rev. Lett.*, vol. 90, no. 25, p. 257402, Jun. 2003.

[3] E. B. Flagg, A. Muller, J. W. Robertson, S. Founta, D. G. Deppe, M. Xiao, W. Ma, G. J. Salamo, and C. K. Shih, “Resonantly driven coherent oscillations in a solid-state quantum emitter,” *Nat. Phys.*, vol. 5, no. 3, pp. 203–207, Jan. 2009.

[4] C. Matthiesen, A. Vamivakas, and M. Atatüre, “Subnatural Linewidth Single Photons from a Quantum Dot,” *Phys. Rev. Lett.*, vol. 108, no. 9, pp. 1–4, Feb. 2012.

[5] A. Dousse, L. Lanco, J. Suffczyński, E. Semenova, A. Miard, A. Lemaître, I. Sagnes, C. Roblin, J. Bloch, and P. Senellart, “Controlled Light-Matter Coupling for a Single Quantum Dot Embedded in a Pillar Microcavity Using Far-Field Optical Lithography,” *Phys. Rev. Lett.*, vol. 101, no. 26, p. 267404, Dec. 2008.

[6] P. Lodahl and S. Mahmoodian, “Interfacing single photons and single quantum dots with photonic nanostructures,” 2013.